

Tahaguas Woldu

Modeling and Simulation of Power System Dynamics for Studying the Impacts of Increasing Wind Power in a Weak Grid System

Tahaguas Woldu: Dynamic model of Wind Power Generation

The issue of environmental concerns and efforts to decrease dependency on fossil fuel are bringing renewable energy resources to the mainstream of electric power generation. Due to the integration of large number of distributed generation systems, more and more conventional generators are eliminated which raises concerns regarding stability and security of supply. In addition, the impact of distributed generation systems, especially wind turbine generators, on dynamic stability is not yet fully understood and needs further investigation. Therefore, the dynamic behavior of wind turbine systems and their impact on system stability are investigated in this thesis work. Moreover, control strategies are proposed to help them not only to remain connected but also to support the system stability during grid fault events.

Modeling and Simulation of Power System Dynamics for Studying the Impacts of Increasing Wind Power in a Weak Grid System

Dissertation

zur Erlangung des akademischen Grades

Doktoringenieur

(Dr.-Ing.)

von **M. Sc. Tahaguas Woldu**

geb. am 03.10.1984 in Rama

genehmigt durch die Fakultät für Elektrotechnik und Informationstechnik
der Otto-von-Guericke-Universität Magdeburg

Gutachter:

Univ.-Prof. Dr.-Ing. habil. Martin Wolter

Univ.-Prof. Dr.-Ing. Fábio Bisogno

Promotionskolloquium am 21. Dezember 2022

Res Electricae Magdeburgenses

Magdeburger Forum zur Elektrotechnik, Jg. 21, Band 94, 2023

<http://www.mafo.ovgu.de/>

IMPRESSUM

Herausgeber:

- Prof. Dr.-Ing. Andreas Lindemann, Lehrstuhl für Leistungselektronik, Institut für Elektrische Energiesysteme
- Prof. Dr.-Ing. habil. Martin Wolter, Lehrstuhl für Elektrische Netze und Erneuerbare Energie, Institut für Elektrische Energiesysteme
- Prof. Dr. rer. nat. Georg Rose, Lehrstuhl für Medizinische Telematik/Medizintechnik, Institut für Medizintechnik
- Prof. Dr.-Ing. Ralf Vick, Lehrstuhl für Elektromagnetische Verträglichkeit, Institut für Medizintechnik

Gründungsherausgeber:

- Prof. Dr. rer. nat. habil. Jürgen Nitsch
- Prof. Dr.-Ing. habil. Zbigniew Antoni Styczynski

alle: Otto-von-Guericke-Universität Magdeburg
Postfach 4120, 39016 Magdeburg

V. i. S. d. P.:

Dr.-Ing. Tahaguas Woldu

Otto-von-Guericke-Universität Magdeburg, Postfach 4120, 39016 Magdeburg

1. Auflage, Magdeburg, Otto-von-Guericke-Universität, 2023

Zugl.: Magdeburg, Univ., Diss., 2023

Auflage: 20

Redaktionsschluss: Februar 2023

ISSN: 1612-2526

ISBN: 978-3-948749-31-6

DOI: 10.24352/UB.OVGU-2023-013

© Copyright 2023 Tahaguas Woldu

Bezug über die Herausgeber

Druck: docupoint GmbH

Otto-von-Guericke-Allee 14, 39179 Barleben

Preface

This Ph.D. thesis is a summarized report during my doctoral studies at the Chair of Electrical Power Networks and Renewable Energy (LENA), Institute of Electric Power Systems (IESY) of the Otto von Guericke University Magdeburg. The financial support during my five-year Ph.D. program has mainly been provided by projects under the LENA chair. Cambridge Industries limited had financially supported me during the first year to settle and pursue my Ph.D. research in Germany. Acknowledgments are given to the aforementioned institute and company.

First and foremost, I would like to express my sincere gratitude to Prof. Dr.-Ing. habil. Martin Wolter who gave me opportunity to supervise my Ph.D. thesis and helped me unconditionally to get to this stage. I am very much pleased to thank Prof. Wolter for his unlimited support and outstanding feedbacks while doing my Ph.D. thesis. It is my great honor to do my Ph.D. research under Prof. Wolter through which I have learned a lot, specifically from his well-organized project management styles and strict requirements on writing scientific contributions.

I am also very grateful to Prof. Wolter for employing and giving me the opportunity to be a part of the TransnetBW GmbH project from 24.06.2019 to 24.02.2021 and UMZUG project starting 01.03.2021. It has been an amazing experience working with my colleagues in the projects, especially with Christian Ziegler and Christian Klabunde, to consolidate my knowledge in the power system area.

My warm regards also extend to Prof. Dr.-Ing. Roberto Leidhold for his support and guiding me to introduce with Prof. Wolter to be my thesis supervisor.

I would also like to thank Prof. Dr. Fábio Bisogno for having interest in my thesis and for being a second examiner.

I am very much obliged to everyone I've collaborated in the LENA chair, especially André Richter, Nicola Könneke, Christian Ziegler and Tamara Schröter for their consistent support related to my research, teaching tasks and helping me in settling down in Magdeburg.

Finally, but the most importantly, I would like to thank to my parents, especially to my beloved wife Rewina and to my children Nathan and Abenezzer for their endless love, solidarity and encouragements.

Magdeburg, 21. 11. 2022
Tahaguas Woldu

Zusammenfassung

Die Sorge um die Umwelt und die Bemühungen, die Abhängigkeit von fossilen Brennstoffen zu verringern, führen dazu, dass erneuerbare Energieressourcen bei der Stromerzeugung in den Vordergrund rücken. Die Windenergie hat in den letzten Jahrzehnten weltweit einen rasanten Ausbau erfahren, was zu Herausforderungen im Systembetrieb in Bezug auf Frequenz- und Spannungsstabilität führt. Die Untersuchung und Bewertung der Auswirkungen großer Windkraftanlagen auf die Dynamik des Stromnetzes ist ein wesentlicher Schritt zur Verbesserung des frequenz- und spannungsstabilen Betriebs. Ziel dieser Arbeit ist es, die Auswirkungen der Windenergie zu untersuchen und Maßnahmen zur Verbesserung des dynamischen Verhaltens von elektrischen Netzen mit verschiedenen Netztopologien vorzuschlagen.

Der doppelt gespeiste Asynchrongenerator (DFIG) ist der am weitesten verbreitete Windturbinentyp, da er mit variabler Windgeschwindigkeit betrieben werden kann, über einen Teillastumrichter verfügt und in der Lage ist, den Generator bei anormalen Bedingungen synchron mit dem Netz zu halten. Daher wird in dieser Arbeit ein detailliertes Modell von DFIG-basierten Windturbinengeneratoren verwendet, um den Einfluss eines steigenden Windenergieanteils in einem großen Netzsystem zu veranschaulichen. Die netzdynamischen Modelle umfassen Synchrongeneratoren, automatische Spannungsregler, Turbinenregelungssysteme, DFIG-basierte Windturbinengeneratoren, verschiedene Steuerelemente, Übertragungssysteme und Transformatoren. Die mathematischen, dynamischen Modelle werden mit Hilfe numerischer Integrationstechniken gelöst. Zu diesem Zweck wird ein Tool zur dynamischen Simulation von Stromsystemen in MATLAB/Simulink entwickelt.

In dieser Arbeit werden vier Testnetze, einschließlich einer Fallstudie für das äthiopische Stromnetz, verwendet, um die dynamischen Reaktionen in verschiedenen Netztopologien zu simulieren. Die verschiedenen Simulationsszenarien und Netztopologien bestätigen, dass eine Erhöhung des Windenergieanteils die transiente Stabilität des Systems verschlechtert. Die Ergebnisse zeigen, dass die Erhöhung des Windkraftanteils zu einer Verringerung der dynamischen Spannungsstabilitätsreserven, einer Erhöhung der Frequenzänderungsrate und einer Verringerung der Wirkleistungsübertragungsfähigkeit führen. Darüber hinaus wird beobachtet, dass sich die DFIGs als Reaktion auf Netzspannungseinbrüche bei schweren Fehlerereignissen selbst vom Netz trennen, um die rotorseitigen Back-to-Back-Umrichter vor Rotorüberströmen zu schützen.

Die dynamischen Auswirkungen von DFIG-basierten Windgeneratoren werden bewertet und es werden Regelungsstrategien vorgeschlagen, die die Windgeneratoren nicht nur unterstützen, am Netz zu bleiben, sondern auch die Systemstabilität bei Netzstörungen zu

verbessern. Es wird eine neue Regelungsstrategie vorgeschlagen, um die Fähigkeit von DFIG-Windgeneratoren zum Niederspannungs-Ride-Through zu verbessern. Die vorgeschlagene Regelungsstrategie umfasst die gemeinsame Anwendung eines STATCOM und einer Rotor-Überdrehzahl-Strategie. Der STATCOM wird hauptsächlich eingesetzt, um den Stator-Spannungseinbruch zu reduzieren und die Rotor-Überdrehzahl-Strategie wird verwendet, um die Rotorüberströme bei Stator-Spannungseinbrüchen zu reduzieren, was zu einer geringeren Ausgangsleistung führt. Die Überdrehzahlregelung wird eingesetzt, um den Wirkleistungssollwert so anzupassen, dass er proportional zum Spannungseinbruch an der Klemme ist. Auf diese Weise wird die Turbine veranlasst, die Rotordrehzahl bis zur maximal zulässigen Grenze zu erhöhen, sodass die Ausgangsleistung so lange reduziert bleibt, bis der Spannungseinbruch am Stator durch den schnell reagierenden STATCOM wieder ausgeglichen wird.

Der zweite Beitrag dieser Doktorarbeit befasst sich mit Lösungen für die Verbesserung der Netzfrequenzstabilität bei höherem Durchdringungsgrad von Windenergie. Es wird ein neuer Ansatz vorgestellt, mit dem die Betreiber von Windkraftanlagen ihre Windenergieerzeugung so planen können, dass sie den Prozess der Wiederherstellung der Netzfrequenz unterstützen. Das vorgeschlagene Frequenzregelungsmodul auf Anlagenebene überwacht den Beitrag der verschiedenen Betriebseinheiten in einem großen Windpark auf der Grundlage ihrer jeweiligen Windgeschwindigkeit und der Netzfrequenzabweichung.

Die dynamischen Simulationsergebnisse zeigen, dass die vorgeschlagenen Spannungs- und Frequenzregelungsstrategien effizient sind, um den Spannungsabfall in Echtzeit zu regulieren und die Steuerbarkeit von Spannung und Frequenz bei einem höheren Durchdringungsgrad der Windenergie zu verbessern.

Abstract

The issue of environmental concerns and efforts to decrease dependency on fossil fuel are bringing renewable energy resources to the mainstream of electric power generation. Wind energy has undergone fast expansions worldwide in recent decades, but it also results in challenges in system operation related to frequency and voltage stabilities. Investigating and evaluating the impact of large-scale wind power on power system dynamics is an essential step to enhance the stable operation of frequency and voltage. This thesis work is intended to investigate the impacts of wind power and propose mitigation measures to enhance the dynamic behaviors of power systems with various network topologies.

Doubly-fed induction generator (DFIG) is the most common wind turbine type due to its ability to operate at variable wind speed, partial-load converter and its capability to sustain the generator in synchronism with the system during abnormal conditions. Therefore, in this thesis work, a detailed model of DFIG-based wind turbine generators is employed to illustrate the influence of increasing wind power share in a large network system. The network dynamic models include synchronous generators, automatic voltage regulators, turbine-governor systems, DFIG-based wind turbine generators, various control elements, transmission systems and transformers. The mathematical dynamic models are solved using numerical integration techniques. For this purpose, a power system dynamic simulation tool is developed in the MATLAB/Simulink environment.

In this thesis work, four test networks, including a case study for the Ethiopian power system, are employed to simulate the dynamic responses in different network topologies. The various simulation scenarios and network topologies confirm that an increase in wind power share deteriorates the transient stability of a system. The results effectively show that the increase in wind power penetration level has contributed to reducing the dynamic voltage stability margins, increasing the rate of change of frequency and reducing active power transfer capability. Moreover, the DFIGs are observed to disconnect themselves from the grid in response to grid voltage dips under severe fault events so as to protect the back-to-back rotor-side converters from rotor over-currents.

The dynamic impacts of DFIG-based wind generators are assessed and control strategies are proposed to help them not only to remain connected but also to support the system stability during grid fault events. A new control strategy is contributed to enhance the low voltage ride-through capability of DFIG-based wind generators. The proposed control strategy comprises a joint application of a STATCOM and rotor over-speeding schemes. The STATCOM is mainly employed to improve the stator voltage dip and the rotor over-speeding strategy is employed to reduce the rotor over-currents during stator voltage dips

that results in reduced output power. The over-speeding scheme is initiated to adjust the active power reference to be proportional to the voltage dip at the terminal. Thus, the turbine is made to increase the rotor speed till the maximum allowable limit so that the output power remains reduced until the stator voltage dip is recovered by the fast-acting STATCOM.

The second contribution is related to solutions to the grid frequency challenges with higher penetration level of wind power. A new approach is introduced by which wind power plant operators can schedule their wind power generations so as to give support in the frequency restoration process. The proposed frequency control module at plant level monitors the contribution of various operating units in a large wind farm, based on their respective wind speed and the grid frequency deviation.

The time-domain simulation results indicate that the proposed voltage and frequency control strategies are efficient to regulate the real-time voltage dip and enhance the voltage and frequency controllability with higher penetration level of wind power.

Table of Contents

Zusammenfassung	I
Abstract	III
Table of Contents.....	V
List of Figures	VIII
List of Tables.....	XI
List of Symbols.....	XII
List of Abbreviations.....	XV
1 Introduction	1
1.1 Background and motivation	1
1.1.1 Objective of the research	6
1.2 Approach and structure of the work	7
2 State of the Art of Electric Power Systems	8
2.1 Current status and recent trends	8
2.2 Conventional power generation.....	9
2.3 Wind power generation	9
2.3.1 Aerodynamic power regulation	12
2.3.2 Wind generator integration concepts.....	13
2.4 Challenges of wind power generation	15
2.4.1 Wind generator voltage control strategies.....	17
2.4.2 System balancing with wind power.....	18
2.5 Wind turbine and control structure.....	18
3 Mathematical Modeling of Power Systems	21
3.1 General	21
3.2 Modelling of transformers, transmission lines and loads.....	23
3.2.1 Transmission line	23
3.2.2 Transformer	24
3.2.3 Loads	25
3.2.4 Protection system	26
3.3 Modelling of the conventional generation stations	26
3.3.1 Synchronous generator model	26
3.3.1.1 Rotor voltage equations.....	28
3.3.1.2 Stator voltage equations	28
3.3.1.3 Transient saliency.....	29
3.3.1.4 The swing equations	31
3.3.2 Excitation system	33

3.3.2.1	Simplified model of static ST1A exciter	33
3.3.2.2	IEEE-type DC1A.....	34
3.3.3	Speed-governor and turbine systems.....	35
3.4	Grid interfacing	36
4	DFIG-based Wind Turbine Dynamic Model	40
4.1	Generic dynamic wind turbine models.....	40
4.2	Wind speed model	42
4.3	Wind turbine model.....	42
4.4	Drive-train model	44
4.5	Induction generator model.....	46
4.5.1	Steady-state operation	47
4.5.2	Dynamic model of DFIG.....	49
4.5.2.1	Stator and rotor equations.....	50
4.5.2.2	dq-axes model.....	52
4.5.2.3	The per unit system model	53
4.6	Current-controlled converter voltage sources	56
4.6.1	Rotor-side converter voltage source.....	57
4.6.2	Grid-side converter voltage source.....	62
4.6.3	DC-link converter model.....	64
4.6.4	Pitch control system	65
4.7	STATCOM for reactive power compensation	65
4.8	Wind turbine aggregation.....	66
4.9	Grid interfacing	68
5	Multi-machine Power System Representation for Transient Stability Studies.....	70
5.1	General	70
5.2	Power flow Analysis	71
5.3	Transient stability analyses	78
5.4	Prediction methods for dynamic voltage stability margins.....	80
5.5	Calculation of initial conditions	82
5.5.1	Initialization of the dynamic models of synchronous generators.....	83
5.5.2	Initialize the dynamic models of wind generators.....	84
5.6	Numerical solutions of power network dynamic models.....	88
6	Case Studies	93
6.1	Impacts of wind generators on transient responses	93
6.1.1	Analyses of the dynamic characteristics of a wind power plant connected to a voltage source.....	93

6.1.2	Transient response analyses of the New England test system.....	100
6.2	Voltage dip enhancement using STATCOM	107
6.2.1	Fault ride-through capability enhancement using the rotor over-speeding control strategy	110
6.3	Transient responses for the case of the Ethiopian power system	113
7	Control Strategy to Regulate Grid Frequency with Higher Wind Power Share	116
7.1	Introduction	116
7.2	De-loading operations of DFIG-based wind power plants.....	116
7.3	Proposed wind power plant frequency control module.....	117
7.4	Test system simulation for frequency enhancement	122
8	Conclusions and Future Work	126
9	References	128
	Appendices	134
A	DFIG-based wind turbine input data	134
B	4-Bus test network data	135
C	New England test network data	136
D	The Ethiopian power network data	139
E	Microgrid test network data.....	142

List of Figures

Figure 1.1	Impacts of inverter-based generation in power systems [3]	2
Figure 1.2	Installed capacity of energy sources in the Ethiopian Electric Power [9]	4
Figure 1.3	Monthly average hydro flow rate in Ethiopia [9]	4
Figure 1.4	Monthly average wind speed of wind farms in Ethiopia [9]	5
Figure 1.5	Monthly peak load as percent of the annual peak in the Ethiopian power system [9]	5
Figure 2.1	Traditional electric power system structures [10]	8
Figure 2.2	Historic development of total installations of wind power in the world [15] 10	
Figure 2.3	Historic development of Germany's grid-connected wind power installations [16]	11
Figure 2.4	Historic development of Ethiopia's grid-connected wind power installations [8]	11
Figure 2.5	Evolution of wind turbine dimensions [5]	12
Figure 2.6	Constant speed wind turbines (Type 1 and Type 2) [17]	13
Figure 2.7	Variable speed wind turbines (Type 3 and Type 4) [18]	14
Figure 2.8	General architecture of DFIG-based variable speed wind turbine control strategies	20
Figure 3.1	Equivalent circuit diagram of a line [45]	24
Figure 3.2	T-Model transformer equivalent [45]	25
Figure 3.3	Model of synchronous generator - 4th order [41]	27
Figure 3.4	Dynamic equivalent circuit of synchronous generator with transient saliency [41]	31
Figure 3.5	Schematic diagram to illustrate the interaction of rotor dynamics [43]	31
Figure 3.6	Single-time constant IEEE-type ST1A excitation system [36], [41]	33
Figure 3.7	IEEE-type DC1A excitation system model [13] [36]	34
Figure 3.8	Simplified model for speed-governor and hydro-turbine system [36], [41].	35
Figure 3.9	Phase diagram of generator dq-frame and synchronous axis $\alpha\beta$ -frame [41], [48]	37
Figure 3.10	Synchronous generator as source-current in the dq-frame [41]	37
Figure 3.11	Synchronous generator grid integration layout for time simulation [36]	39
Figure 4.1	Schematic diagram of a typical WTG [49]	41
Figure 4.2	Wind turbine control strategy based on four speed control regions [52]	43
Figure 4.3	Two-mass wind turbine shaft system [53]	45
Figure 4.4	Schematic diagram of doubly-fed induction generator and converter	46
Figure 4.5	Equivalent circuit of DFIG with rotor parameters referred to the stator [25]	48
Figure 4.6	DFIG reference frame to represent in space vectors [25]	50
Figure 4.7	RMS equivalent dynamic circuit of the DFIG in network reference frames [52]	51

Figure 4.8	Schematic diagram of DFIG-based wind turbine control strategy [25]	57
Figure 4.9	Synchronous rotating dq-frame aligned with the stator flux space vector [52]	58
Figure 4.10	Block diagram of DFIG rotor-side converter control strategies [54]	60
Figure 4.11	Block diagram of DFIG grid-side converter control strategies [54].....	62
Figure 4.12	Equivalent circuit of DFIG back-to-back converter model [54]	64
Figure 4.13	DFIG-based wind turbine pitch control system [35].....	65
Figure 4.14	Block diagram of simplified STATCOM for RMS model [12]	66
Figure 4.15	Wind power plant aggregation model	68
Figure 4.16	Complete DFIG model layout with interfacing to the grid system [52].....	68
Figure 4.17	Axis transformation between dq-frame and $\alpha\beta$ -frame [12].....	69
Figure 5.1	Structure for power network stability studies [37]	78
Figure 5.2	A load connected to infinite bus	81
Figure 5.3	Typical P-U curve of a load connected to infinite bus [58].....	81
Figure 5.4	P-U curves of three voltage source cases (a) and three cases of load PF (b)	82
Figure 5.5	The steady-state generated power P_g , stator power P_s and rotor power P_r (in a) rotor power and rotor slip characteristics (in b) for varying rotor speed.....	87
Figure 5.6	DFIG steady-state outputs (a) stator and rotor voltages (b) stator and rotor currents for varying rotor speed	88
Figure 5.7	Dynamic power system simulation flow chart	91
Figure 5.8	Complete schematic diagram for the multi-machine power system modeling and grid integration	92
Figure 6.1	Aggregated DFIG-based wind power plant in a 4-bus test grid.....	94
Figure 6.2	Aggregated wind power plant simulation results for varying input wind speed	95
Figure 6.3	Three-phase fault transient responses of the 4-bus test grid with SG at bus 4 and AWPP at bus 1.....	96
Figure 6.4	Three-phase fault transient responses of the 4-bus test grid with both AWPPs at bus 1 and bus 4	98
Figure 6.5	Test grid simulation in response to large load change at bus 4 and varying input wind speeds from 12 m/s to 18 m/s.....	99
Figure 6.6	New England IEEE 39-bus system with three synchronous generators replaced by wind generators and three-phase fault at bus 12 [66]	101
Figure 6.7	Impacts of wind power increase on frequency and voltage responses to three- phase fault at critical bus	103
Figure 6.8	P-U curves and corresponding stability indices at the critical bus for the three scenarios	104
Figure 6.9	Stable transient responses of three-phase fault with hydro-generators	105
Figure 6.10	Stable transient responses of load change at bus 20 with hydro-generators	106
Figure 6.11	Stable voltage responses with and without STATCOM during fault event at bus 20	108

Figure 6.12	Transient responses to a three-phase fault at bus 20 with fault clearing time of 120 ms without STATCOM.....	109
Figure 6.13	Transient responses to a three-phase fault at bus 20 with fault clearing time of 120 ms with STATCOM.....	109
Figure 6.14	Rotor-side converter active and reactive power control with rotor over-speeding strategy in response to voltage dips.....	111
Figure 6.15	Improved LVRT capability of DFIG transient responses to symmetrical fault at bus 20.....	112
Figure 6.16	Ethiopian grid system's stable response to 100 % load change at bus 158 with wind power penetration level of 14 %.....	114
Figure 6.17	Ethiopian grid system's unstable response to 100 % load change at bus 158 with wind power penetration level of 28 %.....	115
Figure 7.1	De-loading operation of wind turbines (a) through rotor over-speeding and pitch angle regulation techniques (b).....	117
Figure 7.2	DFIG-based wind turbine types and corresponding reserve of de-loading operation.....	118
Figure 7.3	Algorithm in the WPP Control Module to dispatch the wind generators...	120
Figure 7.4	Speed droop values based on the generation margin.....	121
Figure 7.5	Microgrid with frequency control capability of WPP.....	123
Figure 7.6	Frequency response of the aggregated wind generators for a load change of 50 MW with penetration level of wind power of 75 %.....	124
Figure 7.7	Virtual inertia and primary frequency responses of wind generators for consecutive load changes and penetration level of wind power of 100 % .	125
Figure 7.8	Unstable frequency response for a load change above the pre-defined power constraint.....	125

List of Tables

Table 5.1	Parameters of 2 MW DFIG [26].....	87
Table 5.2	Parameters of 1.5 MW DFIG [48].....	87
Table 7.1	The results of de-loading rate and droop settings with ΔPL of 50 MW.....	123
Table A.1	Generator and turbine parameters of 2 MW DFIG [26].....	134
Table A.2	Converter and pitch control parameters of 2 MW DFIG [26].....	134
Table A.3	Generator and turbine parameters of 1.5 MW DFIG [48].....	134
Table A.4	Converter and pitch control parameters of 1.5 MW DFIG [48].....	135
Table A.5	Bus data for 4-bus test system.....	135
Table A.6	Synchronous machine data for 4-bus test system.....	135
Table A.7	Transmission line data for 4-bus test system.....	135
Table A.8	Two winding transformer data for 4-bus test system	135
Table A.9	Bus data for New England test network (39-bus system)	136
Table A.10	Synchronous machine data for IEEE 39-bus system bus	137
Table A.11	Transmission line data for New England test network (39-bus system)	138
Table A.12	Two-winding transformer data for New England test network (39-bus system)	139
Table A.13	Base load data of the existing conventional generators for the stable case	140
Table A.14	Base load data of the existing aggregated wind power generators for the stable case.....	141
Table A.15	Base load data for the microgrid system	142
Table A.16	Synchronous generator parameters of the thermal power plant in the microgrid	142

List of Symbols

List of symbols in the document refer to Greek letters and nomenclatures of variables and their indices.

Greek symbols

Symbol	Description	Unit
ρ	Density	kg/m ³
τ	Transformer voltage ratio	-
δ	Voltage angle	deg.
β	Pitch angle	deg.
θ	Rotor angle	deg.
α	Admittance angle	deg.
γ	Load impedance angle	deg.
v	Wind speed	m/s
ω	Generator rotor speed	elec. rad/s
Ω	Mechanical rotor speed	mech. rad/s
λ	Rotor tip-speed-ratio	-
ϖ	Gust wind speed	m/s
ψ	Flux	Volt/s
Δ	Change of variable	Varying
s	Rotor slip	-
σ	Leakage reactance	-

Nomenclatures

Running indices

Symbol	Description
k	Network node number
w	Aggregated wind generators
i	Varying index of network nodes
n	Varying indices of an array vector
m	Varying indices of an array vector
v	Time step counter
μ	Iteration number counter

Descriptive indices**Superscript Indices**

Symbol	Description
T	Transposed
*	Complex conjugated
<i>np</i>	Active power voltage dependency
<i>nq</i>	Reactive power voltage dependency
s	Referred to stator reference frame
r	Referred to rotor reference frame

Subscript Indices

b	Base value	K	Network buses
c	Converter	lr	Rotor leakage reactance
CI	Cut-in wind speed	ls	Stator leakage reactance
CO	Cut-out wind speed	max	Maximum value
conv	Converter	min	Minimum value
crt	Critical	opt	Optimal
ctrl	Control	r	Rotor
dc	Direct current	rc	Rotor-side converter
del	De-loading	ref	Reference
Fe	Iron losses	s	Stator
g	Generator	Thev	Thevenin equivalent
gc	Grid side converter	W	Wind generator buses
h	Magnetizing losses	α, β	System indexes in $\alpha, \beta, 0$ coordinates
L	Load	d, q	System indexes in d, q, 0 coordinates

Variables

Nomenclatures in this document are interpreted as follows. Variables printed in italic represent instantaneous values (time-variant) and variables with underline depict complex values. Variables which are printed in bold, italic and upper case depict matrices while variables written in bold, italic and lower case represent vectors.

Symbol	Description	Unit
<i>A</i>	Rotor swept area	m ²
<i>D</i>	Diameter	m
<i>C_p</i>	Power conversion coefficient	-
<i>R</i>	Resistance	Ohm
<i>X</i>	Reactance	Ohm
<i>L</i>	Inductance	Henry
<i>C</i>	Capacitance	Farad
<i>Z</i>	Impedance	Ohm
<i>G</i>	Conductance	Siemens
<i>Y</i>	Admittance	Siemens
<i>B</i>	Susceptance	Siemens
<i>U</i>	Voltage	Volt
<i>I</i>	Current	Ampere
<i>P</i>	Active power	MW
<i>Q</i>	Reactive power	Mvar
<i>S</i>	Apparent power	MVA
<i>T</i>	Torque	Nm
<i>x</i>	State variable	-
<i>u</i>	Input variables	-
<i>K</i>	PID gain constant	-
<i>G</i>	Gate valve position	Pu
<i>H</i>	Inertia constant	Seconds
<i>F</i>	Frequency	Hertz
ΔP	Change of power	MW
<i>M</i>	Nodes with wind power generation	Number
<i>T</i>	Decay time constant	Seconds

List of Abbreviations

AEs	Algebraic equations
AVR	Automatic voltage regulators
AWPP	Aggregated wind power plant
BTB	Back-to-back
DAEs	Differential algebraic equations
DEs	Differential equations
DFIG	Doubly-fed induction generator
DVSM	Dynamic voltage stability margin
EEP	Ethiopian Electric Power
EHV	Extra high voltage
emf	Electromagnetic
EMT	Electromagnetic Transient
ESIG	Energy system international group
FACTS	Flexible alternating current transmission systems
FLC	Full-load converter
GB	Gearbox
GSC	Grid-side converter
HV	High voltage
IBG	Inverter-based generation
IG	Induction generators
LV	Low voltage
LVRT	Low voltage ride-through
MPP	Maximum power point
MPPT	Maximum power point tracking
MV	Medium voltage
NNVSI	New node voltage stability index
PF	Power factor
PFR	Primary frequency response
PLC	Partial-load converters
PMSG	Permanent magnet synchronous generators
POC	Point of connection
PSDST	Power system dynamic simulation tool
PTSI	Power transfer stability index
P-U	Power versus voltage curve
Pu	Per unit
PWM	Pulse width-modulated

RES	Renewable energy sources
RMS	Root Mean Square
ROCOF	Rate-of-change-of-frequency
RSC	Rotor-side converter
SCIG	Squirrel cage induction generators
SG	Synchronous generator
SMIB	Single machine infinite bus
SSSC	Static synchronous series compensator
STATCOM	Static synchronous compensator
SVC	Static VAR compensator
TCSC	Thyristor-controlled series capacitor
VIR	Virtual inertia response
VSWT	Variable rotor speed wind turbine
WECC	Western Electric Coordinating Council
WPP	Wind power plant
WRIG	Wound rotor induction generator
WRSG	Wound rotor synchronous generators
WTG	Wind turbine generator

1 Introduction

Electrical power systems are the backbone of modern society and their stable and reliable operation has top priority. The existing networks are under continuous modification process for being robust, intelligent, optimized and self-sufficient to take decisions with pre-defined conditions so that reliable system is sustained. The growing environmental concerns and efforts to reduce reliance on fossil fuel resources are bringing renewable energy resources (RES) to the mainstream of energy sector. RES such as solar and wind are contributing significant share of electrical power supply in the present era. Wind energy has also an essential role to play in the global energy supply over the coming decades [1].

Among the various RES, wind power is assumed to have the most promising technical and economic prospects [1]. Although, wind turbines have scenery visual impacts and emit some noise, such consequences are minor and the ecosystems seem hardly to be permanently affected. Wind is among the renewable and unlimited primary energy sources. Moreover, wind turbines are installed and generate power within few months and operate with wind as fuel which indicates that the levelized energy cost over the life cycle is definitely positive [2].

1.1 Background and motivation

The increasing growth of price in fossil fuel products together with environmental concerns have caused an increase in the share of RES. Inverter-based generations (IBG) like wind energy and other renewable energy sources are gradually dominating the electricity power generation [3]. Due to the engagement of power electronic converters, variable wind turbine generators are partially or fully electrically decoupled from the grid systems which reduce the overall system inertia as in Figure 1.1. This can potentially affect the inertial response of the network dynamics. The impact of a wind turbine generator (WTG) on power system dynamics is becoming increasingly important as power capacity from wind is growing [2]. The dynamic behavior of a power network is by far delimited by the interaction of generators. Synchronous generators are controllable generators that regulate their output power and voltage depending on the grid feedbacks.

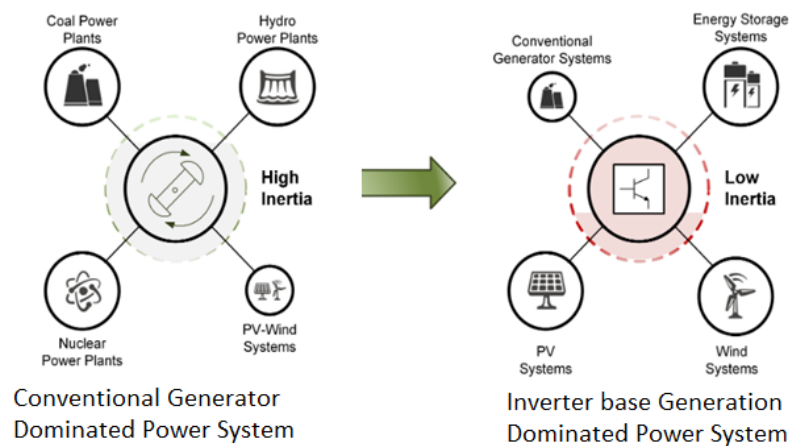


Figure 1.1 Impacts of inverter-based generation in power systems [3]

Power systems with large share of inverter-based generation are observed to behave differently and to challenge various system stability aspects [2], [3]. Such stability problems are related to

- limited reactive power generation to support dynamic voltage stability;
- power system's inertial response decreased which leads to an increased rate-of-change-of-frequency (ROCOF) and
- lack of generation dispatch capability due to the stochastic nature of sources such as in wind power stations

Renewable energy resources are generally characterized by a higher degree of source variability and intermittency for which their availability cannot be predicted with certainty. Such situations increase the complexity of generation dispatching and difficulty of operation planning of power systems with higher share of renewable sources [2]. The growing share of intermittent supply of electricity needs stronger networks with better energy system management of the network assets [2]. The major power system operation challenges with high level of RES include the issues of supply uncertainty, supply and demand balancing, network stability, reliability and others [4]. As in [2], a resilient power system can be defined as one that can respond reliably and quickly to sudden changes and fluctuations in the network supply and demand, due to anticipated or unforeseen variations. Modern power systems are demanding to be more flexible particularly when integrating high penetration level of RES. Power system operators are observed to use several ways to improve their system flexibility [2], [3], [5].

- Increasing flexible and fast spinning reserve capacity
- Diversification of energy mix that can complement each other
- Energy storage to stabilize system fluctuations

- Congestion management which promotes and provides better access to flexible generation sources
- Market integration by developing cross-border power transmission systems

The major problems in modern power systems are still related to frequency deviations and voltage collapses which are an indicator of limited stability margins in the steady-state case. The steady-state frequency variability is associated with angle instability and slow loss of synchronism among generators. The other problem related with slow voltage collapse at load buses under higher loading conditions, while limited reactive power, is among the recent phenomena [4]. RES, particularly wind and solar energy sources have significant impact on reactive power demand and flow over the network. As long as the power share of RES is limited, the behavior of power system dynamics is generally governed by conventional generators [2]. The penetration levels up to which generators with uncontrolled output can safely be integrated to a power system without additional measures depends on [2]:

- Network topology and operation standards
- Spinning reserve and network coupling
- Characteristics of the uncontrolled energy sources
- Load curve and their interaction with the primary energy sources
- The control mechanisms in the primary energy sources

It is difficult to make general statements with respect to the amount of wind generation that can be integrated into a power grid. Thus, the study of how much integrated wind power affects power system operation becomes quite important for power system operators. Some researchers have worked on the subject to realize the dynamic characteristics of wind generators with high wind power penetration levels [6], [7]. Most of these researches investigate the impacts of a single wind turbine or an aggregated wind park connected to a network represented by a constant voltage source. The current researches are limited to demonstrate the impacts when the wind power share in the whole system is increased in various network topologies. The motive of this research work is to get insight into the impacts of large-scale wind power with various network topologies (weak and de-regulated system) and propose strategic solutions.

The research motivation is originally initiated from the challenges related to the increasing wind power in the Ethiopian power sector. Ethiopia's total installed generation capacity is about 4.5 GW in 2022 [8]. The Ethiopian power system is a hydro-dominated system and has been severely affected by drought for which the government of Ethiopia has put forward a strategic plan to diversify the energy mix with other sources such as solar, wind, and geothermal that results in a more climate-resilient power system [9]. Figure 1.2 shows the hydro-dominated energy mix of the Ethiopian grid with current and

projected installed capacity of power plants till the year 2030 [9]. Several large hydro and wind power plants are currently under development, such as the 5.15 GW grand Ethiopian renaissance dam, the 120 MW Aysha wind power project and 100 MW Asela wind power project. Despite the incredible efforts towards generating electricity from hydropower, there is a huge gap in diversifying the energy mix. As per the Ethiopian Electric Power (EEP) planning forecasts, the projected total installed capacity will be 10,358 MW by 2025. Ethiopia currently exports electricity to Djibouti and Sudan up to 100 MW to each country. Ethiopia is also negotiating power purchase agreement with Kenya to begin exporting up to 400 MW [8]. This all indicates that the grid system is growing very fast and it needs technical strategies to enhance the system operation with high share of RES.

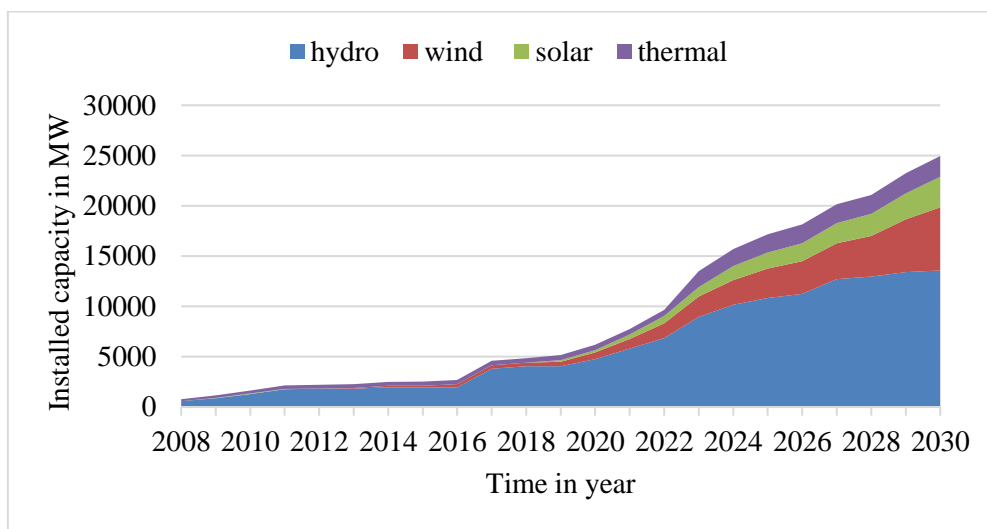


Figure 1.2 Installed capacity of energy sources in the Ethiopian Electric Power [9]

According to [9], the monthly average water flow rate of hydropower plants is presented in Figure 1.3.

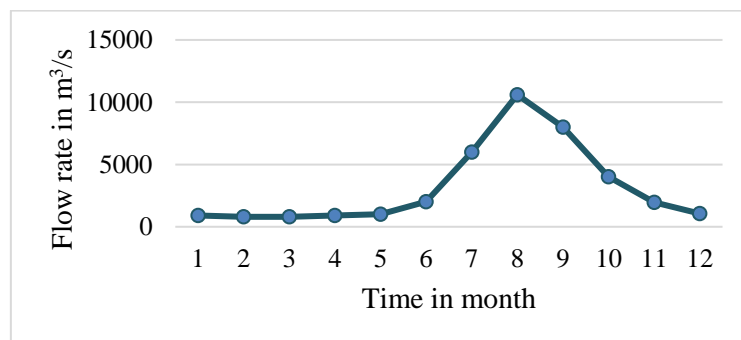


Figure 1.3 Monthly average hydro flow rate in Ethiopia [9]

The monthly average values, in Figure 1.3, show that there is high flow rate in the summer season (June, July and August) and comparatively low in the other seasons. Similarly, the average monthly wind speed of the operational wind power plants (Adama-I, Adama-II, Ashegoda and Aysha wind farms) is shown in Figure 1.4 [9].

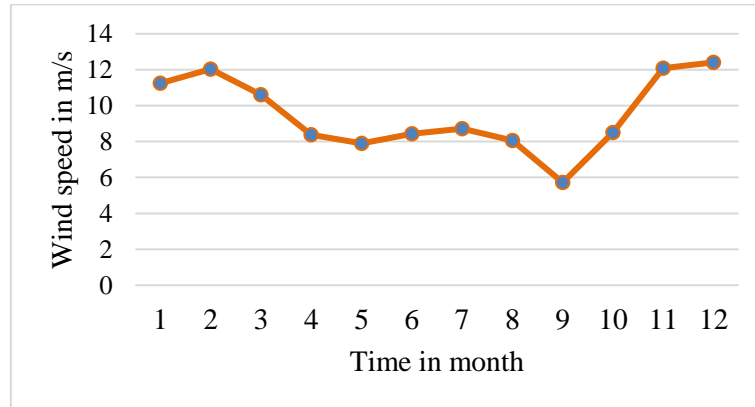


Figure 1.4 Monthly average wind speed of wind farms in Ethiopia [9]

The load characteristics of the Ethiopian power system is also another important issue that contributes to the increase in wind power share. The Ethiopian power system has mainly domestic and industrial load types where the domestic has significant impact on the supply-demand balance of the grid. The monthly peak load as of the annual peak is calculated in [9] and presented in Figure 1.5.

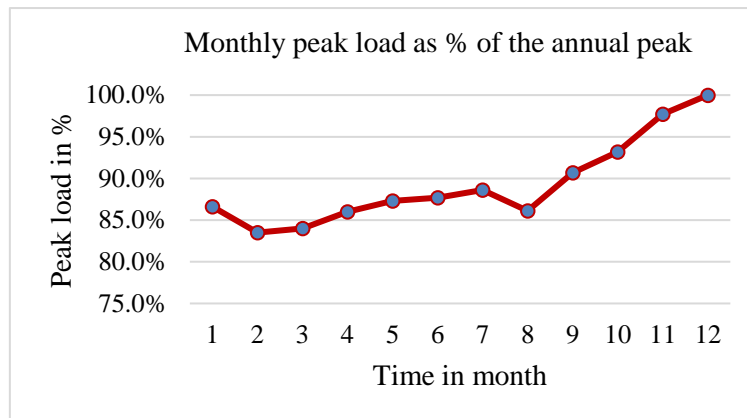


Figure 1.5 Monthly peak load as percent of the annual peak in the Ethiopian power system [9]

Figure 1.5 shows that the autumn season has relatively high electricity demand because this season is the coldest season in Ethiopia. The annual peak demand is registered on the month of December, which could be the Christmas holiday as most of the loads are domestic type. While the peak demand in the month of January drops to 86.6 % of the peak in December. Moreover, the source data shows that the months of February and March

have low monthly peak demands. However, the average wind speeds of the operating wind power plants are high, above 10 m/s, in the months of February and March as in Figure 1.4.

Based on the above average monthly water flows, wind speeds and load rates, there is peak wind power generation during winter time and light load periods where the hydro flow is reduced. Such nature of energy sources and load characteristics contribute to a relatively large share of wind power in the grid system which results in system stability problems to operate specifically for a weak power system.

As the Ethiopian power system is being transformed from a hydro-dominated system to a substantial share of wind power, it is critical to investigate the impact and put forward solutions for reliable operation. Wind power capacity in Ethiopia is expected to ramp up in the near future with several large-scale wind projects in the pipeline. Despite the abundant wind resources in the country, the existing power grid is weak and hydropower dominated system which is currently even challenging the operators during droughts and light load operation. Indeed, the wind sources are high during the winter and spring seasons while there is shortage of water in the hydropower reservoirs. Moreover, the daily wind distributions show most of the operating wind farms have high wind during night when the national load goes down. Such specific wind regime characteristics increase the share of power from wind in the network and this makes the operation of grid-connected wind power plants to be more challenging. Currently, wind power generation is restricted during light load durations to decrease the relative wind capacity share in the grid. In this regard, though the wind speeds are high, multiple wind turbines are deliberately turned off due to the system stability issues of the grid system.

1.1.1 Objective of the research

The main aim of the research work is to investigate the interaction of integration of wind power generators into weak grids and propose mitigation measures to overcome their dynamic impacts. The thesis is intended to get its objective through the following specific research tasks:

- Quantification of the impact of wind generation in power systems
- Development of control strategies to mitigate negative effects of wind energy
- Development of a strategy to maximize the extent of wind energy in weak grids with a special focus on the Ethiopian power system

The impacts of integrating wind power aspects are studied using diverse network topologies under various scenarios. The thesis research proposes control strategies to enhance the flexibility and reliability of power system operations under higher penetration levels of wind capacity.

1.2 Approach and structure of the work

As part of the introduction, the general overviews of the existing conventional power plant behaviors and the state of the art for current wind turbine technologies and their grid integration techniques are reviewed and presented in chapter 2. Also, previous literature assessments on the challenges of wind power are reviewed and documented to use as an input in the preceding sections.

The second part of the thesis, chapter 3 and chapter 4, presents the mathematical models and derivations of the power system dynamics. The dynamic models for power network components including the conventional generators are presented in chapter 3 and in chapter 4, the dynamic models of DFIG-based wind turbines including their control strategies and grid-integration are presented.

The third part, chapter 5 and chapter 6, presents the detailed multi-machine transient stability analyses. Chapter 5 focuses on representing the multi-machine power system dynamics for transient stability studies and validating the generic model for DFIG-based wind turbine generator in contrast to power-curves from manufacturers' data sheets. In chapter 6, the time-domain simulations of the network dynamic are numerically solved and discussed with regard to the negative impacts of wind power by employing various network topologies and scenarios.

Chapter 7 discusses specifically on the proposed control strategies to enhance the employment of higher wind power integration with regard to frequency control issues. Finally, the thesis work concludes by summarizing the research findings and briefing the outlook tasks.

2 State of the Art of Electric Power Systems

2.1 Current status and recent trends

The traditional electric network consists of three major elements: the generation station, power transmission system, and distribution system as depicted in Figure 2.1 [10]. The transmission systems, usually with extra high voltage (EHV) and ultra-high voltage (UHV), link the generation stations to load centers or substations, which supply power to the end user through the distribution system [11]. The generators convert the input mechanical power into electrical power. In the majority of cases, the mechanical power is derived by primary energy sources either from thermal energy or flowing fluid. In most conventional power plants, the conversion of mechanical energy to electrical energy is realized by means of synchronous generators. Whereas, in wind generation systems, both synchronous and asynchronous generators are used. The electric power is usually generated at medium voltage (MV) levels and then fed into the power transmission system via step-up transformers [11].

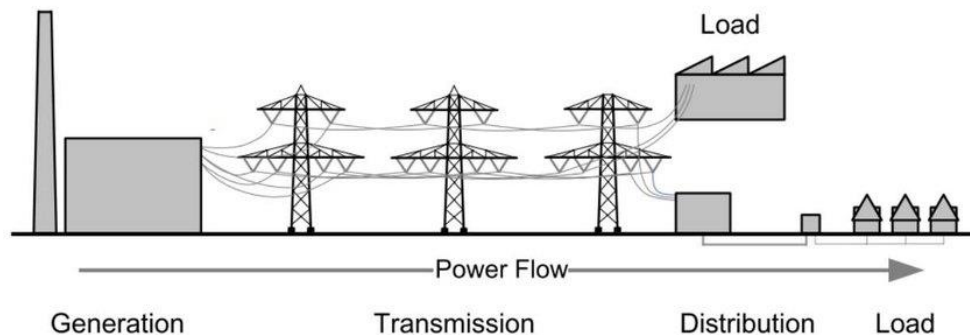


Figure 2.1 Traditional electric power system structures [10]

Power transmission systems connect generating stations to major load centers or substations that distribute power to end users. Transmission systems are named as the back bone of a power system which operate generally at the highest voltage levels in the grid. Transmission lines operate at various voltage levels in different countries. For instance, in Germany, the transmission networks are at voltage levels of 220 kV and 380 kV while for the Ethiopian power system the transmission system includes voltage levels at 132 kV, 230 kV, 400 kV and 500 kV [9]. Similarly, the distribution system represents the last stage of power transfer to the consumers. The primary distribution system operates at medium voltage levels, typically for the Germany network, this ranges between 6 kV and 60 kV. While in the Ethiopian power system, the primary distribution system includes

voltage levels at 15 kV, 33 kV, 45 kV and 66 kV [9]. The secondary distribution feeders are constructed to supply power into residential and commercial customers at 400 V for the 50 Hz grid [11].

2.2 Conventional power generation

Conventional power generation is a general term applied to the energy conversion process of electrical energy from primary energy sources such as oil, coal, or natural gas or flowing fluid [11], [12]. The generator is usually a synchronous machine having various numbers of poles depending on the running rated speed of the generator rotor and grid frequency. The synchronous generators are usually connected directly to a grid via the stator windings. For this reason, the frequency and phase of the electrical quantities at the stator are synchronized with the grid system, i.e., the frequency and phase of the voltages at the connection point are the same.

The conventional generating stations are usually constructed from classical, wound-field, cylindrical rotor, or salient-pole synchronous generators (SGs), which are excited by relatively complex feedback control system, whose primary purpose is to maintain the generators' terminal voltages constant [13]. The generator voltage regulation is automatically accomplished by the excitation system employed with the synchronous generator. Conventional power plants are also employed with frequency control modules named as governor-turbine system to regulate the frequency and rotor angle [11] - [13].

2.3 Wind power generation

Similar to conventional generators, wind generators convert rotational energy, provided by wind turbines, into electrical energy using the application of electromagnetic fields. Unlike most conventional power plants, the primary energy source is uncontrolled and intermittent in nature which leads to difficulties in regulating the output power. Wind turbines extract kinetic energy from the swept area of the blades. The wind passes through the blades (swept rotor area) by generating lift and exerting a turning force. The rotating blades turn the low-speed shaft inside the nacelle, which connects it into a gearbox. The gearbox helps to increase the rotational speed and transfer the mechanical torque via bearings into an appropriate high-speed rotor shaft connected to the generator. The power in the airflow, P_{wind} is given by [14].

$$P_{\text{wind}} = \frac{1}{2} \rho A v^3 \quad (2.1)$$

Where, ρ is the air density (approximately 1.225 kg m^{-3} at sea level); A is the swept area of the rotor in m^2 and v is the undisturbed wind speed in m/s

Energy extraction from free-flowing fluid streams imply decreasing the fluid velocity which cannot fall down to zero. Hence, equation (2.1) expresses the available potential power in the wind while the actual power that can be transferred to the turbine rotor blades, P_{turbine} is limited by the power coefficient C_p .

$$C_p = \frac{P_{\text{turbine}}}{P_{\text{wind}}} \quad (2.2)$$

$$P_{\text{turbine}} = C_p P_{\text{wind}} = \frac{1}{2} \rho A C_p v^3 \quad (2.3)$$

The maximum value of C_p is defined by the famous Betz limit theory [2], which proves that a turbine can convert to maximum efficiency of 59.26 % from the available power in the air stream.

Wind power is among the renewable resources that have utmost favorable technical and economic prospects [2]. For diversifying the energy market, wind energy is therefore among the most rapidly growing RES. Moreover, wind turbines are also among the most cost-effective renewable energy technologies, producing electricity with no fuel and minimum pollution. For these reasons, several wind power plants are being constructed around the globe with both offshore and onshore schemes. Usually, wind project sites are identified based on the wind atlas information of wind speeds, which is then confirmed with local measurements, such as the wind mast, at least for one year. Wind energy sources have undergone fast expansions worldwide in recent decades. At the end of 2020, the amount of installed wind power worldwide reached 743 GW [15]. The expansion of the newly installed capacity in 2020 was the best year in the global wind industry history showing year-over-year growth of 53 % that accounts more than 93 GW installed capacity as in Figure 2.2 [15].

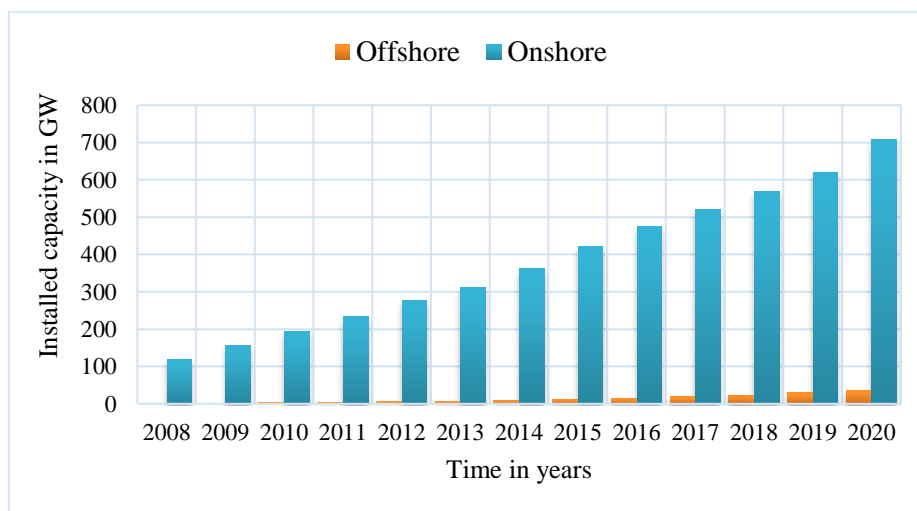


Figure 2.2 Historic development of total installations of wind power in the world [15]

Germany is among the countries which have successfully integrated higher shares of wind capacity into their national grids. Wind power in Germany is rapidly growing and accounts for 26.9 % of the gross power production in the year 2020 as presented in Figure 2.3 [16].

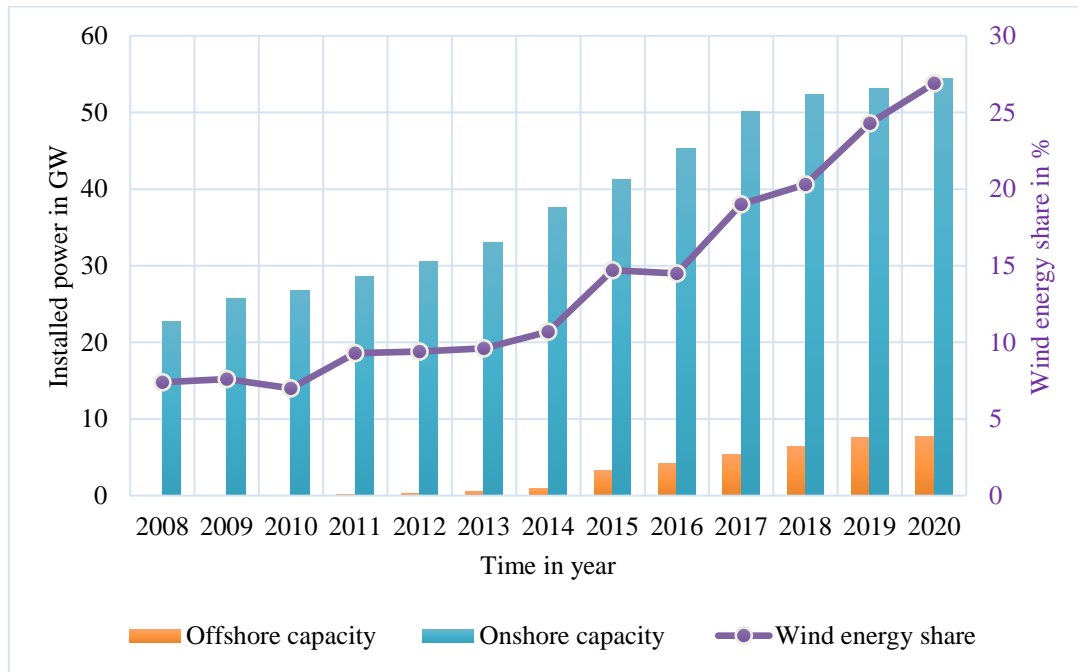


Figure 2.3 Historic development of Germany’s grid-connected wind power installations [16]

Wind power in Ethiopia is also increasing and many wind power projects are underway as stated in the master plan [9]. Figure 2.4 shows the operational onshore wind power commencements into the EEP’s network.

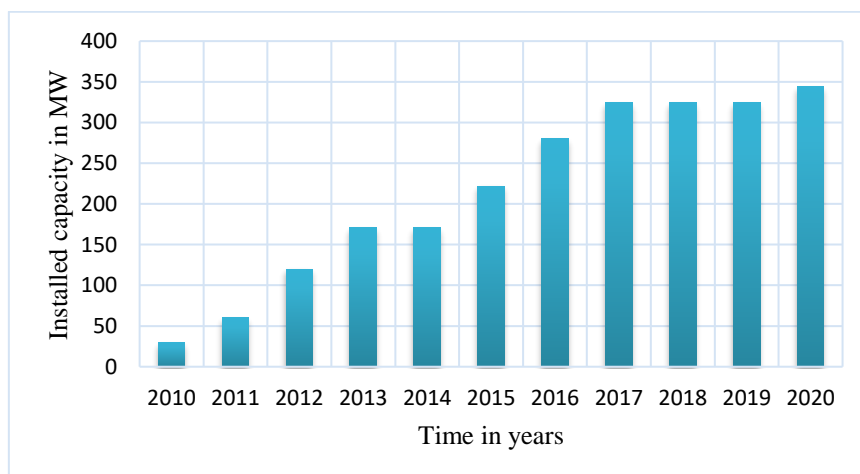


Figure 2.4 Historic development of Ethiopia’s grid-connected wind power installations [8]

Therefore, wind industry has radically increased not only its capacity share but also the conversion process and performance are significantly improved over the last decades. In this regard, wind energy technology has evolved rapidly with increasing rotor swept area and the use of power electronic converters to allow operation at variable rotor speed. Figure 2.5 shows the evolution of wind turbine technologies that illustrates how the swept-rotor area and the unit size of wind turbines are radically upgrading [5].

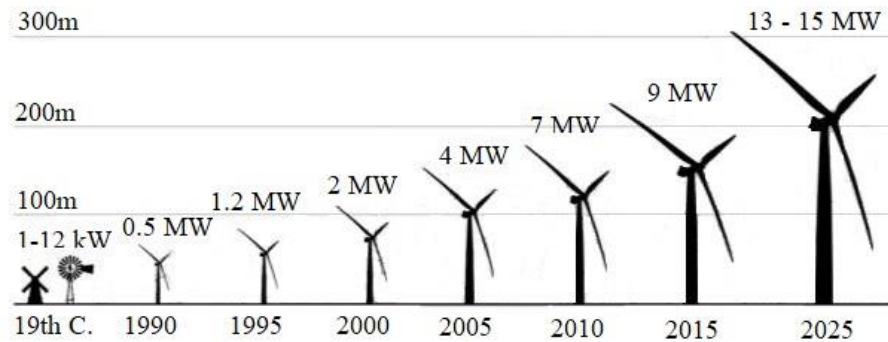


Figure 2.5 Evolution of wind turbine dimensions [5]

Today, there are actually various wind turbine concepts. Some of the important classifications are the way, the active power is controlled and the way the various types of wind generators are connected to a grid system.

2.3.1 Aerodynamic power regulation

The output power of a wind turbine is controlled using stall or pitch regulation techniques. In stall (passive stall) regulated wind turbines, the rotor blades are locked onto the hub at a fixed angle. While the rotor blades are aerodynamically designed to ensure the optimal geometric profile for wind speeds below rated value while creating turbulence on the side of the rotor blade when the wind speed becomes too high. Such stall mechanism is limited to regulate smoothly the output power for wind speeds above the nominal values. Moreover, stall control has a complex aerodynamic design and design problems related to structural dynamics of the overall wind turbine [4]. Hence, stall regulations are not currently employed in modern wind turbines.

The other method how the aerodynamic power can better be controlled is by turning the blades position in such a way, that the wind incidence blade area is reduced, once rated wind speed is attained. This power regulation is named as pitch control system. In pitch control method, the wind turbine can change incidence of its rotor blades based on the real-time wind speed so that the output power is adjusted and higher utilization efficiency is achieved. When the undisturbed wind speed is less than rated speed, the blade stays near the pitch angle 0° (which delivers optimal power). In other words, the wind generator

with constant pitch generates an output power that tracks the wind speed. This control strategy of the wind turbines is named as full load operation. However, if wind speed is above rated speed, the pitch control system acts and changes the rotor blade angle, usually in steps of 2° to 5° , so that the output power is regulated to the nominal turbine capacity [4].

The third type of aerodynamic power control combines the application of both the stall and pitch control methods and is known as active stall of wind turbines.

2.3.2 Wind generator integration concepts

Based on the generator type and grid electrical connections, there are four most relevant wind turbine types which have been commonly being installed in the industry [17], [18]. Figure 2.6 shows fixed-speed wind generators which are directly connected to the grid. This type of wind turbines are outdated technologies and are no more employed in the modern wind industry due to their limited capability for variable wind speeds. On the other hand, the variable-speed wind turbines which have either a slip-ringed induction generator and partial load converter in the rotor circuit or full power converter between stator circuit and the grid as designated in Fig. 2.7.

Type 1 wind turbines, shown in Figure 2.6, operate at fixed-speed which are usually comprised of squirrel cage induction generators (SCIG). The aerodynamic power is usually controlled using passive aerodynamic stall blade control [18].

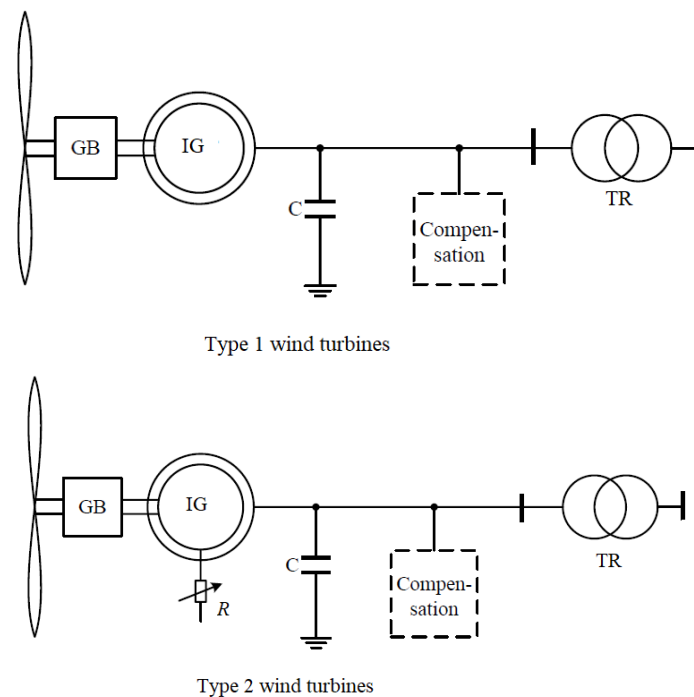


Figure 2.6 Constant speed wind turbines (Type 1 and Type 2) [17]

Type 2 wind turbines are built with wound rotor induction generator and are allowed to operate within a limited speed range. The speed variation in Type 2 is realized using controlled resistors in the rotor circuit. Pitch control is generally used for regulating the aerodynamic power. Unlike the Type-1, the Type-2 wind turbines have capacitor banks and power electronics which are used to control the reactive power [17], [18].

Type 3 wind turbines have variable rotor speed achieved by wound rotor induction generator (WRIG) and a back-to-back converter on the rotor-side [17]. Such converters are named as partial load converters (PLC). The converter control associated with the rotor circuit allows an independent control of active and reactive power for wide rotor speed operating range. Such type of wind turbine is called Doubly-fed induction generator (DFIG), as both rotor and stator can feed power into the grid as shown in Figure 2.7. Pitch control is widely used for regulating the aerodynamic power output of such variable rotor speed wind turbine (VSWT) [17], [18].

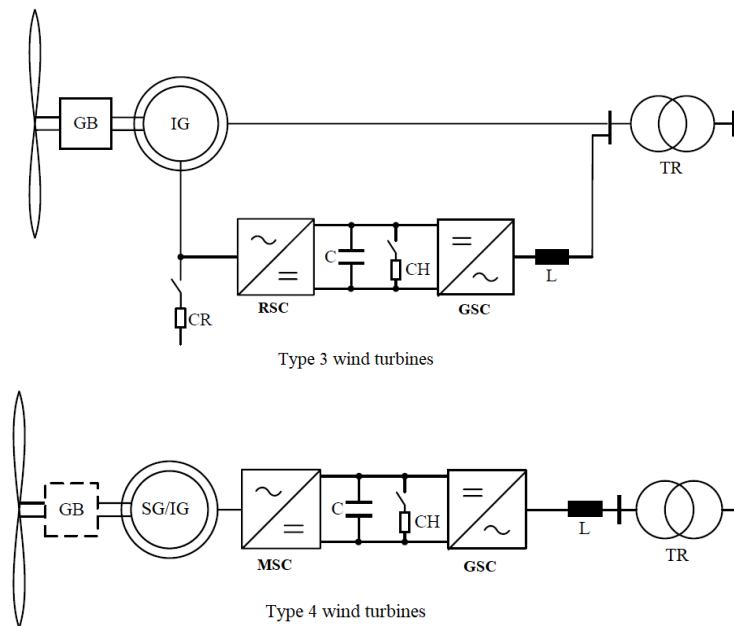


Figure 2.7 Variable speed wind turbines (Type 3 and Type 4) [18]

Type 4 wind turbines are connected to the grid via power electronic converters at the stator side of the generator. All the power from the generator passes through the converter and they are referred to as full-load converter (FLC) turbines. The most common types of such generators are wound rotor synchronous generators (WRSG), permanent magnet synchronous generators (PMSG) and SCIG. Depending on the generator type, a gearbox (GB) may or may not be employed. Type 4 wind turbines generally use pitch control for regulating the aerodynamic power output [18].

Wind turbine generators are evolving greatly to better accommodate variable rotor speed operation and so the Type 3 and Type 4 are dominating the wind industry [2], [4], [18].

2.4 Challenges of wind power generation

This subsection discusses on literatures that have contributed to improve methods related to the challenges in integrating large-scale wind power plants into power systems. Numerous studies have been explored on the requirements of power controllability during ordinary operation and in the event of grid abnormalities to consent some degree of control over active and reactive power generation, leading to the development of a new generation of wind energy conversion system such as the variable speed wind turbine systems [19], [20]. Variable speed wind turbines (VSWTs) are the new and most common norms for installing wind power plants. VSWTs have generally high efficiency in capturing energy comparing to the constant speed wind turbines with effective voltage control [21]. The DFIG and PMSG with AC-to-AC power converter technologies have become the most widely used wind turbines. DFIG has usually a gearbox and only 20 to 30 % of the wind turbine's nominal power is required for regulating its rotor speed that ranges from 0.7 to 1.3 per unit. In this regard, PMSG which have full converter capacity incurs superfluously higher capital cost comparing to the DFIG types [21].

The configuration of DFIG with four-quadrant back-to-back (BTB) converter connected to the rotor windings provides noticeable advantages over other wind turbines such as independent (decoupled) converter control of active and reactive generator power. The independent active and reactive power control scheme helps to regulate the frequency and voltage separately which ultimately improves the system performance efficiency [19]. The rotor power converter operates at higher frequency switching of pulse width-modulation (PWM) to achieve better control performance, that compromises both fast dynamic response and low harmonic distortion of converter control [19].

The dynamic behavior of power systems is significantly determined by the interaction of the generators in the system. Induction generators (IGs), as compared to synchronous generators are limited and act differently in respond to disturbances such as changes in terminal voltage and frequency. Moreover, induction generators have limited capability to contribute to grid voltage control [2], [19]. During large disturbances, IGs may accelerate the rotor speed during fault events and as a result draw huge amounts of reactive power from the grid, which could possibly result in voltage collapse [20]. Despite such circumstances, wind turbines comprised with IGs are widely used in modern power systems due to their robust, simple design, and cost-effective performance [2].

As long as the penetration level of wind power is in the low range, the behavior of the power system can be managed by conventional generators [2], [22], [23]. When more

controllable generators are replaced by uncontrolled generators, it is becoming more difficult for the power system to follow the variable nature of power demand. Thus, when the penetration level of wind power is increased, the dynamic performance of the grid can be affected as the dynamic behavior of wind generator is quite different to that of synchronous generators [22].

Previous researches have realized the dynamic characteristics of wind turbines and their impacts on power systems with high-wind capacity penetration levels [22], [23]. Grid integration impacts of IG-based wind turbine system have been well studied in [20]. In [19], the IG-based wind generators have been detected to observe reactive power from the system which resulted in decrease of voltage stability margin. Dynamic modeling and performance of DFIG-based wind turbine and its controller schemes, to enhance the transient stability of a power system, have also been discussed in [24]. The study in [24] has figured out that the DFIGs are much better than the IG-based wind generators in the steady-state operation. However, the DFIGs have still great influence when the system is subjected to large disturbances where the DFIGs are returned to induction generator operation scheme.

Voltage instability and collapse typically occurs when power systems are not capable of sustaining the dynamic balance of reactive powers due to heavy load changes and fault conditions [23]. Voltage collapse is considered as the main problem associated with wind power [22]. This problem can limit the amount of wind power, which can be installed and interconnected to the power networks. The system voltage fluctuations may cause voltage dips depending on the frequency and magnitude of the fluctuation. A voltage dip, caused by wind turbine operation, should be limited to comply with network code boundaries [25]. However, such effects can be reduced using variable speed wind generators as discussed in [22]. The findings in [5], [22] - [24] indicate that reactive power supply at the wind farm's point of connection is important to maintain the rated voltage on the network during normal and abnormal conditions. These researches investigate the dynamic voltage collapse points by employing various penetration levels of wind generations. However, reactive power compensation must be fast enough to correct the voltage dip. The studies are solely on voltage collapse and limited to demonstrate an integrated impact of the real-time frequency and voltage transients for various network topologies. Most of these researches deal with the impacts of voltage stability on the wind turbines and are also inadequate to present what amount of stability margin is reduced when a specified amount of controlled power generation is replaced by wind power.

In recent years, certain countries have formulated grid codes which define the specific requirements that a wind farm must fulfill in order to connect to their national grids. During normal operation, wind turbines usually operate in a voltage band between 0.9 and 1.1 per unit and a frequency between 49 and 51 Hz conditions [2], [26]. Thus, capabilities of contribution in voltage regulation by continuous modulation of reactive power supply to grid is one of such requirements [2]. The grid code in some countries also state that under power system fault conditions, a wind farm must not disconnect from the grid for a specified time period and fault magnitude [27]. Moreover, there are additional requirements related to sudden grid frequency variations, voltage dips, flickers, harmonics and telharmonic in [28], [29].

2.4.1 Wind generator voltage control strategies

As pointed out above, voltage problems are very common in power systems with high share of wind power particularly, typically in weak grids. Hence, correction measures must be taken to alleviate the voltage problem using fast acting reactive power compensation such as the flexible alternating current transmission systems (FACTS) [25]. FACTS made of power-electronic devices, are installed in an AC transmission networks to improve the voltage stability. Moreover, FACTS are used to enhance power transfer capability and controllability of power system through series or shunt compensation applications. The typical series compensation devices include the thyristor-controlled series capacitor (TCSC) and static synchronous series compensator (SSSC), which are mainly used to increase the power transferability of AC transmission networks [30]. The most common shunt compensation FACTS are static synchronous compensator (STATCOM) and static VAR compensator (SVC) [25], [30]. The shunt compensation devices are mainly used to boost the voltage dips in specific location of a network. The shunt-connected devices provide fast reactive power/voltage control capacity at a bus, whereas the series-connected device reduces series reactance of a transmission line to increase the line transfer capability [30].

Among the FACTs family, STATCOM is the most widely used technology that can be used to support transient stability so that dynamic voltage collapse can be prevented in wind farms. STATCOM is employed based on either as current source converters (CSC) or voltage source converters (VSC) [25], [31]. STATCOM, as compared to the thyristors-based compensators, is cost effective. STATCOM with controlled source of current have the capability of delivering any sort of reactive current in real-time [31].

In this thesis work, a simplified controlled current source model, intended to compensate the reactive power deficiency during the transient disturbance, is designed and integrated to the DFIG-based wind power plant. The wind turbine generators are modeled with fast-

responding STATCOM and rotor over-speeding capability when there is a substantial stator voltage-dip. A joint application of the modified STATCOM and rotor over-speeding capability of DFIG-based wind generators are applied to overcome the voltage dip challenges introduced by transient disturbances.

2.4.2 System balancing with wind power

The power generated from a wind farm is injected into the grid at a point of connection (POC) and together with other power generations supply the demand in the network. The total generated power should be equal to the total load plus the network losses in order to keep the rotor swinging speed of synchronous generators at their equilibrium positions. When the imbalance between generation and load is sustained for longer time without correction, the system frequency will be subjected to large deviations from its nominal value of 50 Hz (e.g., in the European grid system) and 60 Hz (e.g., in the USA grid). Such active power imbalance jeopardizes the stable operation of the system and leads to activation of protection devices which may disconnect either generators or loads or parts of the network in response to large frequency deviation.

The current wind generators are designed to operate at the maximum power point (MPP) which limits wind turbines to participate in frequency restoration process [2], [32]. In this thesis work, a frequency control module is integrated at a plant level to respond to the grid frequency oscillations. An oscillating frequency condition can be occurred due to load change and other disturbances in the network.

2.5 Wind turbine and control structure

As pointed out in the introduction section, WTGs are generally classified into four core types as fixed-speed with generator directly connected to the grid and variable-speed with either a slip-ringed induction generator and converter in the rotor circuit or a generator with full power converter in the stator circuit [2].

It is obvious, that FSWTs have the advantage of being simple and cost-efficient compared to VSWTs. However, the active power and reactive power consumption cannot be independently controlled. FSWTs are also highly affected by wind speed fluctuation which is transmitted into the shaft torque and finally transferred into the electrical power on the stator circuit [33]. Such fluctuation in the output power transfer to the grid can lead to large frequency and magnitude fluctuations [33]. Therefore, VSWTs specifically DFIG-based wind turbines are dominating the wind industry [34]. That is, because a DFIG-based wind turbine, with partial power electronic converter, performs comparatively smooth grid integration by regulating the active and reactive power flow to and from the

electrical generator [34]. Therefore, in this thesis work, the DFIG-based wind turbine is considered to present the impacts of wind power on power system dynamic stability.

The dynamic wind turbine models are highly dependent on the focus and interest of the intended analyses. For instance, a very detailed aerodynamic and structural models with correspondingly detailed wind generator and control models are necessary for wind turbine design and for issuing the manufacturer type certification purposes. For the use in electrical dynamic simulation studies, such transient stabilities near to fundamental frequency, detailed aerodynamic models are usually not necessary [2]. As the purpose of this research is intended to investigate the dynamic impacts of wind generators in an existing large grid, it is rational to reduce the complexity of the system model by applying reduced-order models. As the intention of the simulation is on fundamental frequency range, the drive trains are adequate to be represented by a lump-sum as one rigid system [26].

Representing the synchronous generators in 4-th order model is sufficient to characterize the dynamic behaviors of the machine for transient analyses at fundamental frequency [35]. The synchronous machines in conventional power plants are made to include the simplified models of automatic voltage and frequency regulations. On the other hand, induction machines are composed of stator and rotor windings like the synchronous machines. However, unlike the synchronous machines, induction generators can operate in super-synchronous mode with rotor speeds greater than the synchronous speed and under-synchronous mode when the generator rotor speed is slower than the synchronous speed. Induction generators can operate in a variable rotor speed which is described by the slip ratio of the generator rotor. Hence, the induction machines are fully represented by their stator and rotor transients.

In this thesis work, the DFIG-based wind turbine is made to comprise three main control levels. The first level is the converter control unit that regulates the generator output active power, reactive power and terminal voltage. The second level is the WTG control unit that controls the turbine mechanical power based on the wind speed and the desired rotor speed. The third control hierarchy is at the wind power plant level to regulate and set the reference inputs for the converter control system. Moreover, a protection system is also integrated into the wind turbine model to protect the components from operating beyond their limits. For example, the converter maximum power is set to 30 % of the machine rating so that the control currents for the converter are accordingly restricted. Hence, the proposed DFIG-based wind turbine model has also incorporated a trip signal if the wind speed is beyond the cut-in and cut-out and also if the voltage dip and rotor currents (in-rush current) are beyond their limits for longer time. The adopted general

control structure and levels of the DFIG-based wind power plant is designated in Figure 2.8.

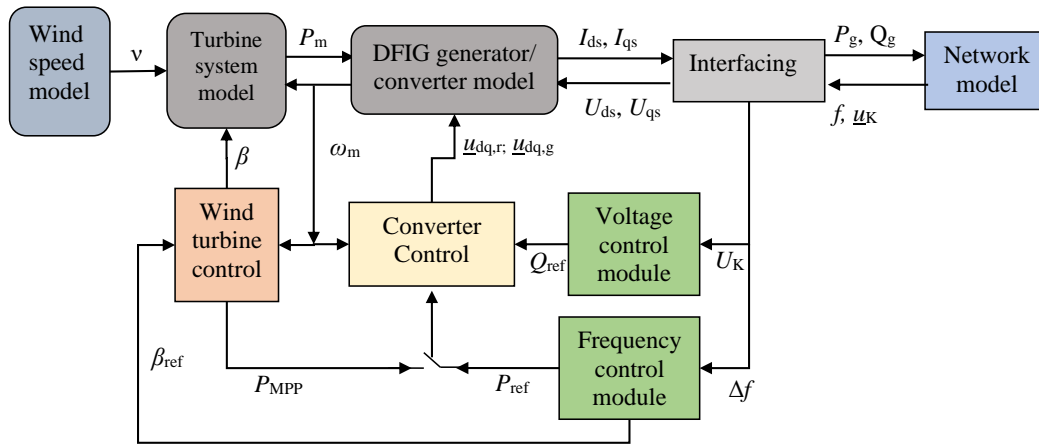


Figure 2.8 General architecture of DFIG-based variable speed wind turbine control strategies

Due to the complexity and simulation computational time, the DFIG-based wind turbines are aggregated into a large generating unit which has equivalent dynamic behaviors like the single units in the array. Hence, wind power plants are aggregated in such a way that the load flow results in the grid are maintained in the steady-state operation. In other words, the wind speed of an aggregated wind generator is generally kept constant during the time simulation at its value that corresponds to the steady-state equilibrium. The total power calculated from load flow at the wind generator terminal is shared to the aggregated arrays within the wind farm as per the optimal power corresponding to the wind speeds.

The set of differential algebraic equations (DAEs) for the machines/controllers and the network equations are solved through numerical methods using the simultaneous method or partitioned method [36]. In this thesis work, the partitioned approach is implemented by applying the 5th- and 6th-orders of Runge-Kutta techniques.

3 Mathematical Modeling of Power Systems

3.1 General

Power system dynamics essentially require detailed study of network dynamics so that various elements in the grid are smoothly interconnected to each other and safely operate. The network dynamics are influenced by the dynamic behaviors of the generators, transmission lines, transformers, loads and other control elements. The dynamic behaviors of power networks could be quite complex in reality and a better comprehension is essential, specifically, for system planning concepts where projecting the system reliability, security and stability are more essential [37]. Power supply reliability does normally imply much more than just being available. The first commitment of reliable supply is to keep all running generators connected in parallel with sufficient spinning reserve to meet the peak load demand. The other requirement of reliable service is to ride through during abnormal conditions. For instance, if at any time a line is tripped or a generator loses synchronism with the rest of the system, this may result in significant frequency, current and voltage fluctuations which lead to automatically activate relays of transmission line and follow by abnormal conditions.

Modelling can be created using the actual structure and fundamental physical laws governing the power system components. The mathematical dynamic model of a power system is the basis for power system analyses. Of course, it doesn't have universal character but reflects specific phenomena of interest. Power systems are generally composed of transmission lines, shunt/series capacitors, transformers and other static elements.

Generally, the rate of change of state variables with respect to time analyses are usually performed through two types of simulations [38]. They are termed as:

- Electromagnetic transient (EMT) simulation
- Root mean square (RMS) or phasor simulation

EMT models represent a power system at all frequencies that include the transient problems such as lightning, switching and temporary over-voltages, inrush currents and sub-synchronous resonances [38]. However, when sinusoidal signals are written in phasor form, the differential equations can be represented by algebraic equations, hence they become easier to solve, take less time and are easy to analyze as the phasor equations can be split between real and imaginary parts. The idea of RMS is basically to analyze the dynamics of machines or controllers in power system by simplifying the network equations as it is computationally expensive to simulate large grids in EMT. The RMS simulation can be performed with less data whereas EMT simulation requires a complete dataset which is usually hard to get. Whereas, the intended target of this research work is

mainly to study the dynamic behaviors of bulk power networks for planning and operation purposes, the RMS model of synchronous generators, induction machines of the wind turbines, control elements and loads are sufficient to be considered.

Hence, the multi-machine power system transient stability analysis is studied by performing RMS time-domain simulations. The main components of the power system such as the network transmission system, synchronous generators, wind turbine induction generators, control elements, etc. are represented by their dynamic equations (in phasor or complex forms). The power system elements are modelled using the orthogonal phase representation (RMS method), with the assumption that the balanced/ unbalanced three phase system are characterized by their equivalent phasor representation in the alpha-beta coordinate ($\alpha\beta$ -axes), where the zero component is neglected [39], [40]. These models are used throughout the thesis work to present the time-domain simulation results in the preceding sections.

Power system models are generally formulated with two terms: the system equations and the system state. The system equations are the set of equations that describes the physical behaviors of a system. The system state is a set of variables that uniquely describe the condition of the grid and allowing to easily derive every other information of interest. The state variables are named as x_1, x_2, \dots, x_n or written as $\mathbf{x} = [x_1, x_2, \dots, x_n]^T$ which is referred to as the state vector. A given system is named as static, when the state variables are time invariant and the variables are termed as x_1, x_2, \dots, x_n . A system is dynamic, when the state variables are time variant, that is $x_1(t), x_2(t), \dots, x_n(t)$ [41], [42], [43].

A power system is essentially stressed by its dynamic subsystems. It is a challenge for transmission system operators (TSOs) to supply reliable, secured and stable electricity to their customers. Power system security and stability assessments are essential to avoid catastrophic consequences of system disturbances which may result in system blackouts. The accuracies of power system assessments are dependent on the precision of the employed models [11], [41]. To implement such assessments, the state variables have to be determined at steady-state conditions and these variables must remain at equilibrium point as far as there is no significant system disturbance. When the system is subjected to disturbance, the state variables will oscillate and settle to a new or previous equilibrium point if the system is stable while remain changing if the system is instable. Therefore, for assessing the system security and stability, there are two important analyses, namely the power flow and the dynamic analyses.

Power flow calculation basically defines the steady-state analysis of power networks. In power flow analysis, the steady-state values of bus voltages (bus profiles) and line power flows are computed for the given electric loads and generations. The Power flow solution

of grid network defines the network steady-state operation and the initial values of the dynamic equations which are evaluated at the equilibrium point for further time-domain simulation studies. For performing the steady-state and time simulation analysis the power network components shall be modeled as per the interest of study. Hence, the goal in this thesis work is to examine the influence of wind power share on the system dynamic behaviors, the major elements of the power network are modeled for a fundamental frequency transient analysis.

The dynamic models of power network components are categorized in three main subsections. The first section is modeling of the network components which are useful for steady-state analysis. This section includes models of the transmission lines, transformers and loads. The second category is modeling of the conventional stations with synchronous generation and the third category is modeling of the wind power plants associated with asynchronous generators, which is presented in a separate section as in chapter 4. Then after, the transient stability analysis will be studied based on the WTGs along with the other power system dynamics through which the impacts of wind energy increase in power system are investigated and mitigation measures are proposed.

3.2 Modelling of transformers, transmission lines and loads

As major elements, AC power networks consist of generator systems, loads, transformers and transmission lines. A power network can be modeled by a bus admittance matrix. Modern electric power systems are basically comprised of thousands of buses and therefore, such bus admittance matrix is usually large and sparse. The methods of representing and analyzing the power system components have significant influence on the system analysis. In this subsection, three components of the electric network, named afterwards, are modeled and their mathematical representations for the dynamic analysis are discussed. However, the model and analysis of synchronous generator systems will be implicitly presented in the next subsections.

3.2.1 Transmission line

Transmission lines are premeditated to efficiently transfer electric power from generation stations to load centers or from one substation to another over medium or long distances. Transmission lines usually operate at extra high or high voltage levels in order to reduce the resistive losses [44]. Such medium or long transmission lines can accurately be represented by a nominal π -model with series and shunt admittances [11]. The series and shunt admittance behaviors of a line, with respect to its terminal measurements taken at

its two ends, is shown in Figure 3.1 [45]. The admittance matrix of such black box representation of a quadrupole is given in (3.2), where \underline{Z}_{AB} is lump summed series impedance of the line and $\underline{Y}_{AB,L}$ is the admittance matrix of the line between point A and B.

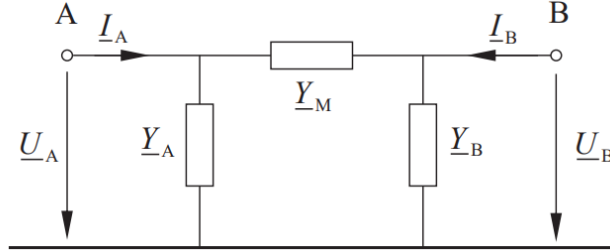


Figure 3.1 Equivalent circuit diagram of a line [45]

$$\underline{Y}_A = \underline{Y}_B = \frac{1}{2}(G + j\omega C) \text{ and } \underline{Y}_M = \frac{1}{\underline{Z}_{AB}} = \frac{1}{R + jX} \quad (3.1)$$

The admittance matrix of the line between bus A and B is derived in [45] as:

$$\underline{Y}_{AB,L} = \begin{pmatrix} \underline{Y}_A + \underline{Y}_M & -\underline{Y}_M \\ -\underline{Y}_M & \underline{Y}_B + \underline{Y}_M \end{pmatrix} \quad (3.2)$$

Where, R is the series line resistance in Ohm, X is the line inductance reactance in Ohm, C is the shunt line capacitance in Farad, G is the shunt line conductance in Siemens, \underline{Y}_M is the series line admittance in Siemens, \underline{Y}_A and \underline{Y}_B are the lump summed shunt admittances in Siemens at points A and B, respectively.

3.2.2 Transformer

Power transformers are used to enable power transfer with minimum losses at different voltage levels between generator sending end to load centers at the receiving end. Moreover, transformers which have taps are also used to regulate the voltage and reactive power flow by changing their transformer turns ratios [41].

Transformers allow to efficiently transfer the power from the primary to the secondary side with minimum losses in the transformer windings. A power transformer with turns ratio \underline{t} changes its current by a ratio of $1/\underline{t}^*$. Reducing the current in the secondary part will decrease losses in the line and allows power transmission with minimal loss over a long distance. The general equivalent circuit diagram of a two-winding transformer, with a T-model type, is adopted in this thesis work. In the T-model type, the equivalent circuit of winding B is related to the rated voltage of winding A as depicted in Figure 3.2 [45].

Back transformation of the related voltages and currents is done using an ideal transformer with the transformation ratio $\underline{\tau}$ which is used to model regulation, tap changing and phase shifting.

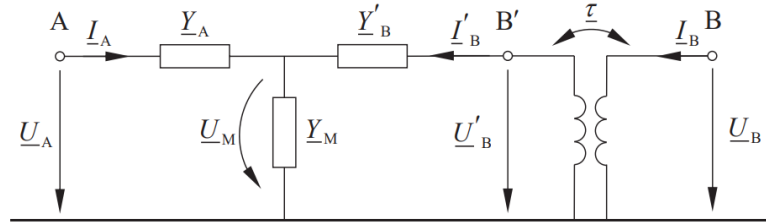


Figure 3.2 T-Model transformer equivalent [45]

The high voltage side winding leakage reactance \underline{Y}_A , the low voltage side leakage reactance referred in the high voltage \underline{Y}'_B , and the shunt admittance due to magnetizing current and iron core resistance \underline{Y}_M are presented in [45] as:

$$\underline{Y}_A = \frac{1}{R_A + jX_A}; \quad \underline{Y}'_B = \frac{1}{R'_B + jX'_B}; \quad \text{and} \quad \underline{Y}_M = \frac{R_{Fe} + jX_h}{R_{Fe} jX_h} \quad (3.3)$$

Then, the admittance matrix of the T-equivalent circuit of a two-windings transformer is defined in [45] as:

$$\underline{Y}_{AB,T} = \frac{1}{\underline{Y}_A + \underline{Y}'_B + \underline{Y}_M} \begin{pmatrix} \underline{Y}_A (\underline{Y}'_B + \underline{Y}_M) & -\underline{\tau} \underline{Y}_A \underline{Y}'_B \\ -\underline{\tau}^* \underline{Y}_A \underline{Y}'_B & |\underline{\tau}|^2 \underline{Y}'_B (\underline{Y}_A + \underline{Y}_M) \end{pmatrix} \quad (3.4)$$

For simplicity and consistency purpose, in this thesis work, three-winding transformers are represented by three equivalent two-winding transformers formed from the three coils of the three-winding power transformer.

3.2.3 Loads

As discussed in [11], loads are classified into three groups i) constant power loads, ii) constant impedance loads and iii) constant current loads. During steady-state operation, the bus voltages remain in normal operating ranges and the loads usually behave like constant impedance type. Hence, when computing power flow analysis, the steady-state values of the bus voltages are within normal operation and so the loads can be represented as constant impedance. Loads are basically named as active power and reactive power loads. However, in transient analysis the bus voltages are varying beyond the normal range and so the loads are not at constant impedance. The loads that depend on voltage and frequency are named as composite loads and they form dynamic system loads [11].

In such composite loads, the constant impedance type is applied and any load deviation is modeled by a simple first order equation. For this reason, in this thesis work, loads are represented as constant impedance type with voltage dependency model.

3.2.4 Protection system

Power systems are employed with protection systems which comprise a variety of defensive devices such as voltage relays, current relays, power sensors, fuses, and circuit breakers. Such protective devices are directly connected to the circuits at substations/switch-gears as instrument transformers, circuit breakers, disconnect switches, fuses, and lightning arresters. These protective devices are essential in order to de-energize the power system either in scenarios of normal operation or in case of failures of the power system due to overloads or faults [11], [44].

When conventional generation systems are dominating the power supply, there are solutions in place to instantly correct and monitor overload and fault events. Such robust facilities prevent the catastrophic phenomena of the system [44]. During periods of severe faults, where high currents occur, the entire power system is potentially threatened, unless fast measures are in place. For this reason, the application of relays is employed, specifically for wind turbines units, to automatically isolate and protect the wind generators from fault conditions beyond the grid code boundaries [44].

3.3 Modelling of the conventional generation stations

Conventional generation stations are fundamental electric power plants where different primary energy sources are converted to electrical energy and transferred to the load centers via transmission networks. The major components of conventional power stations are synchronous generators, excitation systems, turbine-governor systems and switch yards [11], [41]. Each of these elements are discussed and their models are presented in the succeeding subsections.

3.3.1 Synchronous generator model

The dynamic behavior of synchronous generators is described in several mathematical models such as [11], [12], [36], [41] - [43]. For transient analysis of large networks, most of them deal with the classical model or the swing dynamics and therefore lack higher frequency transients. However, modern electric networks are becoming more complicated to analyze due to the increased complexity of operation and control with power electronics, e.g. in the case of wind generations with partial/full converters, that contribute high frequency transients into the system.

Synchronous generators (SGs) are still the main source of energy within modern electric networks, which can be modelled with varying levels of complexity [41]. SGs are modeled with several dynamic variables for studying and enhance the system stability [41]. The SG, as one of the most vital system components, must be modelled mathematically in an adequate manner to represent the power system dynamic for security and stability studies. As integrated research of the thesis work, comparison of different order of synchronous generator's models were investigated in reference to the 6th- order model and the results show that the 4th- order model is sufficient to represent the synchronous generators for a fundamental frequency transient stability analysis [35]. Thus, the synchronous generator, in the thesis work, is modeled with 4th- order and the details are explained in the next sub-sections.

A synchronous generator has two magnetically coupled windings placed in the stator and rotor parts. A three-phase synchronous machine can be modeled in the rotor frame of reference as shown in Figure 3.3. The stator fluxes are transformed using Park's transformation [12], [36] and are represented by virtual windings in the d- and q-axes as a machine-frame of reference. Figure 3.3 depicts two fictitious d- and q-stator windings representing the three-phase armature windings on the stator. Figure 3.3 also depicts the field winding 'f-coil', and one rotor damping coil along q-axis as 'g-coil'. This representation of the rotor circuits is named as the 4th- order model as in [35].

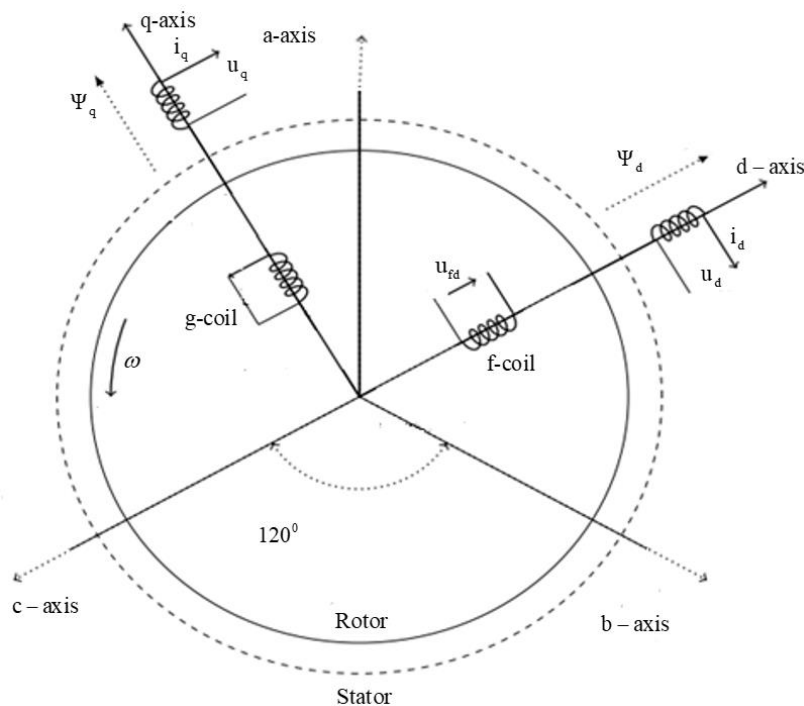


Figure 3.3 Model of synchronous generator - 4th order [41]

3.3.1.1 Rotor voltage equations

The rotor flux linkages either remain with rotor coils closed (the damper windings) or are closed through a finite voltage source (the field winding) [11]. These real two rotor coils (g- and f-coils), shown in Figure 3.3, along the d- and q-axes are considered as state variables and are modeled in state space form as expressed in [36], [41]:

$$\begin{aligned}\frac{d\psi_{d,f}}{dt} &= \frac{1}{T'_d} \left[-\psi_{d,f} + \psi_{d,s} + \frac{X'_d}{X'_d - X'_d} U_{d,f} \right] \\ \frac{d\psi_{q,g}}{dt} &= \frac{1}{T'_q} \left[-\psi_{q,g} + \psi_{q,s} \right]\end{aligned}\quad (3.5)$$

Where, $\Psi_{d,f}$ is the field winding flux linkage in the d-axis; $\Psi_{q,g}$ is the “g”-damper winding flux linkage in the q-axis; $U_{d,f}$ is the excitation control voltage input to the field winding in the d-axis; T'_d is the short circuit time constant in the d-axis while T'_q is the short circuit time constant in the q-axis.

3.3.1.2 Stator voltage equations

The two stator fictitious windings in Figure 3.3 represent the three-phase stator windings in the dq-axis frame. The equivalent stator flux equations are.

$$\begin{aligned}\frac{d\psi_{d,s}}{dt} &= -\omega_s R_s I_{d,s} - \omega \psi_{q,s} - \omega_s U_{d,s} \\ \frac{d\psi_{q,s}}{dt} &= -\omega_s R_s I_{q,s} + \omega \psi_{d,s} - \omega_s U_{q,s}\end{aligned}\quad (3.6)$$

Where $\Psi_{d,s}$, $U_{d,s}$, $I_{d,s}$; and $\Psi_{q,s}$, $U_{q,s}$, $I_{q,s}$ are stator fluxes, voltages and currents in the d-axis and q-axis, respectively; R_s is the stator resistance; ω_s and ω are the synchronous stator and rotor speeds, respectively.

In this thesis work, the generator convention is applied, i.e., positive currents for outgoing currents from the stator and ingoing currents to the rotor windings [11]. The algebraic equations of the stator and rotor flux linkages in terms of the currents for the stator and rotor windings are given in (3.7) as described in [11]:

$$\begin{aligned}\psi_{d,s} &= -X_{d,s} I_{d,s} + X_{d,m} I_{d,f} \\ \psi_{q,s} &= -X_{q,s} I_{q,s} + X_{q,m} I_{q,g} \\ \psi_{d,f} &= -X_{d,m} I_{d,s} + X_{d,f} I_{d,f} \\ \psi_{q,g} &= -X_{q,m} I_{q,s} + X_{q,g} I_{q,g}\end{aligned}\quad (3.7)$$

Where, $I_{d,s}$, $I_{d,f}$ and $I_{q,s}$, $I_{q,g}$ are the currents of the fictitious stator and rotor windings of Figure 3.3 in the d-axis and q-axis, respectively; $X_{d,s}$, $X_{d,f}$, and $X_{q,s}$, $X_{q,g}$ are steady-state inductance reactances of the stator and rotor windings in the d-axis and q-axis, respectively; $X_{d,m}$ and $X_{q,m}$ are the mutual inductance reactances induced between the damper windings and stator windings along the d- and q-axes.

In this analysis, the network transients are neglected. Moreover, the stator flux transients are fast comparing to the rotor flux transients and so it is realistic that the stator flux differential equations are neglected as proven in [11].

$$\frac{d\psi_{d,s}}{dt} = \frac{d\psi_{q,s}}{dt} \approx 0 \quad \text{and} \quad \omega \approx \omega_s \quad (3.8)$$

Using the assumption in (3.8) and applying it in the dynamic stator voltage expressions in (3.6), respectively, the stator equations become algebraic and by employing the flux equations in (3.7), the stator equations can be rewritten in terms of the internal transient generator voltage as derived in [35].

$$\begin{aligned} U_{d,s} &= -R_s I_{d,s} + X'_q I_{q,s} + U'_d \\ U_{q,s} &= -R_s I_{q,s} - X'_d I_{d,s} + U'_q \end{aligned} \quad (3.9)$$

Where, U'_d and U'_q are the dq-axes internal generator voltages behind the d-axis transient reactance X'_d . All generators, in this thesis work, are represented as a current source for studying the dynamic behaviors of the power networks. Thus, the rotor flux differential equations in (3.5) are transformed to their equivalent voltage equations by employing the dq-axes voltage expressions in (3.7) and (3.9) as given in [35], [41], [46].

$$\begin{aligned} \frac{dU'_q}{dt} &= \frac{1}{T'_{do}} \left[-U'_q - (X_{d,s} - X'_d) I_{d,s} + U_{d,f} \right] \\ \frac{dU'_d}{dt} &= \frac{1}{T'_{qo}} \left[-U'_d + (X_{q,s} - X'_q) I_{q,s} \right] \end{aligned} \quad (3.10)$$

T'_{do} and T'_{qo} are open circuit transient time constants on the d-axis and q-axis, respectively.

3.3.1.3 Transient saliency

The transient saliency is the effect of slots in the stator when the transient reactances in the d-axis and q-axis are different. In such cases, the synchronous generators are not easily

represented by an equivalent circuit. As explained in literatures, [12], [36], [41], the transient saliency can be treated either using the constant current source or dummy coil that characterizes the saliency in representing the stator scalar equations into single-phase phasor representation so that the transformation between the machine frame and the network is realized. In this thesis work, the dummy coil technique is considered, which requires to choose appropriate rotor/stator current flow direction and axis transformation.

The transient saliency for the 4th- order model can be determined by adding and subtracting the term $X_d' I_{q,s}$ in the stator voltage equations in (3.9) and gives the phasor representation of the stator as in (3.11).

$$U_{d,s} + jU_{q,s} = (U_d' + jU_q') - (R_s + jX_d')(I_{d,s} + jI_{q,s}) + (X_q' - X_d')I_{q,s} \quad (3.11)$$

If the dummy coil is represented as in (3.12),

$$U_{d,c} = (X_q' - X_d')I_{q,s} \quad (3.12)$$

Then the phasor representation of the stator voltage behind X_d' in the generator frame of reference is rearranged as:

$$U_d' + U_{d,c} + jU_q' = (U_{d,s} + jU_{q,s}) + (R_s + jX_d')(I_{d,s} + jI_{q,s}) \quad (3.13)$$

Thus, the dummy coil dynamic with constant time, T_c' can be represented by:

$$\frac{dU_{d,c}}{dt} = \frac{1}{T_c'} \left[-U_{d,c} + (X_q' - X_d')I_{q,s} \right] \quad (3.14)$$

Hence, using equation (3.13), the dynamic equivalent electrical circuit of the SG for the transient or sometimes called two-axis model, with transient saliency, is presented in Figure 3.4 [41]. The load angle δ is defined as the angle between the q-axis of the individual generator with respect to the real axis of the grid reference frame. Hence, the axis transformation angle between the dq-frame and the $\alpha\beta$ -frame is defined as $\delta - \pi/2$. The detailed axis transformation of the synchronous generators between dq-components and the common grid reference ($\alpha\beta$ -frame) is explained in the succeeding sub-section.

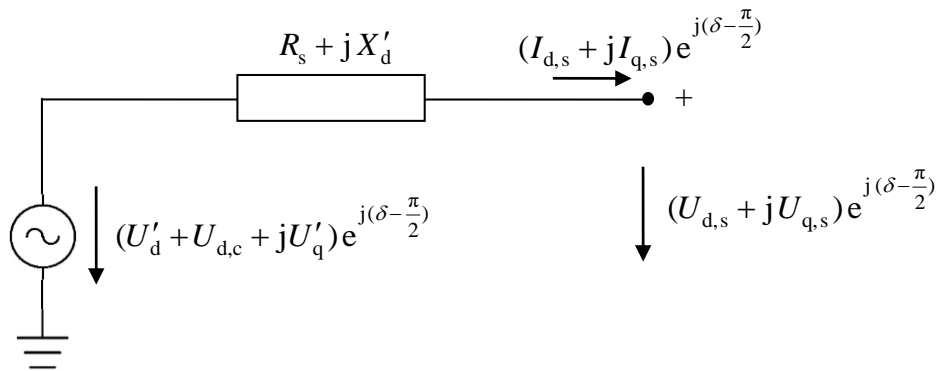


Figure 3.4 Dynamic equivalent circuit of synchronous generator with transient saliency [41]

3.3.1.4 The swing equations

The interaction of rotor dynamics (electromechanical), in terms of the rotor speed, during and after a few seconds of transient disturbance results in generator swing responses. Figure 3.5 shows that two torques are exerting in the opposite directions: on one side the mechanical torque from the turbine T_m and on the other end the electromagnetic torque T_{em} acting on the field windings that are located on the rotor. If the torques at the two ends of the generator shaft are equal then the machine remains in synchronism and is neither accelerating nor decelerating. However, in the real case there are at least small disturbances on both or either side and the machine is usually swinging.

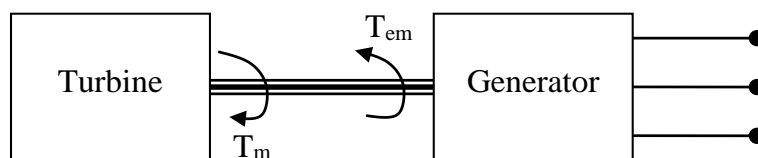


Figure 3.5 Schematic diagram to illustrate the interaction of rotor dynamics [43]

The rotor swing dynamics of synchronous generators are usually modeled by two first order equations along with mechanical dampers to accelerate much faster as in [12], [35], [43]:

$$\begin{aligned} \frac{d\delta}{dt} &= \omega - \omega_0 \\ \frac{2H}{\omega_0} \frac{d\omega}{dt} &= T_m - T_{em} - D(\omega - \omega_0) \end{aligned} \tag{3.15}$$

The induced generator electromagnetic torque, T_{em} in per unit is given by:

$$T_{em} = U'_d I_{d,s} + U'_q I_{q,s} + (X'_d - X'_q) I_{d,s} I_{q,s} \quad (3.16)$$

Where; H is the inertia constant of a generator in seconds, T_m is the mechanical input torque in per unit, D is the damping constant, ω is the rotor speed of the generator in rad/sec and $\omega_0 = \omega_s$ is the initial and base generator rotor speed in rad/sec. The stator currents, internal generator voltages and transient reactances in the dq-axes are all in per units.

Therefore, the complete 4th- order dynamics of the synchronous generator are represented by their differential equations in (3.10), (3.14) and (3.15) and the algebraic equations in (3.9) and (3.16) as in (3.17).

$$\begin{aligned} U_{d,s} &= -R_s I_{d,s} + X'_q I_{q,s} + U'_d \\ U_{q,s} &= -R_s I_{q,s} - X'_d I_{d,s} + U'_q \\ \dot{U}'_q &= \frac{1}{T'_{do}} \left[-U'_q - (X_d - X'_d) I_{d,s} + U_{d,f} \right] \\ \dot{U}'_d &= \frac{1}{T'_{qo}} \left[-U'_d + (X_q - X'_q) I_{q,s} \right] \\ \dot{U}_{dc} &= \frac{1}{T'_c} \left[-U_{dc} + (X'_q - X'_d) I_{q,s} \right] \\ \dot{\delta} &= \omega - \omega_0 \\ \dot{\omega} &= \frac{\omega_0}{2H} \left[T_m - T_{em} - D(\omega - \omega_0) \right] \\ T_{em} &= U'_d I_{d,s} + U'_q I_{q,s} + (X'_d - X'_q) I_{d,s} I_{q,s} \end{aligned} \quad (3.17)$$

In a conventional power plant, the outputs of synchronous generators are normally controlled to a desired active and reactive power reference by which the terminal voltage and frequency of the generator are regulated. As described in section 2.2, there are various types of conventional power plants which are derived by different types of primary energy sources. In this thesis work, the hydropower and steam turbine systems are considered for all test networks and case studies. Thus, the voltage regulation and turbine control system models, in this work, are concerning only to hydropower and steam-based conventional power generation.

3.3.2 Excitation system

The excitation system is a means that provides a regulated output voltage to the field windings of a synchronous generator. In this thesis work, two excitation models have been considered for regulating the grid voltage at the generator terminals. The excitations are simplified forms of fast acting static IEEE-Type ST1A and IEEE-Type DC1A standard excitors as described in [47].

The simplified fast acting ST1A exciter is employed in case of large networks that aims to study mainly the frequency regulations [13], [47]. The DC1A model is applied to evaluate network dynamics when there is interest in voltage stabilities. DC1A, comparing to ST1A, has incorporated a larger number of states and is better to represent the physical behavior of excitation systems which need more simulation time compared to the simplified first exciter.

3.3.2.1 Simplified model of static ST1A exciter

The schematic diagram of the simplified model for the IEEE ST1A static excitation type is shown in Figure 3.6. As described in [36], [41], IEEE-type ST1A is a single-time constant, fast acting with high gain static exciter that behaves like a proportional controller.

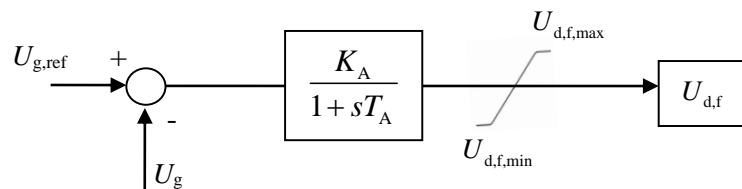


Figure 3.6 Single-time constant IEEE-type ST1A excitation system [36], [41]

The corresponding mathematical representation of such first-order controller is given in (3.18).

$$\frac{dU_{d,f}}{dt} = \frac{1}{T_A} \left[-U_{d,f} + K_A (U_{g,ref} - U_g) \right] \quad (3.18)$$

Where

$U_{d,f}$ is the output of the excitation controller; K_A is the excitation control static gain;
 U_g is the generator bus voltage magnitude; T_A is the excitation voltage time-constant

The excitation state variable, which is an instantaneous input voltage to the rotor exciter, is bounded to maximum and minimum values with limiter as $U_{d,f,min} \leq U_{d,f} \leq U_{d,f,max}$. The

steady-state reference value of such excitation voltage is calculated by setting the derivative equal to zero as in (3.19).

$$U_{g,\text{ref}} = U_g + \frac{U_{d,f}}{K_A} \tag{3.19}$$

3.3.2.2 IEEE-type DC1A

The IEEE-type DC1A excitation system, due to its simplicity comparing to others, is alternatively also used in this research thesis. DC-generators are the sources of such excitation power and provide current at the excitation voltage $U_{d,f}$ to the rotor windings of the synchronous machine through slip rings. The excitation voltage in such field-controlled exciter models is continuously regulated by a field-controlled DC commutator exciter. The structure of the IEEE-type DC1A excitation model is shown in Figure 3.7 and the dynamic mathematical equations are as follows [13].

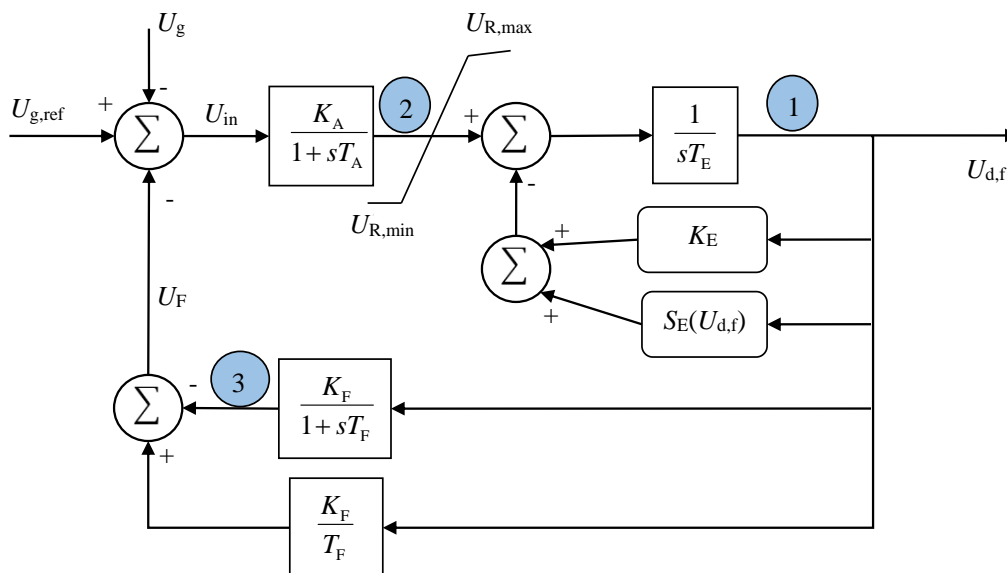


Figure 3.7 IEEE-type DC1A excitation system model [13] [36]

The state variables of the DC1A excitation system are $U_{d,f}$, U_R and U_F . The dynamic model of the DC1A excitation system is presented in (3.19) as in [13].

$$\begin{aligned}
 \frac{dU_{d,f}}{dt} &= U_R - (K_E + S_E(U_{d,f}))U_{d,f} \\
 \frac{dU_R}{dt} &= \frac{1}{T_A} \left[-U_R + K_A R_F - \frac{K_A K_F}{T_F} U_{d,f} + K_A (U_{g,\text{ref}} - U_g) \right] \\
 \frac{dR_F}{dt} &= -R_F + \frac{K_F}{T_F} U_{d,f} \\
 R_F &= \frac{K_F}{T_F} U_{d,f} - U_F
 \end{aligned} \tag{3.20}$$

Where $U_{d,f}$ is the excitation system output voltage; U_F is the rate of feedback to stabilize excitation voltage; U_R is the regulator voltage where $U_{R,\text{min}} \leq U_R \leq U_{R,\text{max}}$; U_g is the terminal voltage magnitude. All gains and time constants are defined and taken from [13].

3.3.3 Speed-governor and turbine systems

The modeling of the turbine system and speed governor is required to regulate the mechanical power as per the demand in the grid so that the rotor tends to rotate at synchronous speed. In this thesis work, a hydraulic turbine system model is presented and its simplified block schematic is shown in Figure 3.8 as in [36], [41], which is used for regulating the governor gate valve. The details of steam turbine and governor system models can be referred at [36], [41].

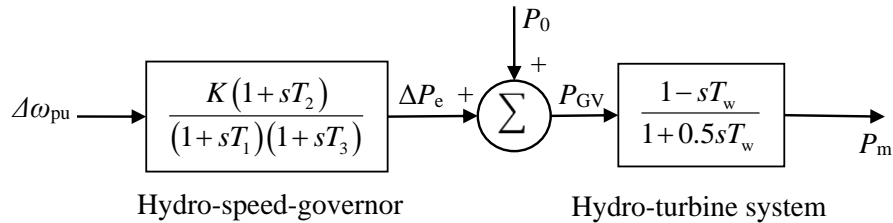


Figure 3.8 Simplified model for speed-governor and hydro-turbine system [36], [41]

The states of the hydro turbine speed-governor and turbine system are defined in Figure 3.8 as follows:

$$\begin{aligned}
\frac{dx_1}{dt} &= \frac{1}{T_1} \left[-x_2 + \frac{K(T_1 - T_2)}{(T_1 - T_3)} \Delta\omega_{pu} \right] \\
\frac{dx_2}{dt} &= \frac{1}{T_3} \left[-x_2 + \frac{K(T_3 - T_2)}{(T_3 - T_1)} \Delta\omega_{pu} \right] \\
P_{GV} &= P_{T0} - \Delta P_e \quad \text{for } P_{\min} \leq P_{GV} \leq P_{\max} \\
\frac{dP_m}{dt} &= \frac{2}{T_w} \left[-P_m + G_{pu} - T_w \frac{dG_{pu}}{dt} \right] \\
\Delta P_e &= x_1 + x_2
\end{aligned} \tag{3.21}$$

Where x_1 and x_2 are the first and second integral intermediate states in pu; K is the hydro turbine proportional gain in pu; P_m is the turbine mechanical power state in pu; ΔP_e is the speed-governor regulated power in pu; P_{T0} is the steady-state value of the P_m input in pu; P_{GV} is the speed-governor input to turbine in pu; T_w is the water starting time or water time constant in sec; T_1, T_2, T_3 are the speed-governor time constants in sec; G_{pu} is the gate valve position between 0 and 1, when the turbine is in full load, $G_{pu} = 1$. All the regulator gains and time constants are defined in [41].

3.4 Grid interfacing

Synchronous generators are modelled in their respective machine reference frames and all the state and auxiliary variables of rotor and stator are represented in their machine-frame of reference (dq-axes). On the other hand, the grid is represented in a ‘synchronous-frame’ of reference ($\alpha\beta$ -axes). A quantity of F (voltage or current) is related mathematically in dq-axes and $\alpha\beta$ -axes as shown in Figure 3.9 [41], [48]. The $\alpha\beta$ -frame for synchronous generators is the resultant or single-phase representation of the three-phase quantities at the generator terminal in the network reference frame. As can be proved later in subsection 5.5.1, the steady-state generator internal voltage lies along the q-axis so that the initial internal voltage angle δ is defined as the angle between the α -axis and the q-axis [42]. Hence, the axis transformation angle between the dq- and $\alpha\beta$ -frames is $\delta - \pi/2$.

Hence, an F quantity in $\alpha\beta$ -frames is transformed to dq-frame using (3.22) and the other way round by inverting the matrix.

$$\begin{bmatrix} F_d \\ F_q \end{bmatrix} = \begin{bmatrix} \sin \delta & -\cos \delta \\ \cos \delta & \sin \delta \end{bmatrix} \begin{bmatrix} F_\alpha \\ F_\beta \end{bmatrix} \tag{3.22}$$

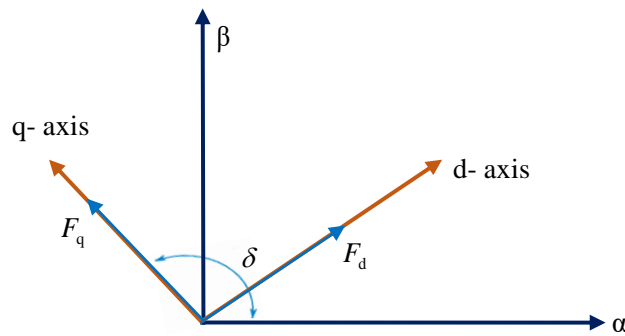


Figure 3.9 Phase diagram of generator dq-frame and synchronous axis $\alpha\beta$ -frame [41], [48]

The synchronous generators are modeled as source-currents, whose internal transient voltages, in (3.9), are transformed to current sources as shown in Figure 3.10. By principle, a generator modeled with source-current has the capability to maintain a constant current flow across its terminal regardless of the voltage profile at the generator bus. [41].

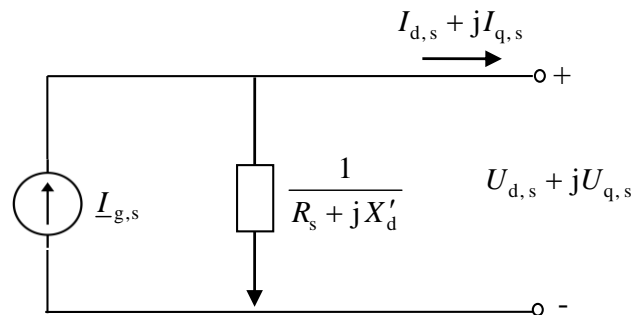


Figure 3.10 Synchronous generator as source-current in the dq-frame [41]

The generator currents in the synchronous reference frame are represented by the generator source current $\underline{I}_{g,s}$ and the grid impedance as in Figure 3.10. This describes the grid interfacing model with generator convention which helps to determine the injected current from the generator as a function of the internal transient voltages. As described in section 3.3.1.3, the dynamic saliency is not neglected for the 4th-order model so that the model can host transient values with $X'_d \neq X'_q$. Thus, using the voltage source equivalent circuit in Figure 3.4, the generator source current in the $\alpha\beta$ -frame is given as in (3.22).

$$\underline{I}_{g,s} = -\frac{U'_d + U_{d,c} + jU'_q}{R_s + jX'_d} (\sin \delta - j\cos \delta) \quad (3.23)$$

Where $\underline{I}_{g,s} = I_{\alpha,s} + j I_{\beta,s}$ represents the $\alpha\beta$ -frame source current of a single generator. In every time step, the generator terminal voltage $\underline{u}_{dq,s}$ is determined from the network model, as shown in Figure 3.11, using (3.24).

$$\underline{u}_K = \underline{Y}_{KK,LG}^{-1} \underline{i}_{g,s} \quad (3.24)$$

Where, \underline{u}_K is the updated vector of all network bus voltages, $\underline{i}_{g,s}$ is the vector of generator source currents in $\alpha\beta$ -frame and $\underline{Y}_{KK,LG}$ is the network admittance matrix including the load and generator admittances as shown in Figure 3.11. Then the generator terminal voltages $\underline{u}_{dq,s}$ are obtained from (3.24) by transforming the $\alpha\beta$ -frame to dq-axes frame using (3.22). Using the new terminal voltage of a generator $\underline{U}_{dq,s}$ and its internal transient voltage \underline{U}'_{dq} , each generator current is updated and will be used as input for the next time simulation through numerical integration with:

$$\underline{I}_{dq,s} = I_{d,s} + j I_{q,s} = \frac{U'_d + U_{dc} + j U'_q - (U_{d,s} + j U_{q,s})}{R_s + j X'_d} \quad (3.25)$$

Where, $\underline{I}_{dq,s}$ is the generator stator current in dq-frame. It is determined as a function of the internal transient generator voltages (U'_d , U_{dc} and U'_q), rotor angle δ and the terminal voltage $\underline{U}_{dq,s}$ in dq-frame (after the network solution).

Electric power change on the supply or demand side can have a major effect on the system frequency which is the average network bus frequency that the majority of the synchronous generators are following. Calculating the momentarily grid frequency is an important task if the generating units are not set sufficiently to automatically respond in line to the changing grid frequency. In this thesis work, the grid frequency f_{COI} that the synchronous generators are following is calculated based on the center of inertia as in [11].

$$f_{COI} = \frac{\sum_{i=1}^{n_g} (\omega_i H_{g,i})}{\sum_{i=1}^{n_g} H_{g,i}} \quad (3.26)$$

Where, $i = 1, 2, \dots, n_g$ is the number of generators participating in frequency regulation. n_g is the total number of generators; $H_{g,i}$ is the i -th generator inertia constant in seconds and ω_i is the i -th generator rotor speed in rad/sec.

The network and synchronous generator dynamic models discussed in this chapter and the wind turbine generator dynamics presented in the next chapter will represent the complete AC power network transient analysis. The complete schematic diagram that describes the grid integration model of synchronous generators along with the voltage and frequency regulation modules is presented in Figure 3.11.

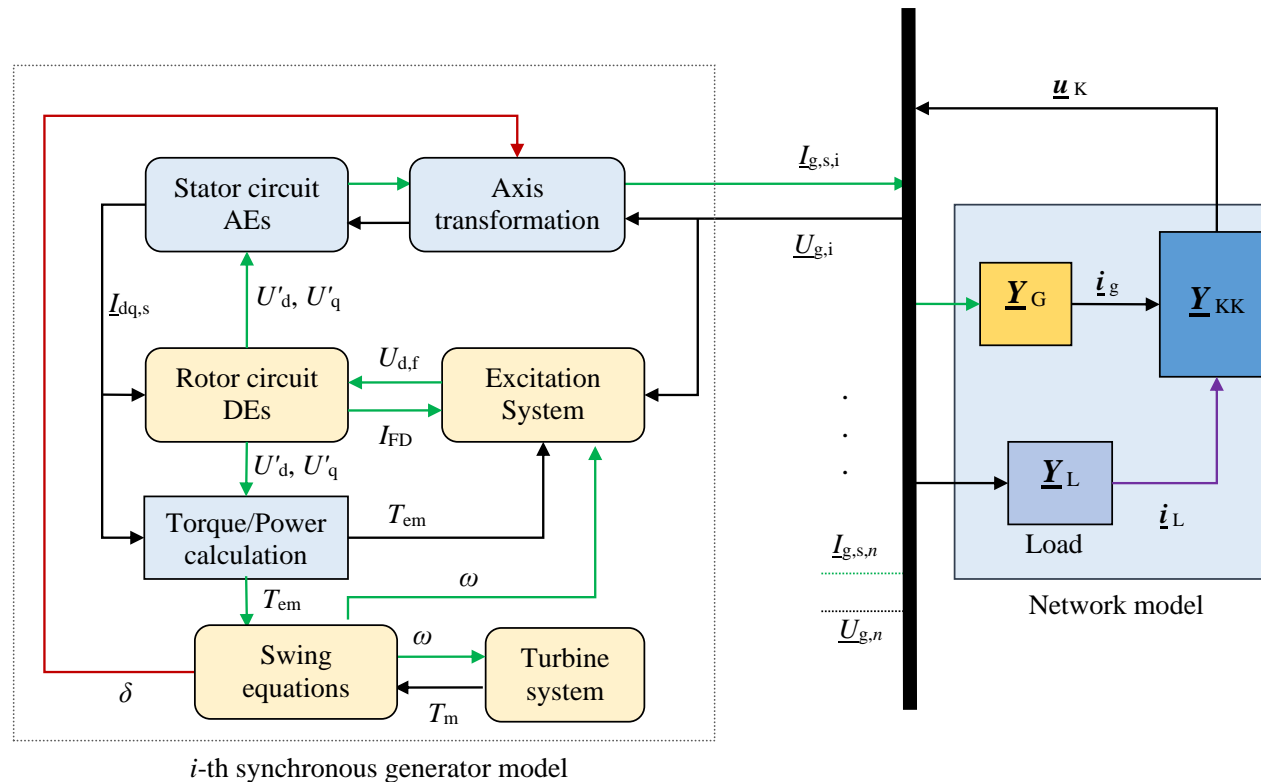


Figure 3.11 Synchronous generator grid integration layout for time simulation [36]

4 DFIG-based Wind Turbine Dynamic Model

4.1 Generic dynamic wind turbine models

Power generation from wind turbine is a relatively new scheme of electric generation with exceptional features, for instance wind turbines are receiving irregular wind speeds and nowadays they use power electronic converters to regulate their outputs. Unlike the conventional power plants, there are few generic models for grid integrated wind turbines intended for transient stability studies. The positive-sequence dynamic models of wind power plant (WPP) are typically used for simulation of bulk power systems. Such models are required for validating the compliance with network reliability criteria and for power system planning expansions. Previously, most dynamic models of wind turbine generators were vendor-specific and have been developed mainly for validating the specific dynamic characteristics of user-defined models [49], [50].

Due to the stochastic nature of wind and technological complexity of the wind turbine components, with plenty of vendor-specific turbine generators, there are still many challenges to use generic wind turbine models like the synchronous generators for stability analyses of large networks [49]. The Western Electric Coordinating Council (WECC) renewable energy modeling task force and the IEEE working group on dynamic performance of wind power generation have jointly developed a set of generic wind turbine models in 2014, which are used in Siemens PTI PSS[®]E and GE PSLF[®] [40]. The energy system international group (ESIG) has sustained interesting thoughts and notable results have also been obtained related to dynamic wind turbine models as in [39]. A collaborative research group between IEC and WECC has resulted in series editions of generic models which are being used by different wind turbine manufacturers and grid operators [39]. However, most of these models are still vendor specific and they are commercial tools specifically to study the dynamics of wind generators not the whole grid system.

Based on the available WTGs in the market, ESIG group has developed four generic wind turbine topologies for the respective type of wind turbines as stated in section 2.3.2. As described in section 2.4, Type 3 WTs (DFIGs) are the most preferable technologies due to their cost and grid integration compatibilities. Therefore, this research focuses on DFIG based power generation and studying the detailed dynamic behaviors and impacts of such machines on the transient stability of power grid. The RMS model of DFIG-based wind turbines is applied to study the dynamic impacts of wind generators on various grid systems in the proceeding sections. The associated control strategies are also presented and

verified via comparative simulations with the available EMT-models in the Simulink library. The models of the wind turbine generator and control strategies are premeditated to present the dynamic behaviors of the machine along with the power system dynamics to check if the system remains stable in response to different types of disturbances.

The main components of a typical WTG are shown in Figure 4.1. The dynamic equations, that include the differential and algebraic equations relating to the mathematical models of wind turbine subsystem are described in the following subsections.

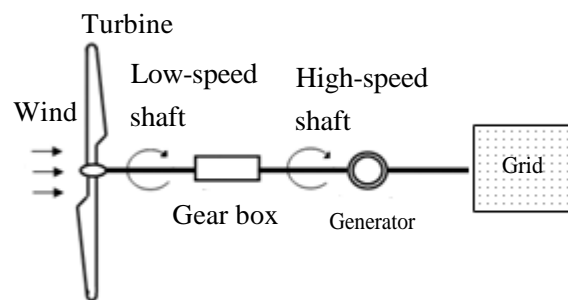


Figure 4.1 Schematic diagram of a typical WTG [49]

Modeling of wind turbines is complex due to the non-linear electromechanical behaviors which incorporate a large number of control subsystems. Wind turbines can be considered as assembly of subsystems which can be uniquely modeled or as a group of turbines with similar design and environment characteristics. The individual subsystems can then be assembled into a wind turbine generator model. Based on a DFIG modeling standpoint, a wind turbine consists of the following main mechanical and electrical subsystems:

- Rotor blades/ the aerodynamic model of turbines;
- Mechanical models for the drive trains;
- Induction generator model;
- Back-to-Back converter model;
- Rotor-side converter control model;
- Grid-side converter control model;
- Pitch controller model and
- The step-up transformer and grid-interfacing model.

The interaction of these subsystems determines the steady-state and dynamic response of the wind turbine generator. Modeling of the rotor blades, drive-train, induction generator and control systems are based on the differential and algebraic equations that describe the respective steady-state and dynamic operations. The active and reactive power references

of the control strategy are determined based on the optimal rotor speed and the desired reactive power demand at the grid-side, respectively.

4.2 Wind speed model

Uniform wind speeds are considered for similar turbines that are receiving the same wind regime in a wind park. Wind gusts are involved in the test model which represent mathematically the random sequential wind function around the average value [51].

$$v_g(t) = \frac{2 v_{g,\max}}{1 + e^{-4(\sin(\omega_g t) - 1)}} \quad (4.1)$$

Where ω_g gust frequency given by $2\pi/T_g$
 v_g maximum possible gust wind speed of the site
 T_g duration of gust wind speed in seconds

The wind gust amplitude fluctuates up to 10 m/s and the gust period is between 10-50 seconds. Then, the resulting wind velocity, $v(t)$ including the gust wind is given by,

$$v(t) = v_0 + v_g(t) \quad (4.2)$$

Where v_0 is the constant average speed in m/s

4.3 Wind turbine model

The kinetic energy contained in a flowing wind is converted to useful mechanical energy by rotor-blades of the turbine. This energy conversion mechanism is represented by the wind turbine model and expressed as in [26].

$$P_T = \frac{1}{2} \rho \pi R^2 C_p(\lambda, \beta) v^3 \quad (4.3)$$

$$\lambda = \frac{\Omega_t R}{v} \quad (4.4)$$

Where P_T is the aerodynamic/turbine power, $C_p(\lambda, \beta)$ is the wind energy conversion coefficient given by (4.5), v is the wind speed in m/s, ρ is the air density in kg/m^3 , R is the rotor blade radius in m, Ω_t is the low-speed shaft turbine speed in rad/sec, λ is the tip speed ratio and β is the pitch angle in degree. The power coefficient of the wind turbine conversion is given by the non-linear relationship in (4.5).

$$C_p(\lambda, \beta) = \left(\frac{C_1}{\lambda_i} - C_2 \beta - C_3 \right) e^{\frac{-C_4}{\lambda_i}} + C_5 \lambda$$

$$\frac{1}{\lambda_i} = \frac{1}{\lambda + 0.08\beta} - \frac{0.035}{1 + \beta^3}$$
(4.5)

The non-linear C_p curve as a function of tip speed ratio λ and pitch angle β is fitted to a wind turbine power curve by using the *gaussfit* toolbox and then optimized by applying *fminsearch* function in MATLAB. The numerical approximated optimal coefficients of the aerodynamic model for the wind turbines used in this work, are determined as in [25]:

$$C_1 = 60.088; C_2 = 0.2072; C_3 = 2.59; C_4 = 21; C_5 = 0.0068$$

The wind turbine power coefficient $C_p(\lambda, \beta)$ is a non-linear exponential function applied to relate the two variables. The correlation is determined using numerical approximation techniques that fits to manufacturer's power curve data. The power coefficient is a variable parameter that depends on the rotor blade tip speed ratio as in (4.5) and pitch angle which in turn depends on the generator rotor speed and the incoming wind speed. The power coefficient is controlled to its optimal value, i.e., the turbine output power is along the maximum power point tracking (MPPT) for wind speeds below the nominal value while the pitch control again reduces the power coefficient to a value that corresponds to the rated power of a generator when the incoming speed is above the nominal wind speed.

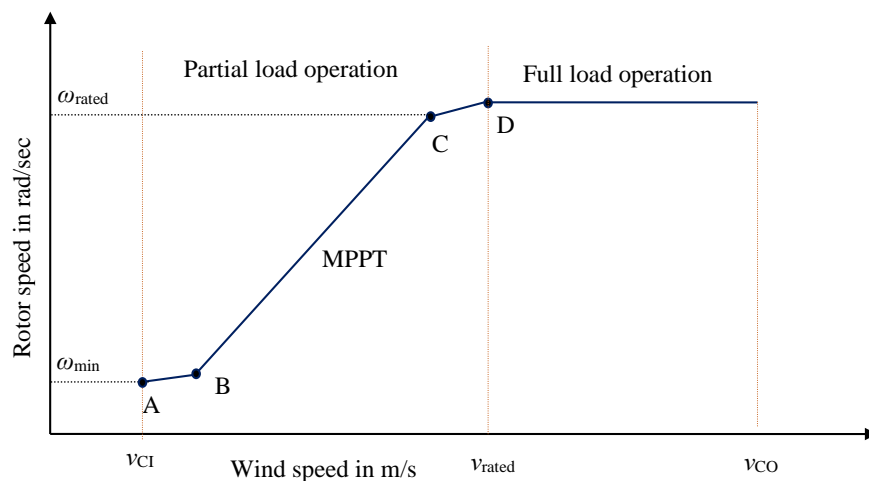


Figure 4.2 Wind turbine control strategy based on four speed control regions [52]

The wind turbine control system has different control strategies to regulate the output wind power depending on the wind speed that ranges between cut-in (v_{CI}) and cut-out (v_{CO}) values. The target of the turbine control system in the region between points B and

C is to optimize the value of $C_p(\lambda, \beta)$ so that the optimal power is tracked. In this regard, the rotor blade tip speed ratio is kept near its optimal value λ_{opt} in (4.4).

The conventional wind turbine control system is required to uphold the optimal energy capture. With such control strategies, the wind turbine energy conversion efficiency is optimal and helps the wind turbine to operate for a wide range of wind velocities. The turbine output power increases by cubic of the rotor speed (high speed shaft), Ω_m^3 with increasing wind speed for the partial load operation and remains near the nominal value during the full load operation in Figure 4.2. The corresponding turbine torque increases by Ω_m^2 . Thus, the optimal power and torque characteristic of a turbine model are described as in [25]:

$$P_T = \frac{1}{2} \rho \pi R^2 C_{p,opt} \left(\frac{\Omega_t R}{\lambda_{opt}} \right)^3 = \frac{1}{2} \rho \pi R^5 \frac{C_{p,opt}}{\lambda_{opt}^3} \Omega_t^3 \quad (4.6)$$

$$T_w = \frac{P_T}{\Omega_t} = \frac{1}{2} \rho \pi R^5 \frac{C_{p,opt}}{\lambda_{opt}^3} \Omega_t^2$$

With a gearbox ratio of N , the high-speed shaft Ω_m is equal to $N\Omega_t$ and its torque T_m is equal to T_w/N . Then the corresponding high-speed power P_m and torque T_m are given by

$$P_m = \frac{1}{2} \rho \pi R^5 \frac{C_{p,opt}}{\lambda_{opt}^3} \left(\frac{\Omega_m}{N} \right)^3 = K_{opt} \Omega_m^3$$

$$T_m = \frac{1}{2} \rho \pi R^5 \frac{C_{p,opt}}{N \lambda_{opt}^3} \left(\frac{\Omega_m}{N} \right)^2 = K_{opt} \Omega_m^2 \quad (4.7)$$

$$\text{Where } K_{opt} = \frac{1}{2} \rho \pi R^5 \frac{C_{p,opt}}{N^3 \lambda_{opt}^3}$$

The performance of the rotational speed Ω_m depends on the efficiency of the mechanical coupling between the rotor and generator, which is expressed as the drive-train dynamics.

4.4 Drive-train model

The mechanical coupling (drive-train) includes the wind turbine, gear-box, shafts and other coupling components of the wind turbine. The wind turbine drive train is usually modeled by a two-mass system as in [53]. The generator's high-speed shaft is coupled to the turbine shaft via gearbox as in Figure 4.3.

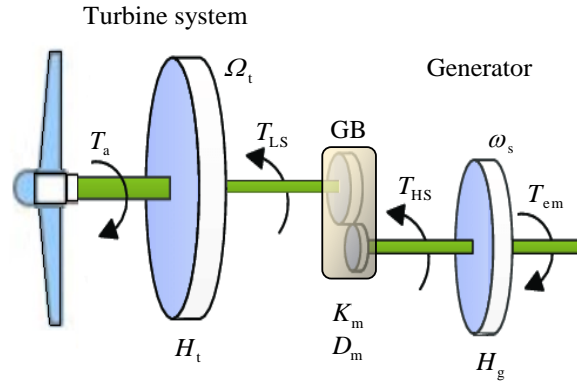


Figure 4.3 Two-mass wind turbine shaft system [53]

Where T_a , T_{LS} , T_{HS} and T_{em} are the aerodynamic, low-speed shaft, high-speed shaft and electromagnetic torques, respectively; H_t and H_g are the turbine and generator mass systems, respectively; K_m and D_m are the shaft stiffness and damper coefficients of the two-mass system, respectively. The high-speed shaft and the low-speed shaft of the two-mass system are related in (4.8).

$$\omega = p \Omega_m = N \omega_t = N p \Omega_t \quad (4.8)$$

Where;

- Ω_t turbine mechanical angle speed (low-speed shaft) in mech. rad/sec
- Ω_m generator mechanical angle (high-speed shaft) in mech. rad/sec
- ω_t turbine rotor angle speed in elec. rad/sec
- ω generator angle speed in elec. rad/sec
- ω_s rotational speed of the generator stator fields in elec. rad/sec
- N gearbox ratio

The one-mass model of the drive train is also applicable for transient stability studies as given in [54]:

$$\frac{d\omega}{dt} = \frac{1}{T_d} (T_m - T_{em}) \quad (4.9)$$

- Where $T_d = 2H$ mechanical transmission time constant in seconds
- H lumped sum inertia constant of WTG in seconds
- T_m mechanical torque of wind generator end axis in per unit
- T_{em} electromagnetic torque of generator in per unit

4.5 Induction generator model

The stator windings of a DFIG-based wind turbine are coupled directly to the grid and the rotor is coupled via a power electronic converter. In **Figure 4.4**, the DFIG configuration shows that the stator is getting supplied by three-phase voltages at constant frequency from the grid. The stator three-phases windings have p pairs of poles and are directly connected to the grid. The currents in the stator windings create rotating magnetic fields in the air gap. These induced stator fields have a rotational speed of ω_s , which is proportional to the grid frequency f_s as in (4.10)

$$\omega_s = 2\pi f_s \quad (4.10)$$

The stator windings are usually connected to the grid through a step-up (unit) transformer. On the other hand, the three-phase rotor windings are supplied by a voltage source via slip rings and brushes but independent from the stator voltages. The power supply of the rotor comes from the rotor-side converter [25], [53]. Therefore, the rotor windings are connected to the grid through a back-to-back converter. If the generator's rotor rotates at a speed different from that of the stator field, variation in magnetic flux is created. By Faraday's law of induction, currents are induced in the rotor windings. This leads to a slip of rotor speed s that rotates at super- or sub-synchronous rotational fields.

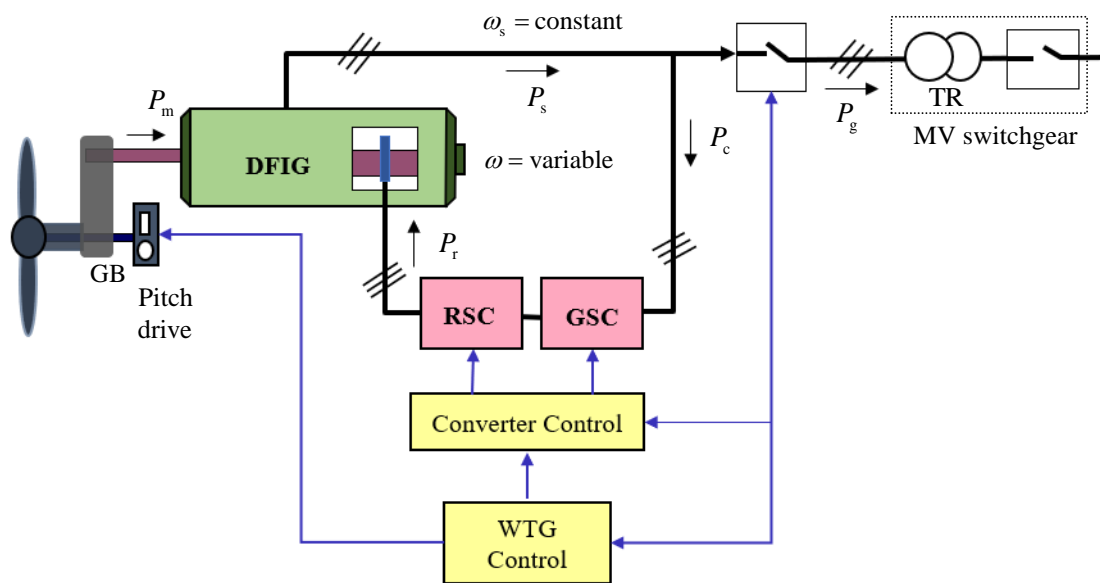


Figure 4.4 Schematic diagram of doubly-fed induction generator and converter

The slip of an induction generator is defined as a variation of the stator rotational field ω_s and rotor mechanical speed ω as stated in (4.11).

$$s = \frac{\omega_s - \omega}{\omega_s} \quad (4.11)$$

Where; ω is the generator rotor angle speed in elec. rad/sec; ω_s is the synchronous speed in elec. rad/s and s is the rotor slip ratio.

4.5.1 Steady-state operation

As described in the drive-train section, the DFIG components operate at different frequencies which are related to each other as in equation (4.12).

$$\omega_r = \omega_s - \omega \quad (4.12)$$

Where;

- ω_s frequency of stator fields (voltages and currents) in elec. rad/sec,
- ω_r frequency of rotor fields (voltages and currents) in elec. rad/sec and
- ω variable rotor speed in elec. rad/sec

As the stator windings of the DFIG are directly connected to the grid, ω_s is constant and equals the synchronous frequency of the network reference frame. However, the frequency of the electrical quantities in the rotor windings ω_r depends on the rotor speed ω , which results in three operating conditions [25]:

$$\begin{aligned} \omega < \omega_s &\Rightarrow s > 0 \rightarrow \text{Sub-synchronous operation} \\ \omega = \omega_s &\Rightarrow s = 0 \rightarrow \text{Synchronous operation} \\ \omega > \omega_s &\Rightarrow s < 0 \rightarrow \text{Super-synchronous operation} \end{aligned} \quad (4.13)$$

The variable rotor speed characteristics of the DFIG-based wind turbines depend on both the available wind speed from the turbine side and the load power (reference active power) by which the partial-load converter either supplies power to the grid or receives power from the grid. Thus, the net generator output power P_g is the sum of the stator and the rotor power which goes via the grid-side converter P_c .

$$P_g = P_s + P_c \quad (4.14)$$

In the transient analyses, the network is represented by a single-phase system and similarly the DFIG stator and rotor are represented by an ideal model with symmetry in the machine (RMS type). The other two phases are considered as balanced system, each at 120° phase shift and a linear magnetization. The stator and rotor windings turn per phase, N_s and N_r respectively, are related by coefficient μ that relate the induced stator and rotor electromagnetics as:

$$\mu = \frac{N_s}{N_r} \Rightarrow U_{rs} = s \frac{U_s}{\mu} \quad (4.15)$$

Where, \underline{U}_{rs} is the rotor induced voltage referred to the stator and \underline{U}_s is the terminal voltage as shown in Figure 4.5. The leakage reactance of the stator and rotor are calculated from the inductances according to the frequency of the stator and rotor fields.

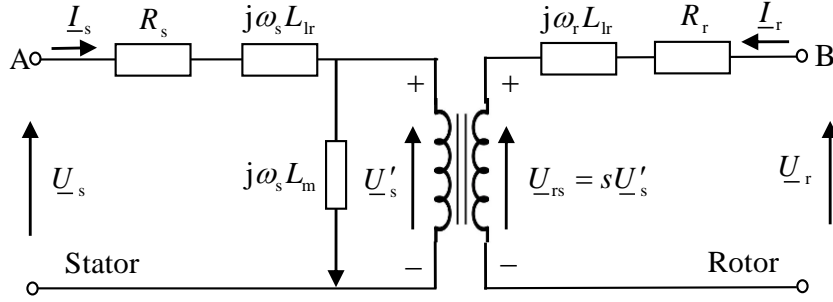


Figure 4.5 Equivalent circuit of DFIG with rotor parameters referred to the stator [25]

In Figure 4.5, the steady-state voltage and flux parameters of the rotor are referred to the stator and the coefficient μ is assumed as unity. By applying the Faraday's voltage law, the steady-state voltage and flux equations are depicted in (4.16) and (4.17), respectively.

$$\begin{aligned} \underline{U}_s &= R_s \underline{I}_s + j\omega_s L_{ls} \underline{I}_s + j\omega_s L_m (\underline{I}_s + \underline{I}_r) = R_s \underline{I}_s + j\omega_s L_s \underline{I}_s + j\omega_s L_m \underline{I}_r \\ \underline{U}_r - s\underline{U}'_s &= (R_r + j s \omega_s L_{lr}) \underline{I}_r \Rightarrow \frac{\underline{U}_r}{s} - \underline{U}'_s = \left(\frac{R_s}{s} + j s \omega_s L_{lr} \right) \underline{I}_r \end{aligned} \quad (4.16)$$

$$\Rightarrow \frac{\underline{U}_r}{s} = \frac{R_s}{s} \underline{I}_r + j \omega_s L_r \underline{I}_r + j \omega_s L_m \underline{I}_s$$

$$\begin{aligned} \underline{\Psi}_s &= L_m (\underline{I}_s + \underline{I}_r) + L_{ls} \underline{I}_s = L_s \underline{I}_s + L_m \underline{I}_r \\ \underline{\Psi}_r &= L_m (\underline{I}_s + \underline{I}_r) + L_{lr} \underline{I}_r = L_m \underline{I}_s + L_r \underline{I}_r \end{aligned} \quad (4.17)$$

Where \underline{U}_s and \underline{U}_r are supplied voltages to the stator and rotor, referred to the stator, respectively; \underline{U}'_s is the internal voltage of the stator; L_{ls} and L_{lr} are leakage reactances for stator and rotor referred to stator, respectively; L_m is mutual inductance; $L_s = L_{ls} + L_m$ is the stator inductance and $L_r = L_{lr} + L_m$ is the rotor inductance; s is the slip of the induction machine.

The active power balance of a DFIG using the generator convention is expressed as in (4.18).

$$P_m = P_s + P_r - P_{cu,s} - P_{cu,r} \quad (4.18)$$

Where P_m is the mechanical turbine power, P_s is the stator active power and P_r is the rotor active power, $P_{cu,s}$ is the copper losses in the stator windings and $P_{cu,r}$ is the copper losses in the rotor windings. The stator and rotor power generations as well as copper losses in (4.18) are defined as:

$$\left. \begin{aligned} P_s &= 3 \operatorname{Re}\{\underline{U}_s \underline{I}_s^*\} = 3R_s I_s^2 + 3\omega_s L_m \operatorname{Im}\{\underline{I}_s \underline{I}_r^*\} \\ P_r &= 3 \operatorname{Re}\{\underline{U}_r \underline{I}_r^*\} = 3R_r I_r^2 - 3s \omega_s L_m \operatorname{Im}\{\underline{I}_s \underline{I}_r^*\} \\ P_{cu,s} &= 3R_s I_s^2 \text{ and } P_{cu,r} = 3R_r I_r^2 \end{aligned} \right\} \Rightarrow P_m = 3p\Omega_m L_m \operatorname{Im}\{\underline{I}_s \underline{I}_r^*\} \quad (4.19)$$

The values of P_s and P_r are interpreted as powers delivered to the machine, the value of P_m is defined as the mechanical power developed by the machine via the generator shaft. The mechanical high-speed shaft speed $\Omega_m = \omega/p$ as explained in (4.8). where ω is the rotor speed in electrical rad/sec and p is the number of pole pairs. Thus, the steady-state electromagnetic torque T_{em} developed in the shaft is defined as follows:

$$T_{em} = \frac{P}{\omega} P_m = 3pL_m \operatorname{Im}\{\underline{I}_s \underline{I}_r^*\} \quad (4.20)$$

4.5.2 Dynamic model of DFIG

As in [25], the DFIG can be modelled in space vector representation with three different reference frames, typically the stator stationary-frame of reference ($\alpha\beta$ -axes), the rotor reference frame (DQ-axes) which rotates at ω and the synchronously rotating frame (dq-axes) which rotates at ω_s . These three possible frames of references are shown in Figure 4.6. For studying the power system transients along with the synchronous generators, the DFIG is modelled in the dq-frame of reference to which all the stationary stator and rotating rotor quantities can be transformed or vice versa. Unlike in the synchronous generator, the induction generator can normally operate at a rotor speed which is higher or lower than the synchronous speed which is explained by the slip operation. Thus, the DFIG operates at three distinct speeds that are the stator field speed, mechanical rotor speed and the slip speed that correspond to the rotor fields. When one or two of these speeds vary unexpectedly or strategically from controllers the other speeds vary in such a way that the sum of the three speeds equals to zero.

$$\begin{aligned}\underline{\psi}_s^s &= L_s \underline{I}_s^s + L_m \underline{I}_r^s \\ \underline{\psi}_r^r &= L_r \underline{I}_r^r + L_m \underline{I}_s^r\end{aligned}\quad (4.22)$$

Where; the superscripts s and r represent the stator fields in the stationary frame of reference ($\alpha\beta$ -axes) and the rotor fields in the rotor frame of reference (DQ-axes). The stator and rotor voltage equations of a-phase axis are similarly expressed as the sum of the voltage drop in the windings and the induced voltage in the windings [25].

$$\begin{aligned}\underline{U}_s^s &= R_s \underline{I}_s^s + \frac{d\underline{\psi}_s^s}{dt} \\ \underline{U}_r^r &= R_r \underline{I}_r^r + \frac{d\underline{\psi}_r^r}{dt}\end{aligned}\quad (4.23)$$

\underline{U}_s and \underline{U}_r are the phase voltage of stator and rotor windings, respectively; \underline{I}_s and \underline{I}_r are the phase currents of stator and rotor windings, respectively; $\underline{\psi}_s$ and $\underline{\psi}_r$ are the phase fluxes of stator and rotor windings, respectively. All the stator and rotor quantities are presented in their respective reference frames, the $\alpha\beta$ -axes and DQ-axes, respectively.

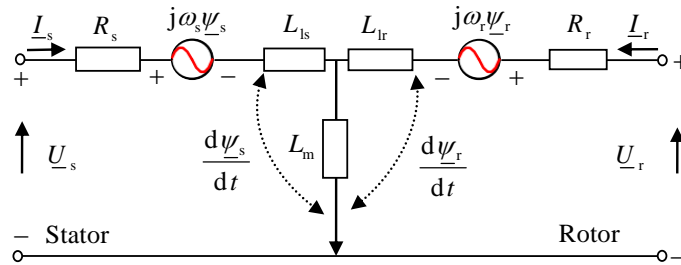


Figure 4.7 RMS equivalent dynamic circuit of the DFIG in network reference frames [52]

Based on the axis transformation in Figure 4.6, the stator and rotor frames of references in (4.22) and (4.23) are multiplied by $e^{-j\theta_s}$ and $e^{-j\theta_m}$, respectively to transform the variables to a grid system reference frame ($\alpha\beta$ -axes). The stator and rotor flux expressions in the static reference frame (a-phase axis, i.e., $\alpha\beta$ -frame) are expressed as:

$$\begin{aligned}\underline{\psi}_s^s e^{-j\theta_s} &= L_s \underline{I}_s^s e^{-j\theta_s} + L_m \underline{I}_r^s e^{-j\theta_s} \\ \underline{\psi}_r^r e^{-j\theta_m} &= L_r \underline{I}_r^r e^{-j\theta_m} + L_m \underline{I}_s^r e^{-j\theta_m}\end{aligned}\quad \Rightarrow \quad \begin{cases} \underline{\psi}_{\alpha\beta,s} = L_s \underline{I}_{\alpha\beta,s} + L_m \underline{I}_{\alpha\beta,r} \\ \underline{\psi}_{\alpha\beta,r} = L_r \underline{I}_{\alpha\beta,r} + L_m \underline{I}_{\alpha\beta,s} \end{cases}\quad (4.24)$$

In a similar way, the stator and rotor voltage equations in the grid reference frame ($\alpha\beta$ -axes) are described as in (4.25).

$$\left. \begin{aligned} \underline{U}_s^s e^{-j\theta_s} &= R_s \underline{I}_s^s e^{-j\theta_s} + \frac{d\underline{\psi}_s^s}{dt} e^{-j\theta_s} \\ \underline{U}_r^r e^{-j\theta_m} &= R_r \underline{I}_r^r e^{-j\theta_m} + \frac{d\underline{\psi}_r^r}{dt} e^{-j\theta_m} \end{aligned} \right\} \Rightarrow \begin{cases} \underline{U}_{\alpha\beta,s} = R_s \underline{I}_{\alpha\beta,s} + j\omega_s \underline{\psi}_{\alpha\beta,s} + \frac{d\underline{\psi}_{\alpha\beta,s}}{dt} \\ \underline{U}_{\alpha\beta,r} = R_r \underline{I}_{\alpha\beta,r} + j\omega_r \underline{\psi}_{\alpha\beta,r} + \frac{d\underline{\psi}_{\alpha\beta,r}}{dt} \end{cases} \quad (4.25)$$

The electromotive torque produced by the induction machine at the stator air-gap is calculated as in [25]:

$$T_{em} = \frac{3}{2} p \operatorname{Im}\{\underline{\psi}_{\alpha\beta,r} \underline{I}_{\alpha\beta,r}^*\} = \frac{3}{2} \frac{L_m}{\sigma L_r L_s} p \operatorname{Im}\{\underline{\psi}_{\alpha\beta,r}^* \underline{\psi}_{\alpha\beta,s}\} \quad (4.26)$$

Where, the fluxes and currents are in RMS values; p is the number of pole pairs of the machine; $\sigma = 1 - \frac{L_m^2}{L_r L_s}$ is the leakage reactance;

The other most applicable option is to transform all the rotor and stator quantities from their respective frames, the rotor frame (DQ-axes) and the grid reference frame ($\alpha\beta$ -axes) respectively, to a common frame which rotates at synchronous rate (the dq-axes). Therefore, from this point, all the electrical quantities of the stator and rotor including the converter control variables are transformed and realized in the dq-frame of reference.

4.5.2.2 dq-axes model

In the dq-frame of reference, the dynamic model of the induction generator is depicted by the conventional T-equivalent circuit model in Figure 4.7. This model consists of a stator winding and a rotor winding with slip rings. Therefore, the dq-axes electrical dynamic equations are derived from the equivalent circuit presented in Fig. 4.7 and/or transforming the respective equations in (4.22) and (4.23), respectively to the synchronous dq-axes. Therefore, the stator and rotor frames of references in (4.22) and (4.23) are multiplied by $e^{-j\theta_s}$ and $e^{-j\theta_r}$, respectively to transform the variables to a common synchronous reference frame (dq-axes). The stator and rotor flux equations are then expressed in the dq-axes as [25]:

$$\begin{aligned} \underline{\psi}_{dq,s} &= L_s \underline{I}_{dq,s} + L_m \underline{I}_{dq,r} \\ \underline{\psi}_{dq,r} &= L_m \underline{I}_{dq,s} + L_r \underline{I}_{dq,r} \end{aligned} \quad (4.27)$$

Similarly, the stator and rotor voltage equations in dq-axes:

$$\begin{aligned}\underline{U}_{dq,s} &= R_s \underline{I}_{dq,s} + \frac{d\underline{\psi}_{dq,s}}{dt} + j\omega_s \underline{\psi}_{dq,s} \\ \underline{U}_{dq,r} &= R_r \underline{I}_{dq,r} + \frac{d\underline{\psi}_{dq,r}}{dt} + j\omega_r \underline{\psi}_{dq,r}\end{aligned}\quad (4.28)$$

Where, the dq-frame components are described as:

$$\begin{aligned}\underline{U}_{dq,s} &= U_{d,s} + jU_{q,s} \text{ is stator voltage in V} & \underline{U}_{dq,r} &= U_{d,r} + jU_{q,r} \text{ is rotor voltage in V} \\ \underline{I}_{dq,s} &= I_{d,s} + jI_{q,s} \text{ is stator current in A} & \underline{I}_{dq,r} &= I_{d,r} + jI_{q,r} \text{ is rotor current in A} \\ \underline{\psi}_{dq,s} &= \psi_{d,s} + j\psi_{q,s} \text{ is stator flux in Weber} & \underline{\psi}_{dq,r} &= \psi_{d,r} + j\psi_{q,r} \text{ is rotor flux in Weber} \\ \omega_s \underline{\psi}_{dq,s} & \text{ is stator back electromagnetic in V} & \omega_r \underline{\psi}_{dq,r} & \text{ is rotor back electromagnetic in V} \\ \omega & \text{ is rotor frequency rad/sec} & \omega_r &= \omega_s - \omega \text{ is slip frequency in rad/sec}\end{aligned}$$

4.5.2.3 The per unit system model

In a similar fashion to the synchronous generator models, the dynamic models in (4.27) and (4.28) are transformed to a common aggregated wind generator base power and stator voltage. The base quantities for the stator of a DFIG generator, with p as pole pairs, are defined in (4.29).

$$\begin{aligned}S_b &= S_{\text{nom}} \\ U_b &= U_s\end{aligned}\quad (4.29)$$

Where, S_b is the three-phase base power which is equal to a nominal value of an aggregated wind park in MVA and U_b is the stator line to neutral voltage (RMS value) of the WTG in V. The other generator base quantities are derived as in (4.30) [11] pp. 317.

$$\begin{aligned}I_b &= \frac{S_b}{3U_b}; \quad \Psi_b = \frac{U_b}{\omega_b}; \quad Z_b = \frac{U_b}{I_b}; \quad L_b = \frac{\Psi_b}{I_b} \\ \Omega_{m,b} &= \frac{\omega_b}{p}; \quad T_b = \frac{S_b}{\Omega_{m,b}} = \frac{S_b}{\omega_b/p}\end{aligned}\quad (4.30)$$

Where, ω_b is the base synchronous speed. The equivalent per unit stator and rotor flux expressions of (4.27) using (4.29) and (4.30) are decomposed to dq- components as:

$$\begin{bmatrix} \psi_{d,s} \\ \psi_{q,s} \\ \psi_{d,r} \\ \psi_{q,r} \end{bmatrix} = \begin{bmatrix} L_s & 0 & L_m & 0 \\ 0 & L_s & 0 & L_m \\ L_m & 0 & L_r & 0 \\ 0 & L_m & 0 & L_r \end{bmatrix} \begin{bmatrix} I_{d,s} \\ I_{q,s} \\ I_{d,r} \\ I_{q,r} \end{bmatrix}\quad (4.31)$$

Similarly, the first order stator and rotor transient equations can be decomposed into d-axis and q-axis components as in (4.32):

$$\begin{aligned}
\frac{1}{\omega_b} \frac{d\psi_{d,s}}{dt} &= U_{d,s} - R_s I_{d,s} + \omega \psi_{q,s} \\
\frac{1}{\omega_b} \frac{d\psi_{q,s}}{dt} &= U_{q,s} - R_s I_{q,s} - \omega \psi_{d,s} \\
\frac{1}{\omega_b} \frac{d\psi_{d,r}}{dt} &= U_{d,r} - R_r I_{d,r} + s \psi_{q,r} \\
\frac{1}{\omega_b} \frac{d\psi_{q,r}}{dt} &= U_{q,r} - R_r I_{q,r} - s \psi_{d,r}
\end{aligned} \tag{4.32}$$

Where, $\omega = \omega_s/\omega_b$ is the rotor speed in per unit. The dq- components of stator and rotor currents can be expressed in terms of the stator, mutual and rotor fluxes as [25]

$$\begin{aligned}
I_{d,s} &= \frac{1}{L_{ls}} (\psi_{d,s} - \psi_{d,m}); \quad I_{q,s} = \frac{1}{L_{ls}} (\psi_{q,s} - \psi_{q,m}) \\
I_{d,r} &= \frac{1}{L_{lr}} (\psi_{d,r} - \psi_{d,m}); \quad I_{q,r} = \frac{1}{L_{lr}} (\psi_{q,r} - \psi_{q,m})
\end{aligned} \tag{4.33}$$

The dq-frame mutual fluxes $\psi_{d,m}$ and $\psi_{q,m}$ in (4.33) induced due to the stator and rotor fluxes are defined as in (4.34)

$$\begin{aligned}
\psi_{d,m} &= L_{ad} \left[\frac{\psi_{d,s}}{L_{ls}} + \frac{\psi_{d,r}}{L_{lr}} \right] \\
\psi_{q,m} &= L_{aq} \left[\frac{\psi_{q,s}}{L_{ls}} + \frac{\psi_{q,r}}{L_{lr}} \right] \\
L_{ad} = L_{aq} &= \frac{1}{\frac{1}{L_{ls}} + \frac{1}{L_m} + \frac{1}{L_{lr}}}
\end{aligned} \tag{4.34}$$

Substituting the mutual fluxes expressions in (4.34) into (4.33), the stator and rotor currents can be represented in terms of the state variables (stator and rotor fluxes) as:

$$\begin{bmatrix} I_{d,s} \\ I_{q,s} \\ I_{d,r} \\ I_{q,r} \end{bmatrix} = \begin{bmatrix} L_{ls} - \frac{L_{ad}^2}{L_{ls}} & 0 & \frac{-L_{ad}}{L_{lr}L_{ls}} & 0 \\ 0 & L_{ls} - \frac{L_{aq}^2}{L_{ls}} & 0 & \frac{-L_{aq}}{L_{lr}L_{ls}} \\ \frac{-L_{ad}}{L_{lr}L_{ls}} & 0 & L_{lr} - \frac{L_{ad}^2}{L_{lr}} & 0 \\ 0 & \frac{-L_{aq}}{L_{lr}L_{ls}} & 0 & L_{lr} - \frac{L_{aq}^2}{L_{lr}} \end{bmatrix} \begin{bmatrix} \psi_{d,s} \\ \psi_{q,s} \\ \psi_{d,r} \\ \psi_{q,r} \end{bmatrix} \quad (4.35)$$

The stator and rotor currents, as d- and q- components, expressed as function of flux state variables in (4.35), are important to determine the currents. That is, the dynamic fluxes are solved using numerical integrations and the currents are calculated from algebraic equations in (4.35), which are functions of the flux states, so that the generator current-source are easily determined.

A state space form of the flux dynamics in (4.32) can be derived by substituting the stator and rotor currents in (4.35) as function of the state variables.

$$\frac{d}{dt} \begin{bmatrix} \psi_{d,s} \\ \psi_{q,s} \\ \psi_{d,r} \\ \psi_{q,r} \end{bmatrix} = \mathbf{A} \begin{bmatrix} \psi_{d,s} \\ \psi_{q,s} \\ \psi_{d,r} \\ \psi_{q,r} \end{bmatrix} + \begin{bmatrix} U_{d,s} \\ U_{q,s} \\ U_{d,r} \\ U_{q,r} \end{bmatrix} \quad (4.36)$$

Therefore, from equation (4.36), the state space model can be realized as:

$$\dot{\mathbf{x}} = \mathbf{A} \mathbf{x} + \mathbf{u} \quad (4.37)$$

Where, \mathbf{x} is the vector of state variables (fluxes), \mathbf{u} is the input vector representing the stator and rotor voltages, \mathbf{A} is a matrix to be determined by combining the equations in (4.32) and (4.35).

The stator and rotor power expressions in per unit can be derived from the dq-components of the voltages and currents of the stator and rotor windings as in [25], pp. 277.

$$\begin{aligned} P_s &= \text{Re} \left\{ \underline{U}_{dq,s} \underline{I}_{dq,s}^* \right\} = U_{d,s} I_{d,s} + U_{q,s} I_{q,s}; & P_r &= \text{Re} \left\{ \underline{U}_{dq,r} \underline{I}_{dq,r}^* \right\} = U_{d,r} I_{d,r} + U_{q,r} I_{q,r} \\ Q_s &= \text{Im} \left\{ \underline{U}_{dq,s} \underline{I}_{dq,s}^* \right\} = U_{q,s} I_{d,s} - U_{d,s} I_{q,s}; & Q_r &= \text{Im} \left\{ \underline{U}_{dq,r} \underline{I}_{dq,r}^* \right\} = U_{q,r} I_{d,r} - U_{d,r} I_{q,r} \end{aligned} \quad (4.38)$$

The electromotive torque induced in the stator air gap (opposite to the turbine torque rotation) as a function of the stator fluxes and currents is given in per unit in [25], pp. 279 as:

$$T_{em} = \frac{\frac{3}{2} p \operatorname{Im}\{\underline{\psi}_{dq,s}^* \underline{I}_{dq,s}\}}{\frac{3}{2} U_b I_b \cdot \frac{p}{\omega_b}} = \operatorname{Im}\{\underline{\psi}_{dq,s}^* \underline{I}_{dq,s}\} = \psi_{d,s} I_{q,s} - \psi_{q,s} I_{d,s} \quad (4.39)$$

Then the swing equation for one-mass drive train model of the induction generator is given by:

$$\begin{aligned} \frac{d\delta}{dt} &= \frac{1}{p} (\omega - \omega_0) \\ \frac{d\omega}{dt} &= \frac{\omega_0}{2H} (T_m - T_{em} - D \Delta\omega) \end{aligned} \quad (4.40)$$

The complete asynchronous machine of the DFIG-based wind turbine is represented by the stator and rotor transients in (4.36), (4.39) and the rotor speed equations in (4.40).

4.6 Current-controlled converter voltage sources

As stated in section 2.3.3, the DFIG-based wind turbine consists of a back-to-back (BTB) partial-load converter (PLC) between the generator rotor and the grid. The BTB converter has two main subsystems, the rotor-side converter (RSC) and the grid-side converter (GSC). Both the RSC and GSC are supplied by DC voltage from the DC-link and phasor voltage from the pulse-width-modulation (PWM) generator. The PWM is regulated by the converter control units. The converter control consists of the RSC control unit that regulate the PWM of the rotor-side converter voltage source and the GSC control units that regulate the PWM for the grid-side converter voltage source. Both converter control units are regulated by inner-current control loops so that the rotor over-currents are limited. The detailed schematic diagram of such arrangements is shown in Figure 4.8. In this regard, the BTB converter is considered as two current-controlled voltage sources one to the generator rotor windings and the other to the GSC filter circuits.

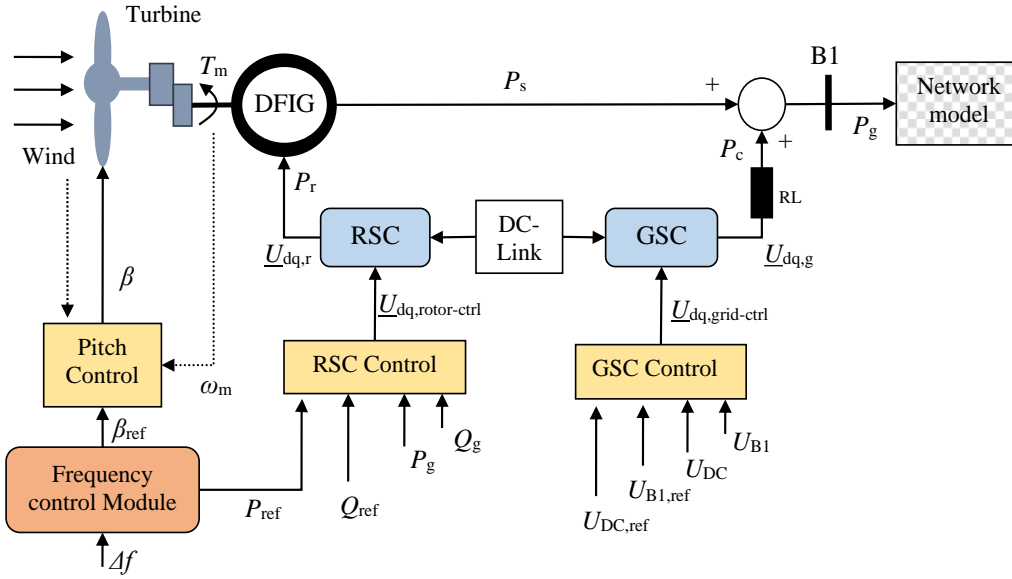


Figure 4.8 Schematic diagram of DFIG-based wind turbine control strategy [25]

Where, P_m , P_s , P_r and P_c are the mechanical turbine, stator, rotor and grid-side converter powers, respectively; P_{ref} and Q_{ref} are the reference rotor-side active and reactive power control of the PI controllers. $\underline{U}_{dq,r}$ and $\underline{U}_{dq,g}$ are the current-controlled converter voltage sources from the RSC and GSC, respectively; $\underline{U}_{dq,rotor-ctrl}$ and $\underline{U}_{dq,grid-ctrl}$ are the reference control voltages to the PWM in the RSC and GSC, respectively; U_{B1} and $U_{B1,ref}$ are the actual and reference bus-1 voltages in per units; similarly, U_{DC} and $U_{DC,ref}$ are the actual and reference DC-link voltages.

4.6.1 Rotor-side converter voltage source

The DFIG dynamic equations in (4.32) are used to develop the stator flux-oriented vector control strategy. Thus, to simplify and decouple the relations between reactive and active powers of the stator, a new frame of reference (named as vector control), as defined in Figure 4.9, is generally applied [25]. A vector control of DFIG is applied in a rotating dq-frame, where the d-axis is aligned with the stator flux space vector. Neglecting the resistance of the stator windings and the differential components in (4.32), the stator and rotor dynamics of the DFIG in dq-frame can be furtherly approximated as in (4.41).

$$\begin{aligned} \psi_{d,s} = \psi_s \quad \text{and} \quad \psi_{q,s} = 0 &\Rightarrow U_{d,s} = 0 \quad \text{and} \quad U_{q,s} = -R_s I_{q,s} + \psi_s \frac{\omega_s}{\omega_b} \approx \psi_s = U_s \\ \Rightarrow \underline{U}_s = U_s e^{j\delta} = U_s e^{j(\theta_s + \frac{\pi}{2})} &\rightarrow \theta_s = \delta - \frac{\pi}{2} \end{aligned} \quad (4.41)$$

Hence, the stator voltage magnitude U_s is approximately perpendicular to the stator flux magnitude ψ_s as can be estimated from the stator voltage equation by neglecting the stator resistance in (4.41). In Figure 4.9, the stator flux magnitude angle θ_s is derived from the stator voltage angle δ as in (4.41). Such stator magnetic fluxes are oriented along the d-axis in the synchronously rotating frame and will enable to independently control the active and reactive stator powers through the rotor-side converter as demonstrated in the subsequent sections.

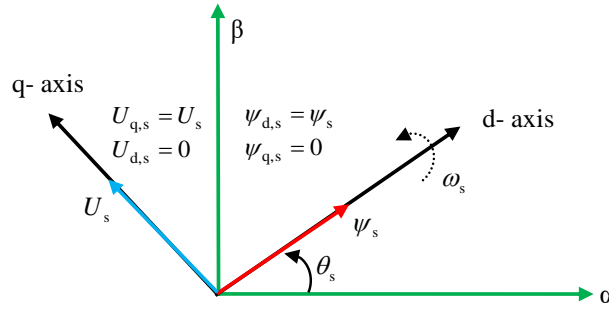


Figure 4.9 Synchronous rotating dq-frame aligned with the stator flux space vector [52]

With the new alignments of the stator voltages, the stator active power and reactive power in equation (4.38) can be expressed in terms of the stator flux magnitude and rotor currents by employing the algebraic equations in (4.31) and (4.41) as in (4.42) and (4.43), respectively.

$$P_s = \text{Re} \left\{ \underline{U}_{dq,s} \underline{I}_{dq,s}^* \right\} = -\frac{L_m}{L_s} (U_{d,s} I_{d,r} + U_{q,s} I_{q,r}) = \frac{L_m}{L_s} \psi_s I_{q,r} = K_T I_{q,r} \quad (4.42)$$

This reflects that there exists strong coupling between the q-axis rotor current and the stator active power. Similarly, the per unit stator reactive power is expressed as:

$$Q_s = \text{Im} \left\{ \underline{U}_{dq,s} \underline{I}_{dq,s}^* \right\} = \frac{L_m}{L_s} (U_{d,s} I_{q,r} - U_{q,s} I_{d,r}) - \frac{1}{L_s} \psi_s^2 = K_Q \left(I_{d,r} + \frac{\psi_s}{L_m} \right) \quad (4.43)$$

This relation again, indicates how firmly reactive power and d-axis element of the rotor current are coupled. Therefore, the stator active power and reactive power are regulated by the q- and d-components of the rotor windings, respectively. However, in this thesis work, the RSC is modelled as a voltage source and it is necessary to swing the control inputs to voltage by introducing current-controlled voltage source. In this regard, the rotor voltage equations will be emulated by a PI controller (inner-control loop) with rotor currents as control input. The reference d- and q-components of the rotor currents are in turn

regulated by the active and reactive power regulators (outer-control loop). The inner-control loop of the current-controlled voltage source is emulated from the rotor transients in (4.32) using the vector control approach as follows:

$$\begin{aligned} U_{d,r} &= R_r I_{d,r} - s \psi_{q,r} + \frac{d\psi_{d,r}}{dt} \\ U_{q,r} &= R_r I_{q,r} + s \psi_{d,r} + \frac{d\psi_{q,r}}{dt} \end{aligned} \quad (4.44)$$

Using equations (4.31), the rotor fluxes in (4.44) can be represented in terms of the rotor currents by applying the vector control orientation in (4.41):

$$\begin{aligned} \psi_{d,r} &= \left(L_r - \frac{L_m^2}{L_s} \right) I_{d,r} + \frac{L_m}{L_m} \psi_{d,s} = \sigma L_r I_{d,r} + \frac{L_m}{L_m} \psi_s \\ \psi_{q,r} &= \left(L_r - \frac{L_m^2}{L_s} \right) I_{q,r} = \sigma L_r I_{q,r} \end{aligned} \quad (4.45)$$

From equations (4.44) and (4.45), the rotor voltage and current relationship is expressed as follows:

$$\begin{aligned} U_{d,r} &= R_r I_{d,r} + \overset{\text{PI}}{\sigma L_r \frac{dI_{d,r}}{dt}} - s L_r I_{q,r} - s L_m I_{q,s} \\ U_{q,r} &= R_r I_{q,r} + \sigma L_r \frac{dI_{q,r}}{dt} + s L_r I_{d,r} + s L_m I_{d,s} \end{aligned} \quad (4.46)$$

Equation (4.46) shows that the rotor-side converter voltage source can be regulated by PI controller with the rotor currents as input parameters. With the stator flux space vector, the stator active and reactive power are independently controlled by rotor q-axis and d-axis currents as described in (4.42) and (4.43). For this reason, the rotor-side converter that supplies power to the rotor windings via slip rings is considered as a current-controlled voltage source. The d-axis and q-axis rotor voltages are controlled through the

respective reference rotor currents in the rotor current PI controller which in turn is regulated by the active power and reactive power PI controllers as in Figure 4.10.

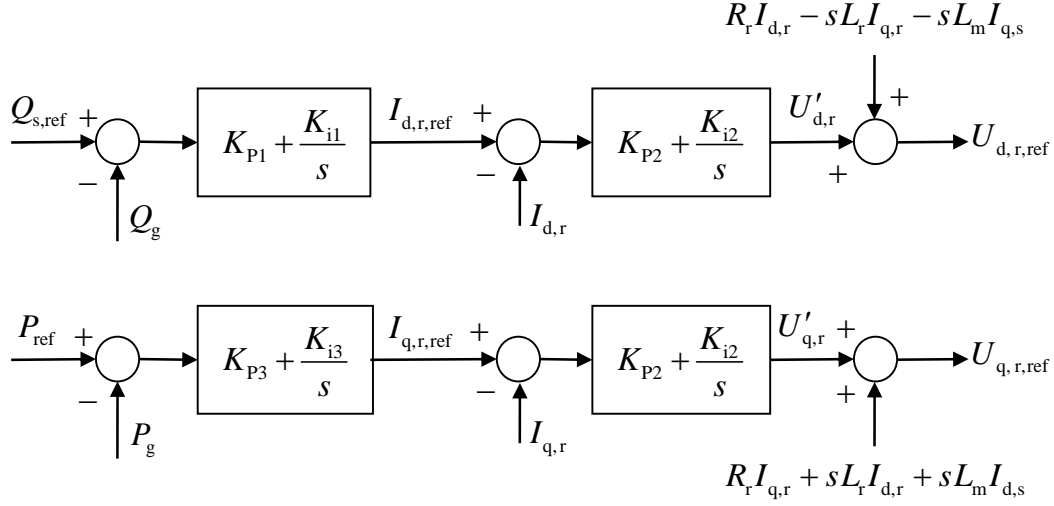


Figure 4.10 Block diagram of DFIG rotor-side converter control strategies [54]

The dynamic equations that represent the DFIG control strategy model in Figure 4.10 are expressed in (4.46).

$$\begin{aligned}
 \frac{dx_1}{dt} &= Q_{s,\text{ref}} - Q_s \\
 \frac{dx_2}{dt} &= I_{d,r,\text{ref}} - I_{d,r} = \frac{1}{K_Q} \left[K_{P1} (Q_{s,\text{ref}} - Q_g) + K_{i1} x_1 \right] - I_{d,r} \\
 \frac{dx_3}{dt} &= P_{\text{ref}} - P_g \\
 \frac{dx_4}{dt} &= I_{q,r,\text{ref}} - I_{q,r} = \frac{1}{K_T} \left[K_{P3} (P_{\text{ref}} - P_g) + K_{i3} x_3 \right] - I_{q,r}
 \end{aligned} \tag{4.46}$$

Where x_1 , x_2 , x_3 and x_4 are the intermediate differential state variables of the RSC outer- and inner control loops. K_{P1} , K_{P2} , K_{P3} and K_{i1} , K_{i2} , K_{i3} are the proportional and integral gains of the reactive power regulator, inner-loop current regulators and active power PI controllers, respectively. $Q_{s,\text{ref}}$ and P_{ref} are the reference or set stator reactive power and generator active power, respectively. The active power control reference is either the optimal turbine power at MPP, i.e., the optimal wind turbine output power that corresponds to the instant wind speed or a desired set value by the operators such as during de-loading operations due to load limitation requirements by the grid operators. P_g and Q_g are the

instant calculated active and reactive power at the grid point of connection. $I_{d,r}$ and $I_{q,r}$ are the instant rotor currents and $I_{d,r,ref}$ and $I_{q,r,ref}$ are the reference rotor currents which are regulated by the set values of the reactive and active powers in the outer-control loop. For turbines with MPP, P_{ref} can be taken from lookup tables from the manufacturer datasheet or can be calculated in each step using the corresponding rotor speed as in (4.47).

$$P_{ref} = P_{nom} \frac{\omega}{\omega_{nom}} \quad (4.47)$$

Where, P_{nom} and ω_{nom} are the nominal DFIG generator power and rotor speed, respectively. Using the expressions in (4.46) and Figure 4.10, the rotor-side current controlled reference voltage source ($\underline{U}_{dq,rotor-ctrl}$ as in Figure 4.8) is defined as:

$$\begin{aligned} U_{d,r,ref} &= K_{P2}((K_{P1}(Q_{s,ref} - Q_g) + K_{i1}x_1) - I_{d,r}) + K_{i2}x_2 + R_r I_{d,r} - sL_r I_{q,r} - sL_m I_{q,s} \\ U_{q,r,ref} &= K_{P2}((K_{P3}(P_{ref} - P_g) + K_{i3}x_3) - I_{q,r}) + K_{i2}x_4 + R_r I_{q,r} + sL_r I_{d,r} + sL_m I_{d,s} \end{aligned} \quad (4.48)$$

The modulation index for the current-controlled voltage source of the rotor-side inverter is calculated and transformed to rotor axis as follows:

$$\underline{U}_{dq,rotor-ctrl} = U_{m,r} e^{j(\theta_{r,ref} + \delta + \theta_{m,f})} \quad (4.49)$$

$$\text{Where; } \begin{cases} \underline{U}_{dq,r,ref} = U_{d,r,ref} + jU_{q,r,ref} = U_{dq,r,ref} e^{j\theta_{r,ref}} \\ U_{m,r} = \frac{2\sqrt{2/3}U_{nom}U_{dq,r,ref}}{U_{DC}} \\ \delta = \text{angle}(\underline{U}_{B1}) \text{ and } \theta_{m,f} = \text{angle}(\underline{\psi}_{dq,m}) \end{cases} \quad (4.50)$$

Note: \underline{U}_{B1} is the stator voltage at bus-1 in a-phase axis ($\alpha\beta$ -frame of reference).

An average model is adopted where the 2-level BTB converter is modeled as simple switches. Thus, the average rotor-side converter source voltage using the converter modulation index is calculated as:

$$\underline{U}_{dq,r} = \frac{U_{DC} \underline{U}_{dq,rotor-ctrl}}{2\sqrt{2/3} U_{nom}} \quad (4.51)$$

4.6.2 Grid-side converter voltage source

The grid currents are premeditated to regulate the source voltage of the grid-side converter so that the DC capacitor voltage is regulated to supply the desired DC-link voltage. In this analysis, the wind power plants are set to unity power factor at the grid-side converter so that the GSC has no contribution to the reactive power generation. Hence, the GSC is only responsible to regulate the bus voltage to constant value referred to the steady-state case. Such decoupling control strategy is developed in [54], by which the DC-link voltage and unity reactive power are independently regulated by the dq- current components of the grid-side converter system. This is achieved by aligning the stator voltage along the direction of the d-axis, i.e., $U_{d,s} = U_s$ and $U_{q,s} = 0$, whereas $U_{d,s}$ is equal to the magnitude of the generator bus voltage. Then, the DC-link voltage and the reactive power can be controlled independently by $I_{d,g}$ and $I_{q,g}$, respectively.

The DC-link outer-loop regulates the reference d-axis current of the grid-side converter. While the reference q-axis current is an external input to the model. In this thesis work, the GSC reactive power is set to zero in order to keep the grid-side converter power factor at unity. Hence, the reactive power is only supplied from the stator side. Applying, RL circuit, the PI-control blocks for GSC outer and inner-loop are presented in Figure 4.11.

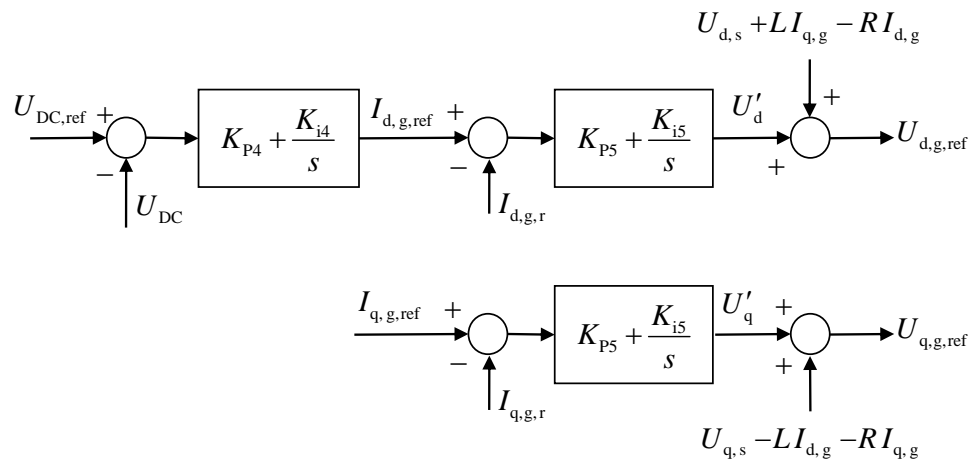


Figure 4.11 Block diagram of DFIG grid-side converter control strategies [54]

The dynamic equations that represent the GSC control strategy in Fig. 4.11 are derived as in (4.52).

$$\begin{aligned}
\frac{dx_5}{dt} &= U_{DC,ref} - U_{DC} \\
\frac{dx_6}{dt} &= I_{d,g,ref} - I_{d,g} = K_{P4} (U_{DC,ref} - U_{DC}) + K_{i4} x_5 - I_{d,g} \\
\frac{dx_7}{dt} &= I_{q,g,ref} - I_{q,g}
\end{aligned} \tag{4.52}$$

Where, x_5 , x_6 and x_7 are the intermediate differential state variables of the GSC outer- and inner control loops. K_{P4} , K_{P5} and K_{i4} , K_{i5} are the proportional and integral gains of the DC-link and inner-loop current-control PI regulators, respectively as in Figure 4.11.

Using the RL circuit in Figure 4.11 and equation (4.52), the current controlled grid-side reference voltage source ($\underline{U}_{dq,grid-ctrl}$ as in Figure 4.8) is defined as:

$$\begin{aligned}
U_{d,g,ref} &= K_{P5} \left(K_{P4} (U_{DC,ref} - U_{DC}) + K_{i4} x_5 - I_{d,g} \right) + K_{i5} x_6 - R I_{d,g} + L I_{q,g} + U_{d,s} \\
U_{q,g,ref} &= K_{P5} \left(I_{q,g,ref} - I_{q,g} \right) + K_{i5} x_7 - R I_{q,g} - L I_{d,g} + U_{q,s}
\end{aligned} \tag{4.53}$$

The dq-frame control voltage of the grid-side converter, using the modulation index, is calculated as in (4.54) and (4.56). Note also that the angle transformation shall be transformed back to the $\alpha\beta$ -axes frame.

$$\underline{U}_{dq,grid-ctrl} = U_{m,g} e^{j(\theta_{g,ref} + \delta)} \tag{4.54}$$

$$\text{Where; } \begin{cases} \underline{U}_{dq,g,ref} = U_{d,g,ref} + j U_{q,g,ref} = U_{dq,g,ref} e^{j\theta_{g,ref}} \\ U_{m,g} = \frac{2\sqrt{2/3} U_{nom} U_{dq,g}}{U_{DC}} \end{cases} \tag{4.55}$$

Then, the average grid-side converter voltage source model using the converter modulation index is calculated as:

$$\underline{U}_{dq,g} = \frac{U_{DC} \underline{U}_{dq,grid-ctrl}}{2\sqrt{2/3} U_{nom}} \tag{4.56}$$

The DFIG converter is connected to the grid through a series RL branch as in Figure 4.8. So that the dynamic grid-side currents in the RL branch and converter power P_c are calculated based on the voltage drop between the grid-side converter voltage source $\underline{U}_{dq,g}$ and the stator bus voltage $\underline{U}_{dq,s}$ as follows.

$$\begin{aligned}
L \frac{dI_{d,g}}{dt} &= -R I_{d,g} + L \omega_b I_{q,g} + U_{d,s} - U_{d,g} \\
L \frac{dI_{q,g}}{dt} &= -R I_{q,g} - L \omega_b I_{d,g} + U_{q,s} - U_{q,g}
\end{aligned}
\tag{4.57}$$

Using Laplace transformation in per unit quantities, the grid-side currents in the RL branch are also defined as:

$$\begin{aligned}
I_{d,g} &= \frac{\omega_b}{sL} (U_{d,s} - U_{d,g} - R I_{d,g} + L I_{q,g}) \\
I_{q,g} &= \frac{\omega_b}{sL} (U_{q,s} - U_{q,g} - R I_{q,g} - L I_{d,g})
\end{aligned}
\tag{4.58}$$

4.6.3 DC-link converter model

The back-to-back converter configuration of DFIG is presented in Figure 4.12. The active power flow of the converters at the DC-link is balanced using the equation in (4.59). Using the indicated directions of the currents, the DC-link power balance is expressed as

$$P_c = P_r + P_{DC} \tag{4.59}$$

Where P_r is the rotor-side converter active power at the AC terminal. P_c is the active power at the AC terminal of the grid-side converter and P_{DC} is the active power of the DC-link. In this thesis work, the DFIG is not supplied from any energy storage rather the DC-link control is aimed to regulate the DC voltage at its nominal value.

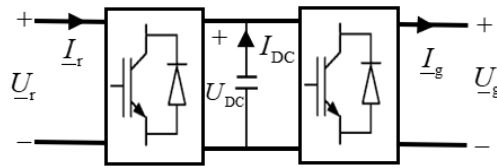


Figure 4.12 Equivalent circuit of DFIG back-to-back converter model [54]

Using the expressions in (4.35) for the rotor currents and (4.58) for RL branch currents, the rotor and grid-side power P_r and P_c are calculated from the rotor and grid-side voltages and currents as follows:

$$\begin{aligned}
P_r &= U_{d,r} I_{d,r} + U_{q,r} I_{q,r} \\
P_c &= U_{d,g} I_{d,g} + U_{q,g} I_{q,g}
\end{aligned}
\tag{4.60}$$

The DC-bus voltage is regulated by the error between the rotor power and grid-side converter power.

$$\frac{dU_{DC}}{dt} = \frac{1}{C U_{DC}} (P_c - P_r) P_{nom} \quad (4.61)$$

Where U_{DC} and I_{DC} are the capacitor DC voltage and current, respectively, and C is the capacitance of the DC-link.

4.6.4 Pitch control system

As pointed out in section 2.3.3, to regulate the variable input wind power, wind turbines are accompanied with wind turbine control modules that maintain the maximum power tracking for wind speeds below the rated value and limiting the output power when the wind speed is between the rated and cut-off values using pitch control system. Thus, the pitch angle control scheme for regulating the wind turbine mechanical power is depicted in Figure 4.13.

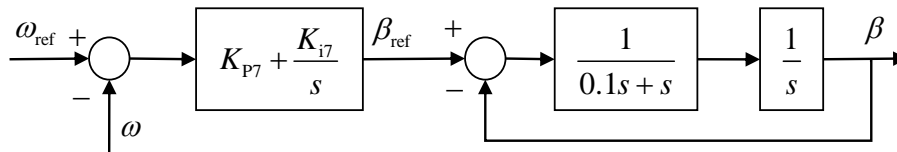


Figure 4.13 DFIG-based wind turbine pitch control system [35]

Where K_{p7} and K_{i7} are the pitch control proportional and integral gains, respectively. In Figure 4.13, the reference rotor speed ω_{ref} of the pitch angle PI regulator is taken as either an optimal rotor speed based on equation (4.2) or it is obtained from the reference power during load limitations such as de-loading operations as in (4.62).

$$\omega_{ref} = \frac{P_{ref}}{T_m} \quad (4.62)$$

Where P_{ref} is the reference set value or constrained turbine power due to load limitation of the generator output and T_m is the mechanical torque.

4.7 STATCOM for reactive power compensation

Unlike synchronous generators, wind induction generators lack in general reactive power contribution to the grid system. They rather consume reactive power for compensating

the voltage drops due to magnetizing. Thus, as an induction generator, DFIG generators need reactive power for their stable operation specifically during voltage dip conditions. Researches in the field have overcome the challenges related to reactive power compensation by integrating FACTS devices with RLC characteristics so that WTGs can operate safely during normal and abnormal conditions [12], [55], [56]. In this thesis, a voltage dip on the DFIG-based wind turbine is immediately compensated by a simplified STATCOM, which is described by a single time constant as in Figure 4.14. The static compensator STATCOM acts as a solid-state synchronous current source in analogy with a synchronous generator that generates balanced phase currents at the fundamental frequency with controllable magnitude and phase angle. The implemented STATCOM device, however, has no inertia and is not capable to regulate the active power.

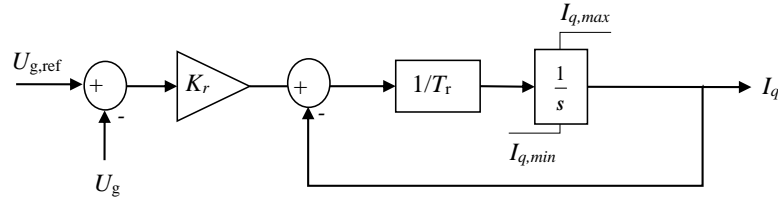


Figure 4.14 Block diagram of simplified STATCOM for RMS model [12]

The mathematical expression of the STATCOM in Figure 4.14 is presented in (4.63)

$$\begin{aligned} \frac{dI_q}{dt} &= \frac{1}{T_r} \left[K_r (U_{g,\text{ref}} - U_{B1}) - I_q \right] \\ Q &= I_q U_{B1} \end{aligned} \quad (4.63)$$

K_r is the STATCOM regulator gain, $U_{g,\text{ref}}$ and U_{B1} are the STATCOM reference voltage and the actual bus voltage magnitude at the point of connection, respectively. The parameters of the STATCOM regulator, K_r and T_r are tuned to act promptly to voltage sags at the bus. Q is the reactive power injected to the POC when the STATCOM is activated.

4.8 Wind turbine aggregation

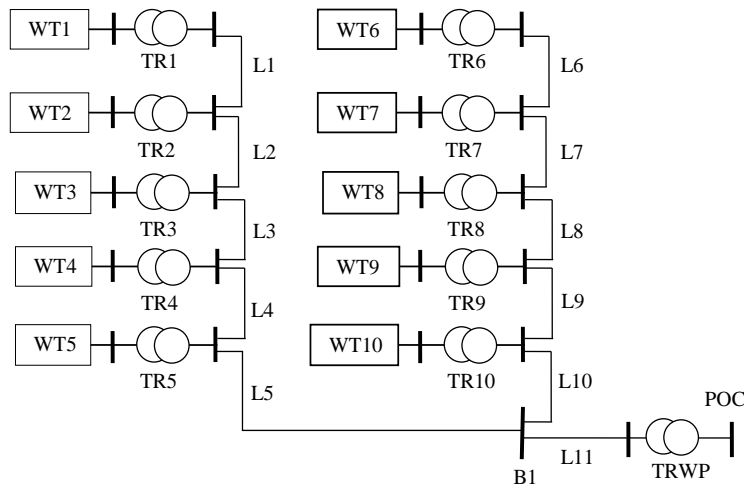
Wind turbines in a wind power plant which have similar wind speeds and environmental situations are aggregated into a group. The dynamic behaviors of individual WTGs are considered as one generator whose rating is the sum of each unit while the resistance and inductances in the stator and rotor are in per unit system and the ratio remain the same.

The line impedances for collecting lines of the wind turbines are aggregated as an equivalent parallel impedance as shown in Figure 4.15. The total active power demand obtained from load flow is shared equally to the operating wind generators in the group by assuming the wind speed in each wind turbine is uniform and remains constant during the simulation time. Since, each WTG is assumed to operate at the same condition, the total injected current of the aggregated WTGs at the k -th bus (B1) is the sum of each generator currents as shown in (4.64).

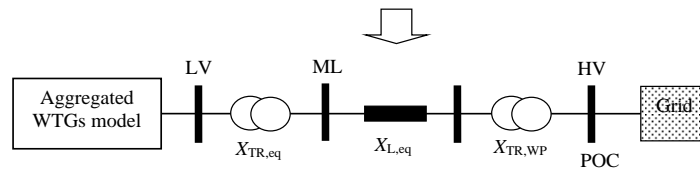
$$\underline{I}_{gw,k} = \sum_{i=1}^{n_{wg}} \underline{I}_{G,i} = \sum_{i=1}^{n_{wg}} (I_{d,g,i} + jI_{q,g,i}) e^{j\theta_{s,i}} \quad (4.64)$$

Where, $k = 1, 2, \dots, m_{wg}$ is the number of network buses where aggregated WPP are located; $i = 1, 2, \dots, n_{wg}$ is the number of WTG units in the k -th aggregated group; $\underline{I}_{gw,k}$ is the injected aggregated wind generators at the medium voltage side (MV) of the unit transformers which is named as ,stator bus, i.e., bus-1 (B1) in Figure 4.15 (a); θ_s is the terminal voltage angle which is also taken as the axis transforming angle for currents between dq-axes and $\alpha\beta$ -axes.

Figure 4.15 (a) aggregates two rows each with five WTGs into a single equivalent generator. The injected current, $\underline{I}_{gw,k}$ at the k -th wind power plant's substation is calculated by considering the equivalent circuit of the unit transformers (TR) and collecting lines between the unit transformers and the stator bus as depicted in Figure 4.15 (a). The equivalent impedance \underline{Z}_w between the aggregated stator node (B1) and network point of connection (POC) is represented by an equivalent impedance circuit of the wind plant step up transformer (TRWP) and that of the collecting lines (L5, L10 and L11) as shown in Figure 4.15 (b).



(a) Two rows each with 5-WTGs aggregation process



(b) Equivalent circuit of the aggregation model in (a)

Figure 4.15 Wind power plant aggregation model

4.9 Grid interfacing

The DFIG model in the dq-frame of reference is rotating at synchronous speed and the network is modelled in the $\alpha\beta$ -frame with $\underline{Y}_{KK,G}$ matrix that relates the injected currents and bus voltages. In a similar way as the synchronous generators are integrated to the grid, the DFIG are connected to the grid as depicted in Figure 4.16. The injected current of individual WTGs at the medium voltage side of the unit-transformer (stator bus) is the sum of the stator current \underline{I}_s and the current in the grid-side converter \underline{I}_c as in (4.65).

$$\underline{I}_{dq,GW} = (\underline{I}_{d,s} + \underline{I}_{d,g}) + j (\underline{I}_{q,s} + \underline{I}_{q,g}) \tag{4.65}$$

The per unit wind generator stator and rotor active powers are derived from the power equations in (4.38) or can be easily approximated from the phasor current \underline{I}_g and the stator bus voltage \underline{U}_{B1} as expressed in (4.66).

$$P_g + jQ_g = \underline{U}_{B1} \underline{I}_{dq,GW}^* \tag{4.66}$$

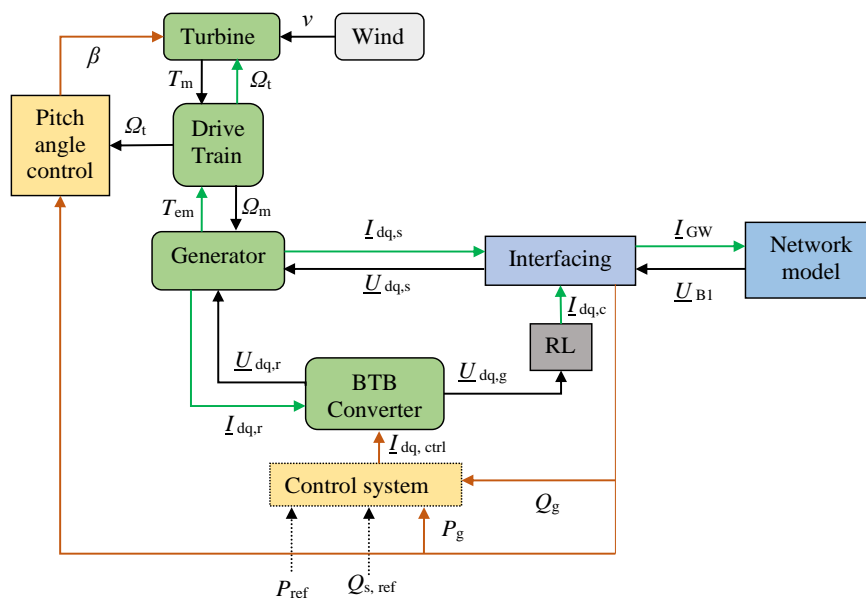


Figure 4.16 Complete DFIG model layout with interfacing to the grid system [52]

Once the generator injected current is determined in the dq-frame of reference, the dq-axes components are transformed to the grid system reference frame ($\alpha\beta$ -axes), which is done in the interfacing block of Figure 4.16. As discussed earlier, the rotating q-axis is set along the angle of the stator voltage from the real-axis of the network reference. Thus, the injected generator currents which are in the dq-axes frame are transformed to the network frame of reference and after solving the network equations, the stator voltages are transformed back from the network frame of reference to the DFIG dq-axes frame as shown in Figure 4.17. The per unit single-phase generator voltage and injected current, at medium voltage side of the unit transformer (B1 in Figure 4.16), are transformed from $\alpha\beta$ -axes to dq-axes and the other way round from dq-axes to $\alpha\beta$ -axes, respectively as in (4.67).

$$\begin{aligned}\underline{U}_{dq,s} &= \underline{U}_{B1} e^{-j\theta_s} \\ \underline{I}_{GW} &= \underline{I}_{dq,GW} e^{j\theta_s}\end{aligned}\quad (4.67)$$

Where, U_s and θ_s are the stator voltage magnitude and the stator flux angle from the synchronous reference as depicted in Figure 4.9.



Figure 4.17 Axis transformation between dq-frame and $\alpha\beta$ -frame [12]

Where, $\alpha\beta$ -axes denotes the network reference frame, and dq-axes denotes the local generator vector-oriented reference frame of an aggregated wind generator. Hence, $\theta_s = \delta - \pi/2$. where, δ is the angle between real axis of the $\alpha\beta$ -frame and q- axis of the dq-frame. Moreover, the power factor of the WTG is assumed to be constant at the grid-side converter so that the angle between voltage and current remains constant. Thus, the transformation axis between generator frame and network are similar for currents and voltages as in Figure 4.17.

5 Multi-machine Power System Representation for Transient Stability Studies

5.1 General

A power network operating in an equilibrium condition or in a situation that operates with sufficient stability margin is considered as steady-state. In reality, power systems in operation have always small load changes, some switching actions, and other small transients. Therefore, in the actual mathematical logic most of the variables are not or slightly time-variant. Such systems can be justified to be represented by an algebraic time-invariant model. On the other hand, large disturbances such as large load change and short-circuit fault events are clearly not at steady-state forms. Such fault events can lead to significant deviation of network states due to the distinct dynamic behaviors of the network elements. To study such dynamic behaviors, the transient analyses is needed.

In this thesis work, four test networks have been employed to simulate the dynamic behaviors of the network elements presented in the previous modeling sections. The dynamic characteristics and transient responses of DFIG-based wind turbines and its control capabilities have been studied and verified using a 4 - bus test system. The topology is similar to a single machine infinite bus (SMIB) system, which comprises an aggregated WPP, collecting lines, a transmission line and infinite bus.

The second network topology is the New England test grid (named as IEEE39-bus test system), which has been applied to evaluate the transient stability of the proposed models and investigate the dynamic impacts of integrating wind turbines. The machines are originally conventional synchronous steam generators. To observe the impact of increasing wind power share, some of them are step by step replaced by aggregated wind generators. Moreover, the simulation has been evaluated by replacing all generators with hydropower plants and then replacing them by wind generators to study the dynamic responses of hydro-dominant network topology. The STATCOM capability for correcting the voltage dip is also included and simulated in the IEEE39 bus system.

A third test network with two-bus system is included where the transmission network impacts are neglected as the intention of this simulation is mainly related with the active power balance between supply and demand. The network is solely used to study the primary frequency control capability of wind generators. In this regard, the grid frequency deviation is an important target which depends on the active power balance of the total generation supply and load. A frequency control module is integrated at the WPP level to dispatch the active power demand. The load has suddenly increased to observe the WPP

responses and taken measures to the grid frequency deviations. A fourth network topology is the case study on the Ethiopian power system, which is applied to examine the dynamic impacts of wind power increase on hydro-dominant grid system.

The steady-state equilibrium point of the test power networks are first determined through power flow analyses to initialize the differential and algebraic equations (DAEs) of the system variables. Then, the transient stability analyses of the networks for the various scenarios have been consecutively analyzed. The impacts of increasing wind power penetration levels on the dynamic network behaviors have also been assessed and presented in the proceeding sections.

5.2 Power flow Analysis

In the modelling section, the major elements of the electric network are represented by mathematical equations and the relations between individual components have to be furtherly studied to develop a complete representation of the whole electric network. Power flow analyses provides a solution for the power grid equations by computing the bus voltages, real power and reactive power flows at each bus. Based on the known variables of a bus and the operating conditions of a power system, power network buses are classified into three types [12], pp.111:

PU-bus: In such types of buses, voltage magnitude U and real power P are given while voltage angle θ and reactive power Q are unknown variables to be determined. The network element connected to the PU-bus is usually a generator.

PQ-bus: In PQ buses both real power P and reactive power Q are known while magnitude U and angle θ of the bus voltage are unknown. Loads are commonly connected to a PQ bus but also a bus can be PQ if the generator output power is constant or un-adjustable.

Slack-bus: The power loss of the network is initially unknown till the end of the power flow solution. So, a generator bus is usually selected and called slack bus whose voltage magnitude U and its phase angle θ are specified while the active and reactive power P and Q are unknown. With such bus assignment, the unknown power losses are added to this bus to balance the network's active and reactive power. It is also called swing bus or reference bus.

The power flow problem is basically formulated with the following four variables that are associated to each other at a particular bus:

- U magnitude of bus voltage
- θ Phase angle of bus voltage
- P active power (net sum of the generation and load)
- Q reactive power (net sum of generation and load)

The active and reactive power P and Q of a load bus may depend on the voltage magnitude and such load dependency characteristics are expressed by an exponential function as in [11].

$$P = P_0 \left(\frac{U}{U_0} \right)^{np} \quad (5.1)$$

$$Q = Q_0 \left(\frac{U}{U_0} \right)^{nq} \quad (5.2)$$

Where np and nq are the factors that define the voltage dependency characteristics of the load bus. There are three different cases that define the load characteristics.

- Power controlled load- $np, nq = 0$; for which active and reactive power are constant and do not depend on the voltage magnitude.
- Current controlled load- $np, nq = 1$; where active and reactive currents are constant and do not depend on the voltage magnitude (the power changes is proportional only to voltage change)
- Constant impedance load- $np, nq = 2$; where the admittance of the load remains constant while the active and reactive powers are proportional to the square of the voltage.

The relationships between voltage and current at each bus are formulated as non-linear set of equations [11]. The power network is modelled by its network admittance matrix \underline{Y}_{KK} to calculate the steady-state equilibrium point using the non-linear power flow equations in (5.3). Thus, the injected network apparent powers are given by (5.3).

$$\underline{s}_K = \underline{u}_K (\underline{i}_K)^* = \underline{U}_K (\underline{Y}_{KK} \underline{u}_K)^* \quad (5.3)$$

Where;

K bus number in a network.

\underline{s}_K K -size vector of bus injected apparent power in pu

\underline{i}_K K -size vector of bus injected currents in pu

\underline{u}_K K -size vector of bus voltages in pu

\underline{U}_K Diagonal matrix with K -size vector of bus voltages in pu

\underline{Y}_{KK} network admittance matrix in pu that comprises the models for all transmission lines and transformers in the network

The most common conventional methods used to solve the power flow equations are Newton-Raphson method, Gauss-Seidel method or Decoupling method [11]. The method

adopted in this thesis work is the Newton-Raphson solutions technique. Hence, the algebraic set of equations in (5.3) are solved iteratively using the Newton-Raphson algorithm. Depending on the type of buses, the voltage magnitude U and phase angle δ as well as the active and reactive power P and Q for all buses are calculated or set. Then, all variables of the dynamic model of a network are evaluated at the steady-state conditions. The Newton-Raphson network solutions and the dynamic system initializations are handled in MATLAB scripts as part of the research contribution.

In a power system, with K total number of buses, the net injected current at any k -th bus can be written in terms of admittance matrix \underline{Y}_{KK} and the bus voltages \underline{u}_K [57].

$$\underline{I}_k = \sum_{i=1}^K \left(Y_{k,i} e^{j\alpha_{k,i}} U_i e^{j\theta_i} \right) \quad (5.4)$$

Where $k = 1, 2, \dots, n$; $i = 1, 2, \dots, n$; U_i is the voltage magnitude at i -th bus; θ_i is the voltage angle at i -th bus; $Y_{k,i}$ is the admittance magnitude at (k,i) -element of the admittance matrix \underline{Y}_{KK} ; $\alpha_{k,i}$ is the admittance angle at (k,i) -element of the admittance matrix \underline{Y}_{KK} . Using the general equation in (5.4), with PU- buses $k = 1, 2, \dots, n_g$, the generator injected current at k -th bus is given by:

$$\underline{I}_{g,k} = \sum_{i=1}^K Y_{k,i} e^{j\alpha_{k,i}} U_i e^{j\theta_i} = (I_{d,k} + jI_{q,k}) e^{j\delta_k} \quad (5.5)$$

Where;

$\underline{I}_{g,k}$ the generator injected current at k -th bus

$I_{d,k}$ the d -axis generator terminal current at k -th bus (generator reference frame)

$I_{q,k}$ the q -axis generator terminal current at k -th bus (generator reference frame)

δ_k the generator rotor angle at k -th bus (i.e., the angle deviation of the generator rotor at k -th bus from the network reference frame)

Then, using the expression in (5.5), the net real and reactive injected power at the k -th generator bus is defined as in (5.6).

$$\begin{aligned} P_k + jQ_k &= \underline{U}_k \underline{I}_{g,k}^* = (P_{G,k}(U_k) - P_{D,k}(U_k)) + j(Q_{G,k} - Q_{D,k}) \\ &= U_k e^{j\theta_k} \sum_{i=1}^n Y_{k,i} U_i e^{-j(\alpha_{k,i} + \theta_i)} = \sum_{i=1}^n Y_{k,i} U_k U_i e^{j(\theta_k - \theta_i - \alpha_{k,i})} \\ &= \sum_{i=1}^n Y_{k,i} U_k U_i \cos(\theta_k - \theta_i - \alpha_{k,i}) + j \sum_{i=1}^n Y_{k,i} U_k U_i \sin(\theta_k - \theta_i - \alpha_{k,i}) \end{aligned} \quad (5.6)$$

Where;

$P_{G,k}$ real or active generated power at k -th bus

$Q_{G,k}$ reactive generated power at k -th bus

$P_{D,k}$ voltage dependent real demand power at k -th bus

$Q_{D,k}$ voltage dependent reactive demand power at k -th bus

The generator output power can be expressed in terms of the dq-axes generator currents in equation (5.5) and transformed to the network axis frame as in (5.7)

$$\begin{aligned} P_{G,k} &= \text{Real}\{U_k e^{j\theta_k} ((I_{d,k} + jI_{q,k}) e^{j\delta_k})^*\} = U_k I_{q,k} \cos(\delta_k - \theta_k) + U_k I_{d,k} \sin(\delta_k - \theta_k) \\ Q_{G,k} &= \text{Imag}\{U_k e^{j\theta_k} ((I_{d,k} + jI_{q,k}) e^{j\delta_k})^*\} = U_k I_{d,k} \cos(\delta_k - \theta_k) - U_k I_{q,k} \sin(\delta_k - \theta_k) \end{aligned} \quad (5.7)$$

Therefore, combining the expressions in equations (5.6) and (5.7), the grid power equations at the PU- bus are formulated as in (5.8)

$$\begin{aligned} U_k I_{q,k} \cos(\delta_k - \theta_k) + U_k I_{d,k} \sin(\delta_k - \theta_k) - P_D(U_k) - \sum_{i=1}^n Y_{k,i} U_k U_i \cos(\theta_k - \theta_i - \alpha_{k,i}) &= 0 \\ U_k I_{d,k} \cos(\delta_k - \theta_k) - U_k I_{q,k} \sin(\delta_k - \theta_k) - Q_D(U_k) - \sum_{i=1}^n Y_{k,i} U_k U_i \sin(\theta_k - \theta_i - \alpha_{k,i}) &= 0 \end{aligned} \quad (5.8)$$

In a similar fashion, for load buses (PQ buses, i.e., $k = n_g+1, n_g+2, \dots, n$) the power flow equations are derived from equation (5.6) as in (5.9)

$$\begin{aligned} P_{D,k}(U_k) - \sum_{i=1}^n Y_{k,i} U_k U_i \cos(\theta_k - \theta_i - \alpha_{k,i}) &= 0 \\ Q_{D,k}(U_k) - \sum_{i=1}^n Y_{k,i} U_k U_i \sin(\theta_k - \theta_i - \alpha_{k,i}) &= 0 \end{aligned} \quad (5.9)$$

Thus, the set of algebraic equations in (5.8) and (5.9) which are in the form of equation (5.3) are the non-linear power flow equations which need to be solved using Newton-Raphson techniques. Equations (5.8) and (5.9) represent the network algebraic equations and together with the dynamic models of synchronous, asynchronous generators and control dynamics form a complete power network model.

The Newton-Raphson iteration of the power flow equations in (5.8) and (5.9), with constant impedance loads, is formulated with the state vector of unknown voltage magnitudes \mathbf{u} and angles $\boldsymbol{\delta}$ as

$$\mathbf{x} = \begin{bmatrix} \boldsymbol{\delta} \\ \mathbf{u} \end{bmatrix} \quad (5.10)$$

The set of algebraic equations of the power flow form a non-linear function of $g(\mathbf{x}) = 0$. The non-linear set of equations are solved iteratively using the Newton-Raphson till the tolerance of the state deviations is achieved. The final values of the state variables at iteration $v+1$ is given by equation (5.11)

$$\mathbf{x}_{v+1} = \mathbf{x}_v + \Delta \mathbf{x}_v \quad (5.11)$$

Where the network state deviations $\Delta \mathbf{x}$ are approximated by linear systems using the Taylor series approach, which ignores the high order derivatives and results as in (5.12) [11].

$$\Delta \mathbf{x}_v = - \left[\frac{\partial g(\mathbf{x}_v)}{\partial \mathbf{x}} \right]^{-1} g(\mathbf{x}_v) \quad (5.12)$$

To solve the power flow, the Newton-Raphson iteration is formulated with the first components to match the active power while the last ones to reactive power. The set of active and reactive power deviation expressions, which are the state deviations $\Delta \mathbf{x}$, form the most famous linearized power flow equations in (5.13) as described in [12], [45].

$$g(\mathbf{x}) = \begin{bmatrix} \Delta \mathbf{p}_K \\ \Delta \mathbf{q}_K \end{bmatrix} = \begin{bmatrix} \frac{\partial \mathbf{p}_K}{\partial \delta_K^T} & \frac{\partial \mathbf{p}_K}{\partial \mathbf{u}_K^T} \\ \frac{\partial \mathbf{q}_K}{\partial \delta_K^T} & \frac{\partial \mathbf{q}_K}{\partial \mathbf{u}_K^T} \end{bmatrix} \begin{bmatrix} \Delta \delta_K \\ \Delta \mathbf{u}_K \end{bmatrix} = \mathbf{J} \begin{bmatrix} \Delta \delta_K \\ \Delta \mathbf{u}_K \end{bmatrix} \quad (5.13)$$

Where;

$\Delta \delta_k$ incremental change of the k -th bus voltage angle

$\Delta \mathbf{u}_k$ incremental change of the k -th bus voltage

$\Delta \mathbf{p}_k$ incremental change of the k -th bus real power

$\Delta \mathbf{q}_k$ incremental change of the k -th bus reactive power

Then the state deviations, $\Delta \mathbf{x}_v$ at iteration v are determined by evaluating the inverse of power flow Jacobian matrix $\mathbf{J}(\mathbf{x}_v)$ and the function $g(\mathbf{x}_v)$ as in (5.14).

$$\begin{bmatrix} \Delta \delta_K \\ \Delta \mathbf{u}_K \end{bmatrix} = - \begin{bmatrix} \frac{\partial \mathbf{p}_K}{\partial \delta_K^T} & \frac{\partial \mathbf{p}_K}{\partial \mathbf{u}_K^T} \\ \frac{\partial \mathbf{q}_K}{\partial \delta_K^T} & \frac{\partial \mathbf{q}_K}{\partial \mathbf{u}_K^T} \end{bmatrix}^{-1} \begin{bmatrix} \Delta \mathbf{p}_K \\ \Delta \mathbf{q}_K \end{bmatrix} \quad (5.14)$$

The new state variables, bus voltage angle and magnitude, are calculated as in (5.15).

$$\begin{bmatrix} \delta_{K,v+1} \\ \mathbf{u}_{K,v+1} \end{bmatrix} = \begin{bmatrix} \delta_{K,v} \\ \mathbf{u}_{K,v} \end{bmatrix} + \begin{bmatrix} \Delta \delta_{K,v} \\ \Delta \mathbf{u}_{K,v} \end{bmatrix} \quad (5.15)$$

The Newton-Raphson iteration repeats until the specified tolerance is achieved. When the specified tolerance is achieved, the new state values are considered as steady-state bus voltage profiles. Then, the per unit active and reactive injected power of each bus at steady-state condition are also determined as in (5.16).

$$\underline{\mathbf{s}}_K = \underline{\mathbf{U}}_K (\underline{\mathbf{Y}}_{KK} \underline{\mathbf{u}}_K)^* \quad (5.16)$$

For simplicity of the analyses, the steady-state loads are represented by their equivalent impedances $\underline{\mathbf{Y}}_L$ and the generator transient impedances matrix $\underline{\mathbf{Y}}_G$ for conventional generators are included with the bus admittance matrix, $\underline{\mathbf{Y}}_{KK}$ and form a time invariant network model, $\underline{\mathbf{Y}}_{KK,LG}$ as shown in (5.17).

$$\underline{\mathbf{Y}}_{KK,LG} = \underline{\mathbf{Y}}_{KK} - \underline{\mathbf{Y}}_L - \underline{\mathbf{Y}}_G \quad (5.17)$$

In such arrangements, as the large network admittances are sparse, the power flow solutions are reduced to only the buses that have injected currents such as generator buses, n_g and load buses which have voltage dependency behaviors, n_{dL} . Thus, the injected current vector ranges with $k = 1, 2, \dots, n_g + n_{dL}$ and are represented as a function of the sparse admittance matrix $\underline{\mathbf{Y}}_{KK,LG}$ with constant impedance approach, and the network state variable $\underline{\mathbf{u}}_K$ and the generators source currents $\underline{\mathbf{i}}_{gs}$ are related by algebraic equations in (5.18).

$$\underline{\mathbf{i}}_{gs} = \underline{\mathbf{Y}}_{KK,LG} \underline{\mathbf{u}}_K \quad (5.18)$$

If wind turbine generators are connected to the grid, then the network model in (5.18) is modified as described in section 4.6. Where, the unit transformer and the collecting lines between each group of wind generators and network bus (point of connection) are represented by an equivalent admittance of $\underline{\mathbf{Y}}_W$. Then the network model is extended to include W additional buses. Where, W is the total number of aggregated buses connected to the network buses.

The wind generators units in a wind power plant are grouped based on the aggregation principles in subsection 4.8. Each group of wind generators is represented by w -th additional node that connect the aggregated group to the main substation of the wind power plant through which the grid is connected. The equivalent admittance between the network k -th bus and the w -th aggregated wind generator bus is $\underline{\mathbf{Y}}_{W,k}$. Hence, $w = 1, 2, \dots, W$. where W is the total number of additional nodes that are added to the existing K -size

network buses. Thus, a wind farm may have W -size aggregated generators that are connected to the main substation. Using the wind turbines aggregation approach in Figure 4.15 (a), the current injected at such new node of a wind power plant are given by (5.19).

$$\underline{I}_{GW,k} = \underline{Y}_{W,k} (\underline{U}_{s,w} - \underline{U}_k) \quad (5.19)$$

Where $k = 1, 2, \dots$, and $w = 1, 2, \dots, W$ is the bus of aggregated wind generator; $\underline{U}_{s,w}$ is the w -th wind generator stator voltage, which is point B1 in Figure 4.15 (a). From equation (5.18), the current injected from the aggregated wind power plants is the voltage drop between the network node and the additional node at the generator stator. The admittance which is an equivalent of the unit transformers and collecting lines between the network bus and the generator stator bus (B1 as in Figure 4.5) is \underline{Y}_W . Using the current expression in (5.19), the aggregated wind power plant currents through their respective admittance \underline{Y}_W is given as in (5.20)

$$\underline{i}_{GW} = \underline{Y}_{WW} \underline{u}_{s,W} - \underline{Y}_{WK} \underline{u}_K \quad (5.20)$$

Where, \underline{Y}_{WW} and \underline{Y}_{WK} are diagonal matrices with W by W and W by K sizes, respectively. W is the size of the additional buses for the aggregated wind power plants while K is the size of the network nodes. Combining the current expressions in (5.18) and the network equation in (5.20), the network admittance extended to the wind turbine nodes is given in (5.21). The grid state variables, \underline{u}_K and the stator voltages of the wind generators at the low voltage side of the unit transformers, $\underline{u}_{s,w}$ are now determined from the solutions of the modified network model and the injected currents in (5.18) and (5.20) [36].

$$\begin{aligned} \begin{bmatrix} \underline{i}_{GW} \\ \underline{i}_{gs} \end{bmatrix} &= \begin{bmatrix} \underline{Y}_{WW} & \underline{Y}_{WK} \\ \underline{Y}_{WK}^T & \underline{Y}_{KKGLW} \end{bmatrix} \begin{bmatrix} \underline{u}_{s,W} \\ \underline{u}_K \end{bmatrix} \\ \Rightarrow \begin{cases} \underline{u}_K = [\underline{Y}_{KKGLW} - \underline{Y}_{WK}^T \underline{Y}_{WW}^{-1} \underline{Y}_{WK}]^{-1} (\underline{i}_{gs} - \underline{Y}_{WK}^T \underline{Y}_{WW}^{-1} \underline{i}_{GW}) \\ \underline{u}_{s,W} = \underline{Y}_{WW}^{-1} [\underline{i}_{GW} - \underline{Y}_{WK} \underline{u}_K] \end{cases} \end{aligned} \quad (5.21)$$

Where;

- \underline{u}_K vector of K -size network bus voltages
- $\underline{u}_{s,W}$ vector of W -size aggregated wind generator stator voltages at the extended buses
- \underline{i}_{gs} vector of synchronous generator source currents including all other PQ buses
- \underline{i}_{GW} vector of aggregated wind generators injected currents at the extended wind-buses
- \underline{Y}_{WK} the equivalent admittance of the transformers and collecting lines between wind generator buses W and network buses K .

$\underline{Y}_{KK,GLW}$ reduced nodal admittance that include the bus network \underline{Y}_{KK} , constant load admittances \underline{Y}_L , conventional generators' shunt admittances \underline{Y}_G and the equivalent admittance \underline{Y}_W for each group of wind generators.

Therefore, the power flow solutions, in (5.21), provide the bus voltages magnitude and angle as well as the injected active and reactive power of all buses which are the steady-state inputs to determine the initial conditions of the dynamic state variables of the conventional generator stations and wind power plants.

5.3 Transient stability analyses

Power system stability expresses the ability of a system to sustain the steady-state conditions or the abilities to attain a state of equilibrium after being subjected to disturbance [37]. Synchronous generators are still the most dominant type of generators in modern electrical power networks which are capable to operate in synchronism with the rest of the system. Any generator can be considered as synchronized with a network when both sides of the interconnection bus have the same frequency, voltage and phase sequences. Thus, power system dynamics can be generally classified in to three stability categories as shown in Figure 5.1.

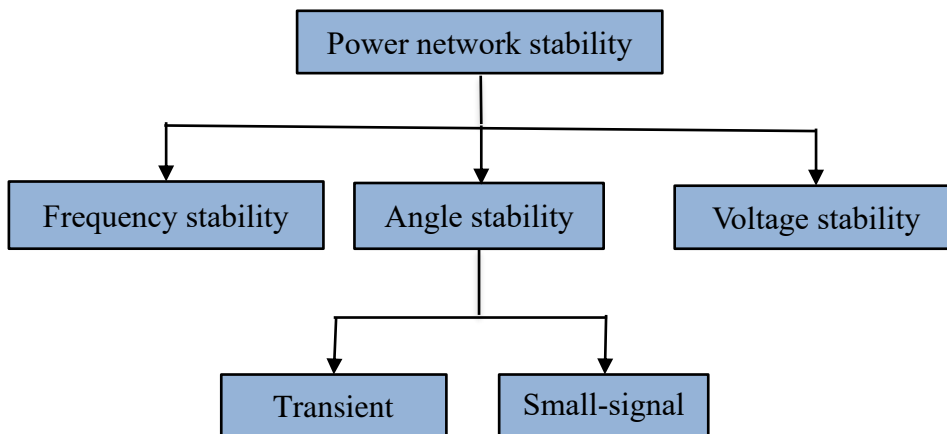


Figure 5.1 Structure for power network stability studies [37]

As defined earlier in this subsection, transient stability is the ability of a power system to stay in synchronism when subjected to small or large disturbances such as three-phase faults, large load variations or generator outages. Such transient disturbance results in large swings of output powers, rotor speeds, rotor angles and bus voltages at the generator terminal [37]. In transient stability analysis, the dynamic models are not-linearized due to the large disturbance's behaviors and for this reason numerical integration techniques are

applied to solve the problems. However, small signal stability deals with the ability of a system to be in synchronism when subjected to small disturbances such as small load changes [36]. For small disturbances, the network dynamic models can be linearized and analytical solutions can be applied such as the eigenvalue analysis.

During steady-state operation, all synchronous generators in the network rotate at constant speed and the rotor angle differences of any two generators remain constant. While, under any fault event, the generator rotors will accelerate or decelerate and their speeds will deviate from the steady-state values due to mismatch between the mechanical and electromagnetic torques (see Figure 3.5). Therefore, in such cases, the rotor angle differences between any two generators will also change. If the difference of rotor angle between any pair of generators coming back to steady-state point (not necessarily the same as previous), then the SGs are said to be in 'synchronism' and stable [58].

On the contrary, if the SGs lose synchronism after the fault event, the power system is entitled as instable. Under such circumstances, the output power, current, voltage, frequency etc. of the generator uninterruptedly drift away from the pre-disturbance equilibrium condition. If the transient sustainability indicates a violation or approaching to the stability boundaries, the system shall automatically prepare and activate corrective actions to maintain the sustainability of the power system.

Similarly, the frequency stability describes the ability of a power network to maintain stable frequency following severe or large system disturbance resulting in substantial imbalance between generation and load [37]. If the system frequency is not ultimately settled and correct measures are not taken in time, cascaded outages might be initiated and system separation into islands could eventually lead to a complete system blackout.

Modern power networks are significantly supplied from induction generators which are fully or partially isolated from the grid system such as the variable-speed wind generators, as studied in this thesis, which worsen the frequency stability boundaries [59]. To avoid getting involved in such situations, some preventive measures are taken such as under frequency load shedding [32]. However, under frequency load shedding is not normally recommended and so system sustainability shall be reinforced by employing other frequency control measures such as the virtual inertial responses, fast acting storage systems etc. so that the stability margin will remain as to the pre-disturbance condition.

The other important element of the power network stability analysis is voltage dynamics, specifically in weak grid system. Voltage stability states the ability of a power system to uphold steady voltages at all buses in the system after being subjected to disturbance [38]. Compared to synchronous generators, induction generators respond to fault events, such as changes in terminal voltage and frequency in a different way. Moreover, their capability to contribute to grid voltage control is limited [2], [59]. During large disturbances, induction generators may accelerate to high rotor speed and as a result absorb large amount of reactive power from the system, that can result in voltage collapse [50]. Thus,

it is essential to investigate how far the actual system is operating in regard to the voltage stability limits when the share of wind turbines is increasing.

5.4 Prediction methods for dynamic voltage stability margins

Voltage collapses occur when a power network is not proficient to withstand the dynamic imbalance of reactive power which could result due to heavy load changes or fault conditions [60]. A system is termed as voltage instable if at least one bus in the system has voltage magnitude U decreases while the reactive power injection, at the same bus is increasing. This implies that, when U - Q sensitivity is positive for all buses in the network then voltage is stable while if any bus has negative U - Q sensitivity, then the system is voltage unstable [11], [58].

There are several studies that have been performed with the voltage stability problem [59], [60], [61], [62], [63], [64], [65]. Most of these voltage stability analyses are used for determining the voltage stability problem for static analysis methods, based on two buses one as voltage source (Thevenin voltage) and the other as receiving end [48], [61] - [63]. Limitations of these indices is that they predict voltage instability based on the maximum line carrying capacity and the N-bus power network indices are extended from such two-bus system as described in [57].

The most commonly used bus voltage index, applicable for large networks, is the power transfer stability index (PTSI) in [64]. Where, the PTSI is calculated using (5.22).

$$\text{PTSI}_k = \frac{2 S_{L,k} Z_{\text{Thev},k} (1 + \cos(\alpha_k - \gamma_k))}{U_{\text{Thev},k}^2} \leq 1 \quad (5.22)$$

Where;

- α_k Thevenin impedance angle at k -th bus
- γ_k load impedance angle at k -th bus
- Z_{Thev} equivalent Thevenin impedance at k -th bus
- U_{Thev} source Thevenin voltage for k -th bus
- $U_{L,k}$ load apparent power at k -th bus

To ensure voltage stability, the PTSI must be between 0 and 1. The greater the PTSI value the more unstable the condition. Hence, the dynamic voltage stability margin of a load bus is the difference in voltages at steady-state and the value that correspond to the maximum PTSI. The voltage at maximum PTSI is a critical (collapse) voltage, which is a voltage corresponding to PTSI equal to one. The PTSI will be calculated by increasing the active power at a bus step by step while projecting the power-voltage (P-U) curve.

The dynamic voltage stability indices for large networks including the wind turbine generators are analyzed in the subsequent sections. However, to realize the voltage collapse problem in detail, a two-bus network, as in Figure 5.2, is applied in this subsection.

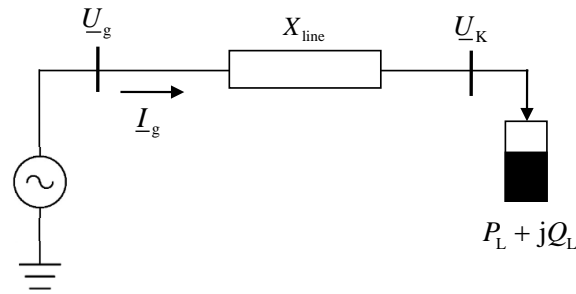


Figure 5.2 A load connected to infinite bus

The active power-voltage curve (P-U curve) is a widely used method of foreseeing voltage collapse margins. The P-U curves are generally used to predict the loading margin of a power system using the distance (power difference) from the actual operating point to the minimum (critical) voltage. The critical voltage bus is defined as the weakest bus that runs first into voltage collapse when the system is being subjected to disturbances. The static and dynamic voltage stability criterion is then evaluated from the current operating power and the maximum power [65]. A typical P-U curve, in Figure 5.3, is shown for a constant power load coupled through a transmission line to an infinite-bus.

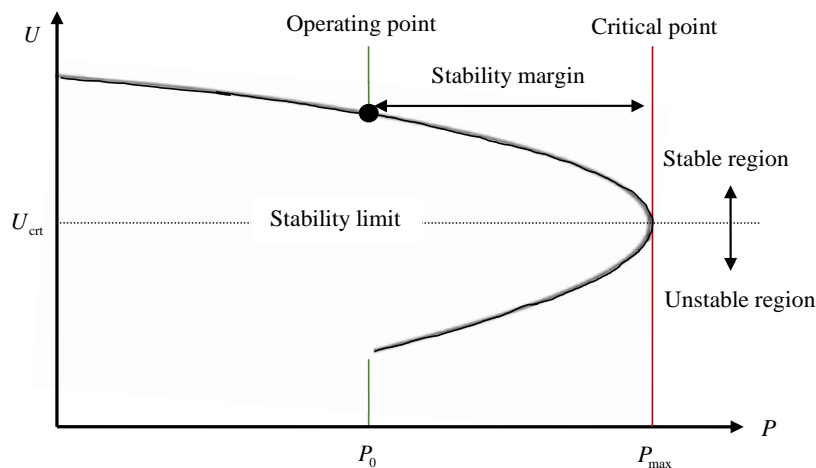


Figure 5.3 Typical P-U curve of a load connected to infinite bus [58]

Figure 5.3 is obtained by applying the power flow solutions, where the load power P is varying slowly till the nose of the curve and U is the corresponding voltage magnitude at the load bus. The top portion of the curve in Figure 5.3 is stable operation whereas the

bottom half is taken to be the instable operation. The risk of voltage collapse is much lower if the bus voltage is further away from the critical voltage corresponding to P_{\max} .

The maximum transmissible power to the load, for the network in Figure 5.2, is calculated at different scenarios such as varying the voltage source U_p or different reactive power at the load bus, i.e., by varying the load power factor angle (load angle) γ_k .

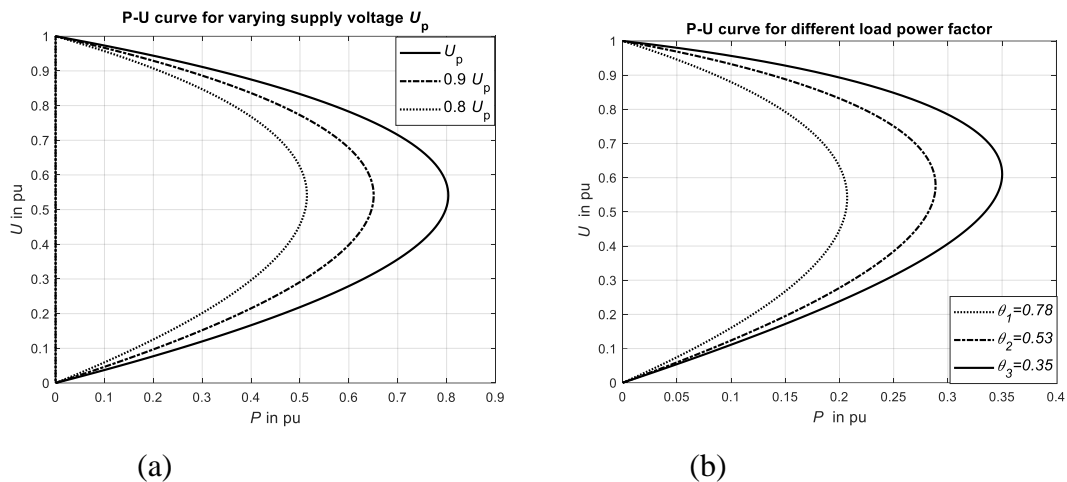


Figure 5.4 P-U curves of three voltage source cases (a) and three cases of load PF (b)

Figure 5.4 shows the P-U curves for various cases of source voltage and load angle to realize their impact on the maximum transferable power to the load. When the source voltage magnitude is decreasing the nose of the P-U curve is shrinking, i.e., decreasing the critical voltage operation as in (a). In Figure 5.4 (b), it can be seen that the maximum transmissible power rises when the load power factor is leading, since load compensation rises. The transmissible power in each step matches to a value of the voltage at the bus until its critical point is reached, i.e. further increase in power results in voltage instability.

Analyzing the voltage collapse problem as in the above is helpful to relate and realize the impacts of integrating large-scale wind power plants which normally create voltage dips and consume reactive power from the system.

5.5 Calculation of initial conditions

Before doing transient stability analyses, a system with its generators, loads and network should be initialized to the steady-state condition. The power system is represented by an admittance matrix, \underline{Y}_{KK} as in section 5.2 and the load flow defines the steady-state operating point with estimated node voltage and network power flows. The consistent steady-state of the network is the initial state of any power system dynamic simulations. The load flow results and the steady-state power network model are used to initialize the dynamic models.

Initialization in this thesis work represents calculation of the initial values of all dynamic variables at their steady-state condition. Initialization of the dynamic variables for synchronous generators and DFIG-based wind turbines are calculated based on the load flow results in (5.16) and (5.17). Initialization of the excitation system, turbine-governor system, DFIG converter control and other voltage and frequency regulators are realized by making all differential equations equal to zero. Thus, if the initial conditions of generators are determined, initializing the control elements is straightforward and for this reason, its details are not included in the thesis report.

5.5.1 Initialization of the dynamic models of synchronous generators

The network buses with synchronous generators are considered as PU buses and one of these generation stations may or may not be accounted as slack bus. Thus, the power flow solutions in section 5.2 provide the steady-state values of the grid states (voltage magnitude and angle) as well as the injected bus active and reactive powers. Based on these results, the initial values of the DAE variables in equation (3.16) are calculated. In steady-state, the derivative terms in (3.16) are equal to zero and by using the stator equations, the generator terminal voltage is represented as in (5.23).

The network states are in the synchronous frame of reference while the dynamic models of the generators are in their respective dq-frame of reference as described in Figure 3.9 in section 3.4. Thus, an axis transformation is applied using the rotor angle. The initial rotor angle δ is the same as the internal voltage angle behind the q-axis reactance, i.e., the steady-state phasor internal voltage lies along the q-axis. This can be verified by adopting the algebraic stator equations in (3.9) into voltage phasor representations, without the dummy coil, as in (5.23).

$$\begin{aligned}
 U_{d,s} + jU_{q,s} &= -R_s I_{d,s} + X'_q I_{q,s} + U'_d + j(-R_s I_{q,s} - X'_d I_{d,s} + U'_q) \\
 &= j((X_q - X_d) I_{d,s} + U_{d,f}) - (R_s + jX_q) (I_{d,s} + jI_{q,s}) \\
 &= 0 + j\underline{U}'_q - (R_s + jX_q) (I_{d,s} + jI_{q,s}) \\
 &= \underline{U}'_{dq} - (R_s + jX_q) (I_{d,s} + jI_{q,s})
 \end{aligned} \tag{5.23}$$

Where $\underline{U}'_{dq} = jU'_q$, represents the internal transient voltage which proves that the steady-state generator internal voltage lies in the q-axis behind the reactance X_q (note that the internal voltage is not expressed behind the transient reactance X'_d). Thus, the initial rotor angle and the transient internal voltage magnitude can be directly calculated from the load flow results. By transforming the dq-axes frame of equation (5.24) to the network reference frame ($\alpha\beta$ -axes), the initial magnitude of the internal generator voltage magnitude

which lies along the q-axis U'_q and the corresponding initial rotor angle δ of a synchronous generator at the k -th bus are calculated using (5.24).

$$U'_{q,k} e^{j\delta_k} = \underline{U}_k + (R_s + jX_q) \underline{I}_k \quad (5.24)$$

Where k is the generator bus number, \underline{U}_k and \underline{I}_k are the complex voltage and injected current at the k -th generator bus which are solutions of the load flow analyses. R_s and X_q are the synchronous generator stator resistance and q-axis reactance, respectively.

After the internal voltages are determined, the next step is to calculate the dq-axis components of stator voltages and currents by applying the axis transformation in (3.14) from the load flow quantities. Thus, the dq-axis components of the generator stator voltage and current at the k -th bus are obtained from the phasor representations in (5.25)

$$\begin{aligned} U_{d,s,k} + j U_{q,s,k} &= \underline{U}_k (\sin \delta_k + j \cos \delta_k) \\ I_{d,s,k} + j I_{q,s,k} &= \underline{I}_k (\sin \delta_k + j \cos \delta_k) \end{aligned} \quad (5.25)$$

Where $U_{d,s,k}$, $I_{d,s,k}$, $U_{q,s,k}$ and $I_{q,s,k}$ are the dq-axes frame components of the k -th bus stator voltage and currents, respectively. δ_k is the rotor angle in radians while \underline{U}_k and \underline{I}_k are the load flow quantities in $\alpha\beta$ -frame (network reference frame) at the k -th bus. The excitation initial voltage $U_{d,f}$ is obtained by equating the differential term in (3.16) equal to zero and rearranging as in (5.26).

$$U_{d,f,k} = U'_{q,k} + (X_d - X'_d) I_{d,s,k} \quad (5.26)$$

Then, the other dynamic variables of the synchronous generator, excitation system, turbine-governor systems are straightforward to calculate from their respective dynamic equations by setting the differential terms equal to zero and using the generator quantities from (5.24) to (5.26).

5.5.2 Initialize the dynamic models of wind generators

The influence of increased wind power on power system dynamic behaviors are studied by substituting the existing conventional generators with wind power generators. The initial calculation of DFIG generators is not direct and easy like the synchronous generators. The dq-axes model of the DFIG is exploited further in order to calculate the initial values of the machine variables at a steady-state condition. The DFIG-based wind power plants are assumed to operate at their steady-state conditions till a fault event occurs.

In steady-state operation, the DFIG control is intended to maintain the generator rotor speed at its optimal torque/speed characteristic. Thus, it is convenient to initialize the

DFIG-based wind turbine based on the optimum power extraction characteristic, i.e., the injected active power of the generator bus is equal to the mechanical input power $P_G \approx P_m$ by neglecting the losses. It is also possible to use the generator efficiency and estimate the input turbine power. Therefore, the rotor speed in electrical rad/sec that corresponds to the steady-state operation is calculated based on the aerodynamic equations in (4.7) and then the wind turbine generator slip ratio and mechanical torque are calculated as in (5.27).

$$\omega = p \Omega_m = p \left(\frac{P_m}{K_{opt}} \right)^{1/3} \Rightarrow \begin{cases} s = \frac{\omega_s - \omega}{\omega_s} \\ T_{em} = \frac{P_m}{\Omega} \end{cases} \quad (5.27)$$

The load flow inputs to the DFIG-based wind turbine dynamic models are the $P_{g,k}$, $Q_{g,k}$ and \underline{U}_k . Then the rotor speed Ω_m , rotor slip s and the mechanical torque T_{em} are calculated in steps as in (5.27).

The control strategies are now enabling to keep the equilibrium point by deducing the remaining electric variables of the machine at steady-state operation such as generator and converter currents, voltages and powers. In steady-state condition, the stator differential equations in (4.32) are equal to zero and presented in (5.28). Moreover, the per unit wind generator stator and rotor active powers are derived in a similar approach as in (4.40) with electromagnetic torque as a function of the stator flux and currents.

$$\begin{aligned} 0 &= U_{q,s} - R_s I_{q,s} - \omega \psi_{d,s} \\ 0 &= U_{d,s} - R_s I_{d,s} + \omega \psi_{q,s} \\ T_{em} &\approx P_s = \psi_{d,s} I_{q,s} - \psi_{q,s} I_{d,s} \\ Q_s &= \psi_{d,s} I_{d,s} + \psi_{q,s} I_{q,s} \end{aligned} \quad (5.28)$$

Equation (5.28), has six unknown variables and there are only four equations. To solve this set of algebraic equations, two more equations are required. Thus, one additional equation can be obtained from the magnitude of the load flow bus voltage, i.e., $\underline{U}_k = U_s e^{j\theta}$. To initialize the induction generator, the stator flux orientation control strategy is applied as in (4.41), where the stator flux is oriented along the d-axis, i.e., $U_{q,s} = U_s = \Psi_s$. Moreover, assuming the initial synchronous stator frequency is the same as the base value that is $\omega_s = \omega_b \rightarrow \omega = 1$, then the following reduced five equations in the per unit system are applied to estimate the initial stator flux magnitude Ψ_s as in (5.29).

$$\left. \begin{aligned} U_{d,s} &= R_s I_{d,s} \\ U_{q,s} &= R_s I_{q,s} + \psi_s \\ T_{em} &= \psi_s I_{q,s} \\ Q_s &= \psi_s I_{d,s} \\ U_s^2 &= U_{d,s}^2 + U_{q,s}^2 \end{aligned} \right\} \Rightarrow \psi_s = \sqrt{\frac{-B \pm \sqrt{B^2 - 4C}}{2}} \Rightarrow \begin{cases} B = 2R_s T_{em} - U_s^2 \\ C = R_s^2 (Q_s^2 + T_{em}^2) \end{cases} \quad (5.29)$$

After the stator flux magnitude Ψ_s is determined, the rest of the initial parameters of the dynamic equations are easily determined in the dq-frame as in (5.30).

$$\left. \begin{aligned} I_{d,s} &= \frac{Q_s}{\psi_s} \\ U_{d,s} &= -R_s I_{d,s} \\ I_{d,r} &= \frac{-\psi_s - L_s I_{d,s}}{L_m} \\ \psi_{d,s} &= -L_s I_{d,s} - L_m I_{d,r} \\ U_{d,r} &= -R_r I_{d,r} + s \sigma L_r I_{q,r} \\ \psi_{d,r} &= -L_m I_{d,s} - L_r I_{d,r} \\ P_s &= U_{d,s} I_{d,s} + U_{q,s} I_{q,s} \\ P_r &= U_{d,r} I_{d,r} + U_{q,r} I_{q,r} \end{aligned} \right| \left. \begin{aligned} I_{q,s} &= \frac{T_{em}}{\psi_s} \\ U_{q,s} &= -R_s I_{q,s} + \psi_s \\ I_{d,r} &= -\frac{L_s}{L_m} I_{q,s} \\ \psi_{q,s} &= -L_s I_{q,s} - L_m I_{q,r} \\ U_{q,r} &= -R_r I_{q,r} - s \sigma L_r I_{d,r} + s L_m \psi_s / L_s \\ \psi_{q,r} &= -L_m I_{q,s} - L_r I_{q,r} \\ Q_s &= U_{q,s} I_{d,s} - U_{d,s} I_{q,s} \\ Q_r &= U_{q,r} I_{d,r} - U_{d,r} I_{q,r} \end{aligned} \right\} \quad (5.30)$$

If the initial conditions of the DFIG-based wind turbine dynamic equations are correctly determined, the DAEs variables remain in steady-state until any disturbance is occurring in the system. Thus, one way to validate a model is to solve the set of DAEs using numerical integrations without any disturbance for longer time for which the time simulation results are expected to remain at their steady-state values as far as there is no disturbance in the system. Then, the steady-state operation of the DFIG-based wind turbine model has been evaluated at different wind speeds ranging from values below cut-in speed to above cut-out speeds. Analyzing the steady-state condition is crucial to assure the wind turbine operation is as per the manufacturer datasheet power curve and discourse the operation behaviors before entering the transient analysis.

In the simulation, two types of DFIG-based wind turbines have been considered to study the steady-state operation. The simulation input data for the two types of DFIG-based wind turbines are given in Table 5.1 and Table 5.2. The detailed parameters for the dynamic analyses of the generic models of the wind turbines are given in Appendix A.

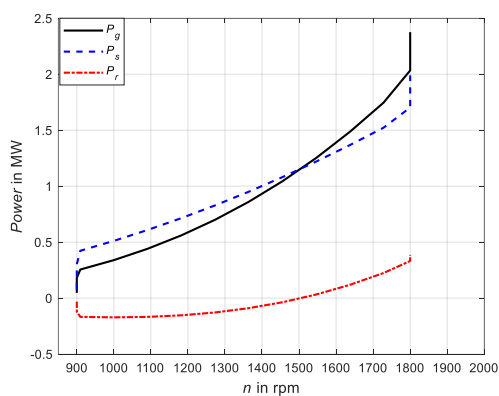
Table 5.1 Parameters of 2 MW DFIG [26]

Rated power	2 MW	Stator resistance	0.00488 Ω	Cut-in wind speed	4 m/s
Rated voltage	690 V	Stator linkage inductance	0.09241 H	Rated wind speed	12m/s
Rotor diameter	84 m	Mutual inductance	3.9527 H	Cut-out wind speed	25m/s
Number of Poles	4	Rotor resistance	0.00488 Ω	Optimal pitch angle	0 ⁰
Min. rotor speed	9 rpm	Rotor linkage inductance	0.09955 H		
Max. rotor speed	18rpm	Stator/rotor turns ratio	1/3		

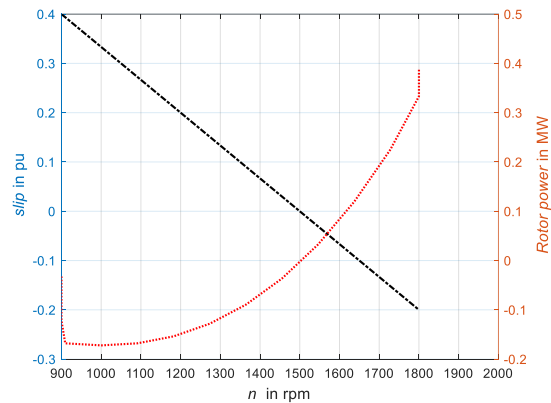
Table 5.2 Parameters of 1.5 MW DFIG [48]

Rated power	1.5MW	Stator resistance	0.0071 Ω	Cut-in wind speed-	4 m/s
Rated voltage	575 V	Stator linkage inductance	0.171H	Rated wind speed	13.3m/s
Rotor diameter	38 m	Mutual inductance	3.90 H	Cut-out wind speed	22 m/s
Number of Poles	6	Rotor resistance	0.005 Ω	Optimal pitch angle	0 ⁰
Min. rotor speed	9 rpm	Rotor linkage inductance	0.156H		
Max. rotor speed	22 rpm	Stator/rotor turns ratio	1/3		

The steady-state results in Figure 5.5 and Figure 5.6 illustrate the DFIG-based wind turbine response for an increasing rotor speed input which corresponds to variable wind speeds. Figure 5.5 (a) shows the DFIG variable characteristics plots for air-gap induced stator power, rotor power and the total generator active power. The output generator power is the sum of the rotor and stator where the stator power is the major contributor. After the rated wind speed that corresponds to the maximum rotor speed, the WTG output power is controlled and remains at its rated value of 2 MW.



(a) Stator, rotor and grid powers



(b) slip and rotor power

Figure 5.5 The steady-state generated power P_g , stator power P_s and rotor power P_r (in a) rotor power and rotor slip characteristics (in b) for varying rotor speed

The rotor slip has initially positive value until the turbine reaches its nominal value at 1500 rpm so that the generator is in sub-synchronous operation. At nominal speed, the

generated power and the stator power are equal as the rotor does not contribute any power (see Figure 5.5 (b)). Moreover, in the super-synchronous operation the slip become negative and the rotor starts generating power and add up to the stator so that the generator output is above the stator power. The results in Figure 5.6 (a) show the stator and rotor voltage and current responses to the varying rotor speed inputs. The steady-state stator voltage remains constant as it is determined by a change in the network while the rotor voltage is the control output. Its steady-state result is varying in response to the variable wind speed. Similarly the stator and rotor currents, in Figure 5.6 (b), are increasing to increase the output powers as per the control strategies discussed in (4.47).

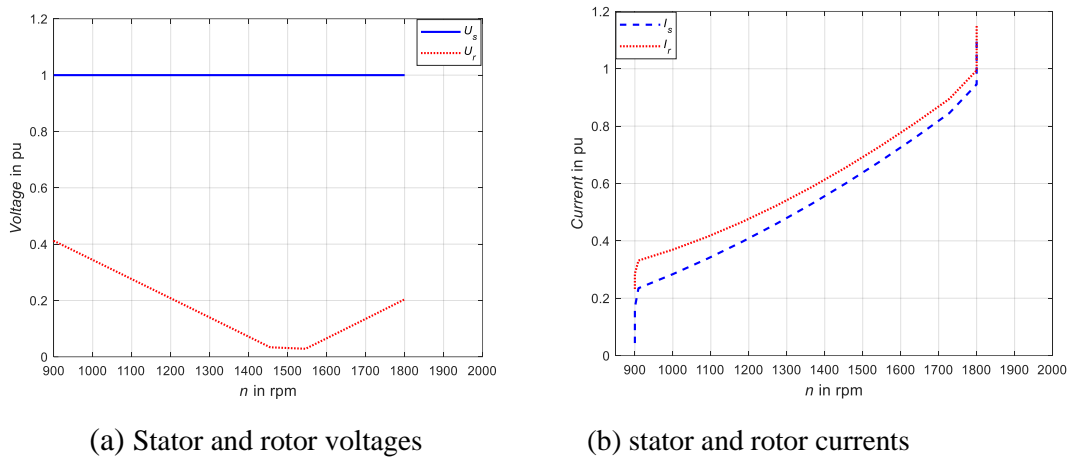


Figure 5.6 DFIG steady-state outputs (a) stator and rotor voltages (b) stator and rotor currents for varying rotor speed

During normal operation, integration of wind turbines may affect the voltage profiles in the network due to the variations of load characteristics. There are grid codes which define the utility requirements for wind farm integration at the POC [11]. Thus, the wind power plant operators are obliged to ensure that the wind farm does not breach the voltage level outside the required limits. For this reason, in this thesis work, appropriate protection for the stator under/over voltage and currents have been considered in the model.

5.6 Numerical solutions of power network dynamic models

The dynamic model of synchronous generators for the conventional generation, induction generators for the wind power plants, mechanical dynamics and associated control strategies along with the grid power flow equations characterize the power system dynamics. After calculating the initial conditions of all state variables in the network, the set of differential algebraic equations (DAEs) are organized and solved using numerical integrations as in (5.31).

$$\begin{aligned}
\dot{\mathbf{x}} &= \mathbf{f}(\mathbf{x}, \mathbf{i}_{dq}, \mathbf{u}_K, \mathbf{v}) \\
\mathbf{i}_{dq} &= \mathbf{h}(\mathbf{x}, \mathbf{u}_K) \\
\mathbf{0} &= \mathbf{g}(\mathbf{x}, \mathbf{i}_{dq}, \mathbf{u}_K)
\end{aligned} \tag{5.31}$$

Where;

- \mathbf{f} set of first order differential equations (representing power network dynamics)
- \mathbf{h} set of algebraic stator equations (related to generator-grid integration circuits)
- \mathbf{g} set of algebraic network equations (power flow equations)
- \mathbf{x} vector of dynamic state variables
- \mathbf{i}_{dq} vector of generator terminal currents injected to the networks in dq-reference frame
- \mathbf{u}_K vector of network bus voltages to be calculated using the power flow equations
- \mathbf{v} vector of system inputs

Then, the set of DAEs in (5.31) is solved in the time-domain simulation by means of numerical integration techniques. The fifth and sixth order Runge-Kutta methods have been adopted in this thesis work.

As described in section 3.3, the complete model of a conventional power plant at bus i is represented by the dynamic equations of the 4th-order model of synchronous generator in (3.16), IEEE-type DC1A voltage regulator in (3.19) or the ST1A exciter in (3.17) and hydro turbine governor system in (3.20). The vectors related to such i -th bus state variables \mathbf{x} , auxiliary or intermediate variables $\mathbf{i}_{dq,i}$, bus voltage \mathbf{u}_K and inputs \mathbf{v} are defined in (5.32).

$$\begin{aligned}
\mathbf{x}_i &= [\delta_i, \omega_i, U_{d,i}', U_{q,i}', U_{d,f,i}, U_{R,i}, R_{F,i}, X_{1,i}, X_{2,i}, P_{m,i}]^T; \\
\mathbf{i}_{dq,i} &= [I_{d,i}, I_{q,i}]^T; \quad \mathbf{v}_i = U_{ref,i}; \\
\mathbf{u}_K &= [U_1, U_2, \dots, U_K]^T;
\end{aligned} \tag{5.32}$$

Where K is the number of network nodes and n_g is the number of synchronous generations and $i = 1, 2, \dots, n_g$. In a similar approach, the DFIG-based wind turbine generators are represented by the first order dynamic equations in (4.36) and (4.40), (4.47), (4.53), (4.58), (4.62) and the pitch control in Figure 4.13. Thus, a DFIG-based wind power plant at bus j has vectors related to state variables \mathbf{x} , auxiliary variables $\mathbf{i}_{dq,j}$, bus voltage \mathbf{u}_K and inputs \mathbf{v} as defined in (5.33).

$$\begin{aligned}
\mathbf{x}_j &= [\omega_{m,j}, \psi_{d,s,j}, \psi_{q,s,j}, \psi_{d,r,j}, \psi_{q,r,j}, x_{1,j}, x_{2,j}, x_{3,j}, x_{4,j}, \dots \\
&\quad x_{5,j}, x_{6,j}, x_{7,j}, I_{d,g,j}, I_{q,g,j}, U_{DC,j}, \beta_j]^T \\
\mathbf{i}_{dq,j} &= [I_{d,j}, I_{q,j}]^T; \\
\mathbf{u}_K &= [\underline{U}_1, \underline{U}_2, \dots, \underline{U}_K]^T; \\
\mathbf{v}_j &= [T_{m,j}, U_{d,s,j}, U_{q,s,j}, U_{d,r,j}, U_{q,r,j}]^T;
\end{aligned} \tag{5.33}$$

Where n is the number of network nodes and m is the number of aggregated wind power generations. $j = 1, 2, \dots, m$. The set of differential algebraic equations in (5.32) and (5.33) represent all dynamic and algebraic equations of the synchronous generators and DFIG-based wind power plants, respectively form the system dynamic equations (DEs) for transient stability studies. Such set of DAEs is non-linear and is solved using numerical integration techniques. In this thesis, a power system simulation tool that solves the network power flow and then the time-domain simulation to solve the non-linear differential equations has been developed in the MATLAB/Simulink environment.

The time-domain dynamic simulation tool solves the set of DAEs as per the flow-chart presented in Figure 5.7. To execute the time-domain simulation, the power network solutions at steady-state have to be analyzed and the initial values of the dynamic model variables have to be calculated as discussed in section 5.5.

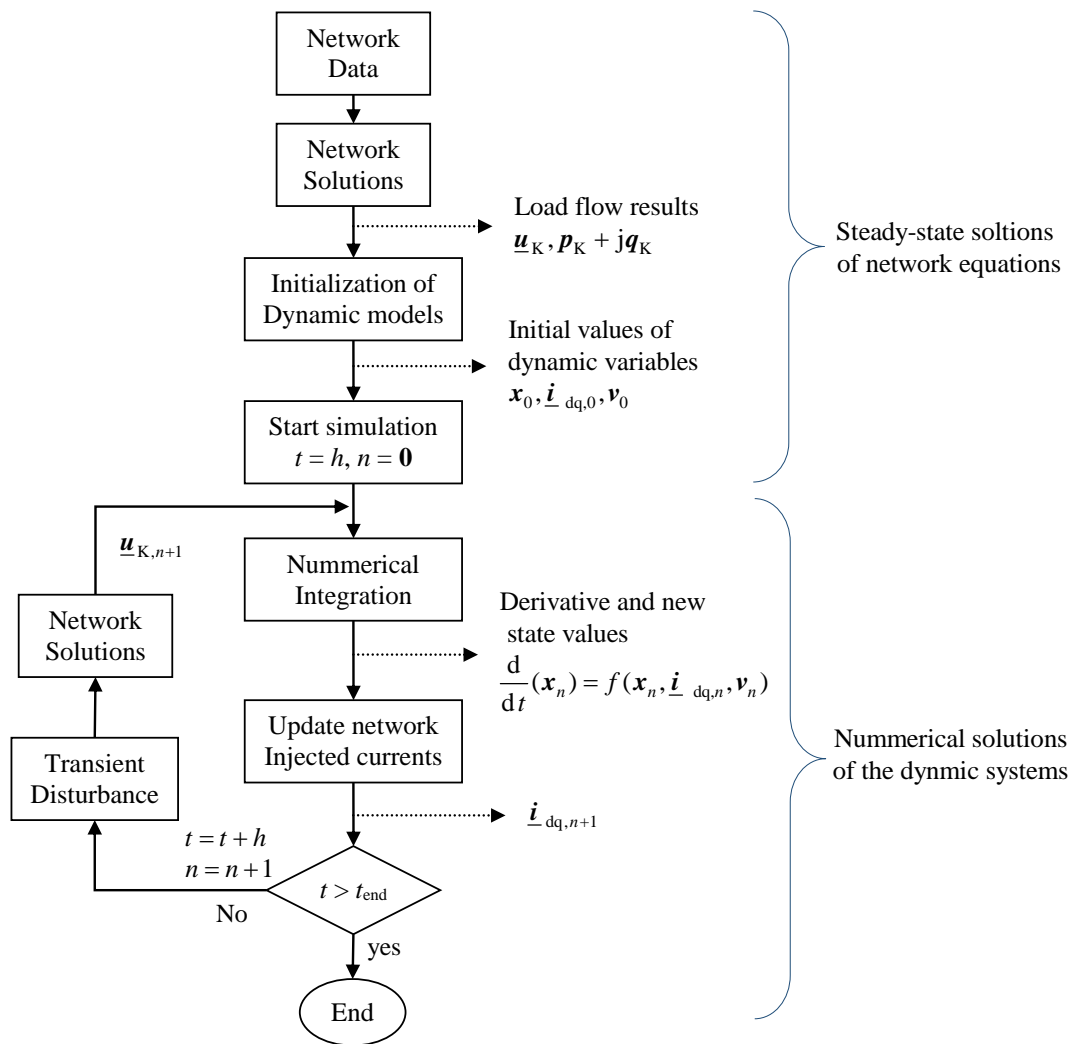


Figure 5.7 Dynamic power system simulation flow chart

The overall network integration and the approach for the time simulation analysis is demonstrated in Figure 5.8. In this schematic diagram, a synchronous generator at the i -th bus and a DFIG-based wind power plant at the j -th bus are depicted in detail with all components and their respective variables in and out of the dynamic model. The numerical simulations are solved and the network solutions are updated during the first-time step. Using the new state variables, the differential equations and algebraic equations in respective order are solved in the next time step. This continues till the end of simulation time.

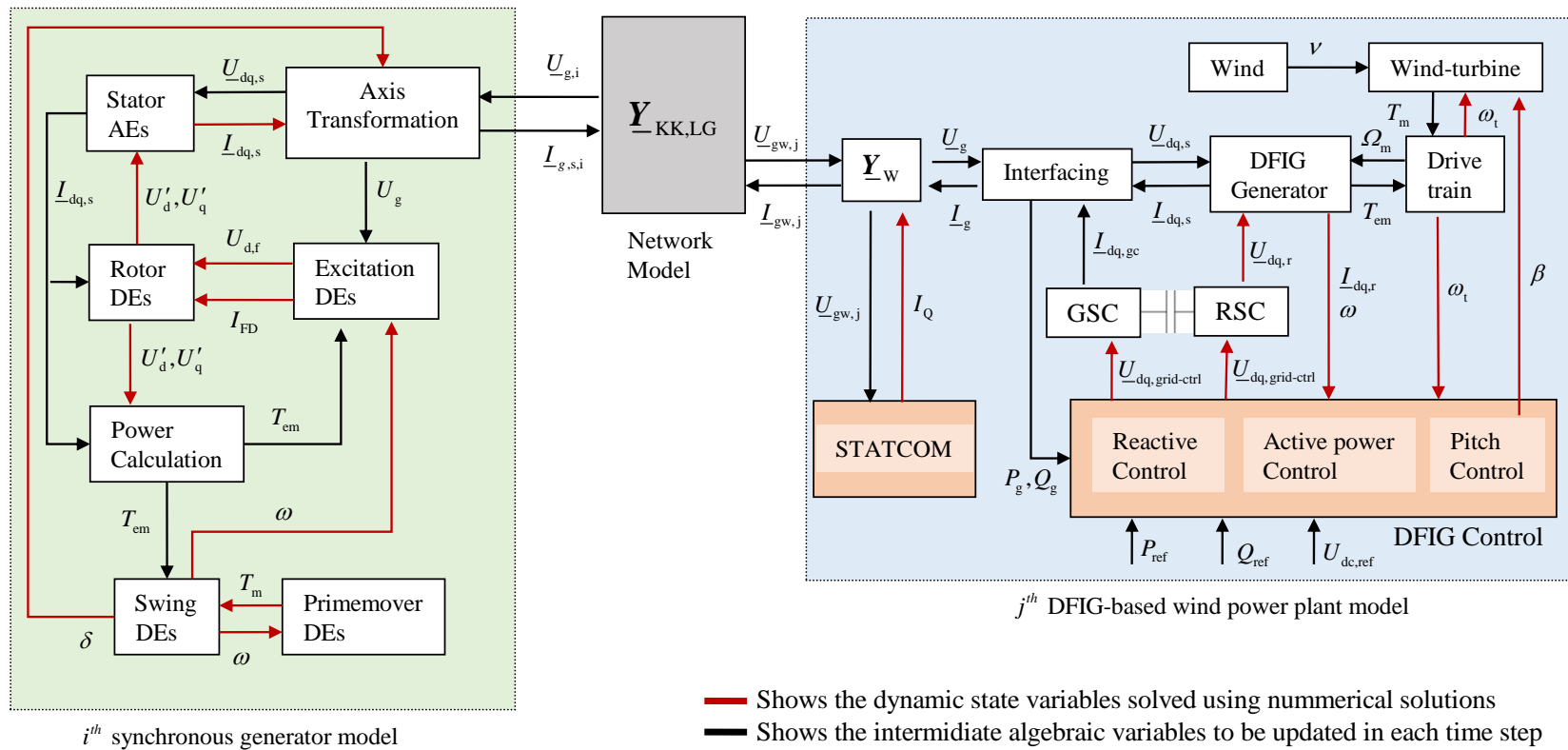


Figure 5.8 Complete schematic diagram for the multi-machine power system modeling and grid integration

6 Case Studies

In this case studies, various test systems have been considered to evaluate the analyses of power system dynamics and demonstrate what is the technical impact of increasing the wind power share on system transient stability. Moreover, the issues related to dynamic voltage stability and system frequency stability will be studied in detail for various network topologies and disturbance events.

6.1 Impacts of wind generators on transient responses

The proposed RMS model of the DFIG-based wind power plants has been applied for different power network topologies and the time-domain simulation responses are noted. In this section, three test grid systems have been considered to study the dynamic impacts and to verify the proposed measures for grid connected large-scale wind power plants.

The dynamic characteristics of the proposed model for a DFIG-based wind power plant is first evaluated through a 4-bus test grid system. The aggregated DFIG-based wind turbine model is connected to a voltage source bus so that the detailed dynamic characteristics of the proposed machine model and control strategies are examined. It is understood that this is not the most realistic depiction of a power system, but it is the simplest form of a system to explicitly illustrate the functionality of the model for studying the dynamic behaviors of frequency and voltages.

6.1.1 Analyses of the dynamic characteristics of a wind power plant connected to a voltage source

Figure 6.1 shows the 4-bus test system used in the simulation to evaluate dynamic behaviors of a wind turbine generator and its control strategies. The DFIG-based wind power plant consists of 10 units each with 1.5 MW machine rating as in Table 5.2. The wind turbines are aggregated according to the principles described in section 4.8. Thus, a total of 15 MW installed capacity of aggregated wind power plant at bus 1 and a 30 MVA synchronous generator at bus 4 are interconnected through an equivalent line and transformer based on Figure 4.15 (b). The synchronous generator represents the rest bulk power system while isolating the average frequency dynamics from other factors such as the large grid topologies and different types of controllers such as the turbine governors and voltage regulators. The parameters of the aggregated wind power plant, the equivalent

line inductance of the collecting lines X_{eq} , 20/220 kV step-up transformer, 220 kV transmission line and the synchronous generator are presented in Appendix B.

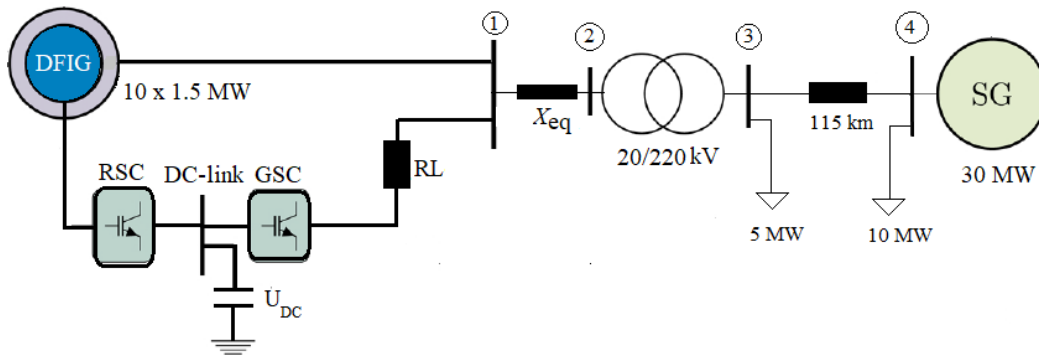
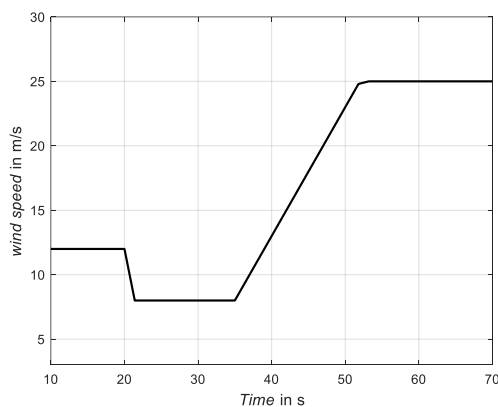
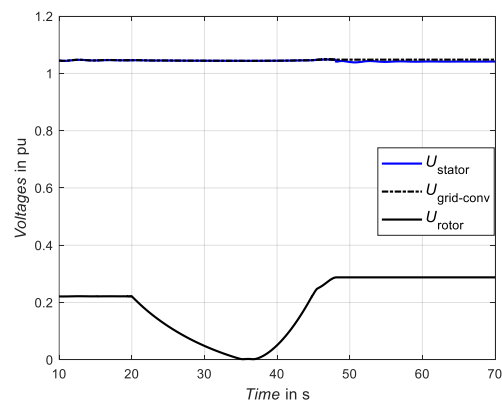


Figure 6.1 Aggregated DFIG-based wind power plant in a 4-bus test grid

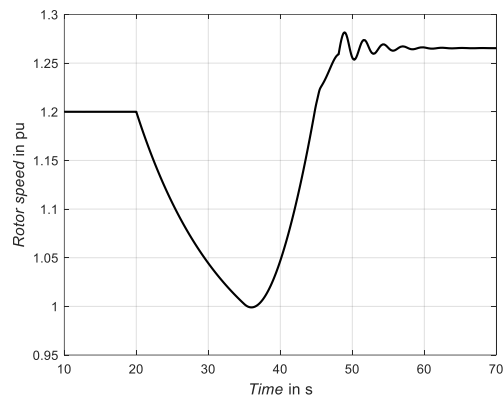
The loads at bus 3 and 4 have initially 5 MW and 10 MW, respectively at power factor of 0.95. The wind turbines are arranged to start the simulation at 12 m/s wind speed. In this regard, the wind power penetration is approximately 66.67 % of the total generation capacity. Figure 6.2 shows stator, rotor and grid-side converter outputs of the aggregated wind power plant in response to the varying wind speed (see Figure 6.2 (a)). Figure 6.2 (b) shows that stator and grid-side voltages remain constant while the rotor-side converter-controlled voltage source is varying to regulate the stator power in response to the wind speed.



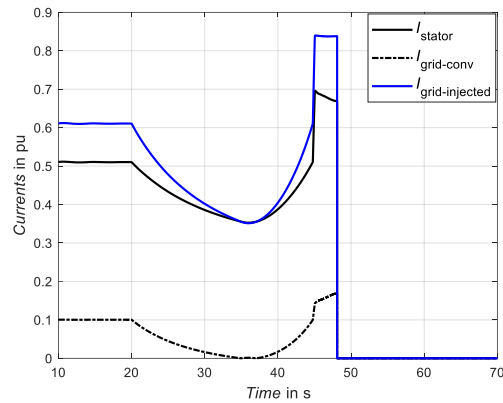
(a) Input wind speed



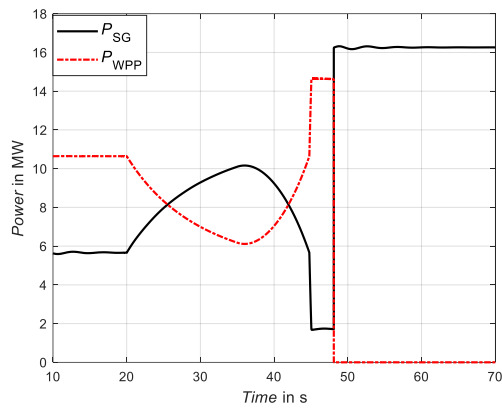
(b) Stator, grid and rotor-side converter voltages



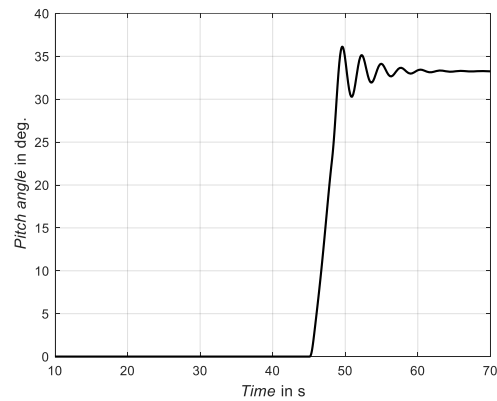
(c) Wind generator rotor speed



(d) Stator, grid-side converter and grid currents



(e) Aggregated wind power plant power

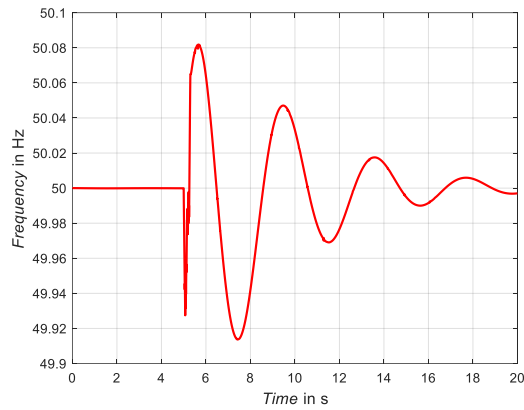


(f) Rotor pitch angle

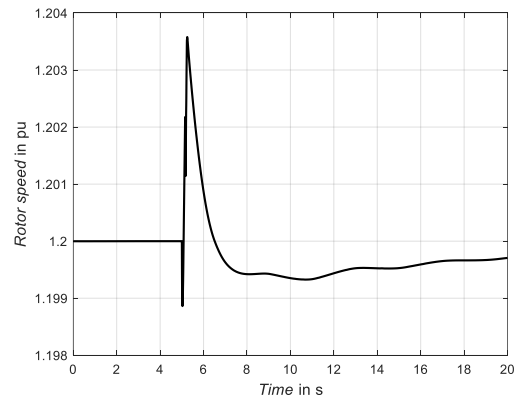
Figure 6.2 Aggregated wind power plant simulation results for varying input wind speed

The results in Figure 6.2 (b) – (f) show that the aggregated wind power plant outputs are tracking the input wind speed until the cut-out wind speed at 22 m/s and then a trip signal, with some protection response delay, is ordered to shut down the turbines so that the output power is zero at simulation time 48. These results indicate the proposed DFIG-based wind turbine model is adequate to represent its dynamic characteristics and control strategies in response to the varying input wind speed.

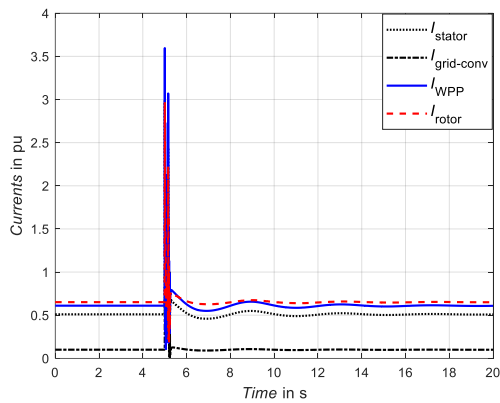
The small test grid has been also subjected to transient disturbances (three-phase fault and large load change at bus 4) to spot the dynamic responses of the wind power plant. In the first scenario, a three-phase fault is applied at bus 4 at 5.0 seconds with fault clearing time at 5.15 seconds. The wind speed is set to remain constant at 12 m/s where the generator is expected to rotate at a slip of - 0.2 (see Appendix B). Figure 6.4 shows the aggregated wind power plant (AWPP) and SG dynamic responses to the three-phase fault at bus 4.



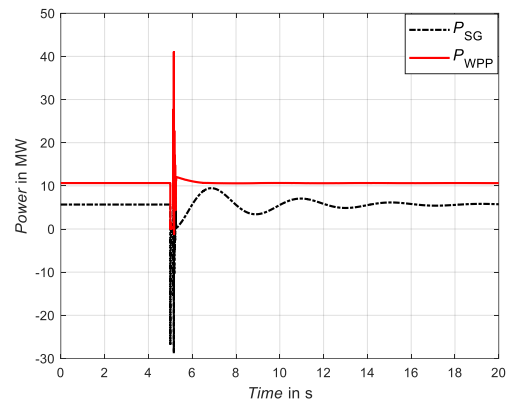
(a) Grid frequency



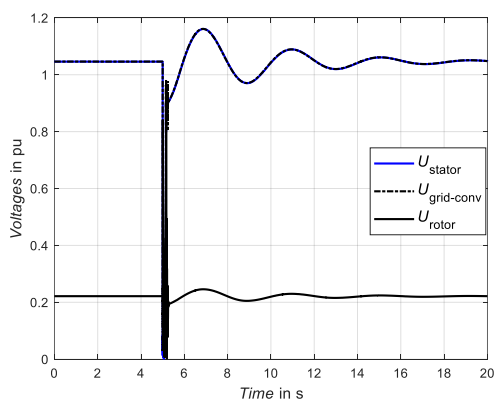
(b) AWPP rotor speed with slip = - 0.2



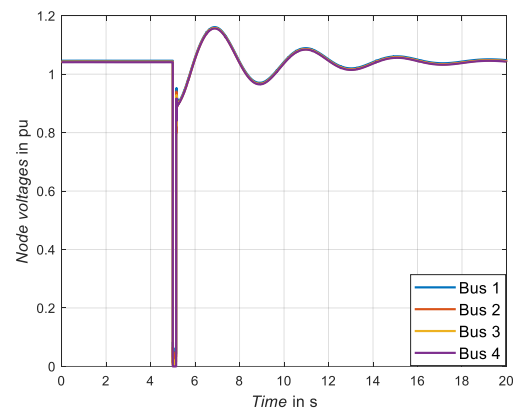
(c) AWPP current responses



(d) SG and AWPP power generations



(e) AWPP generator voltage dips

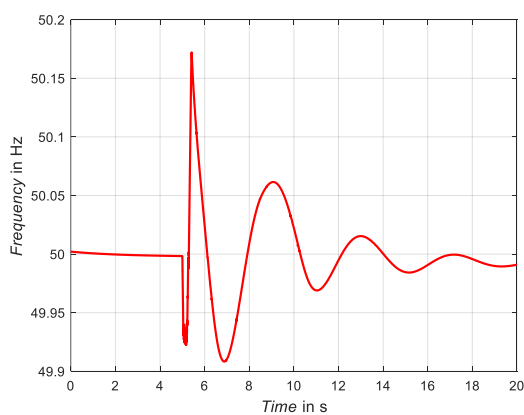


(f) Test grid bus voltage response

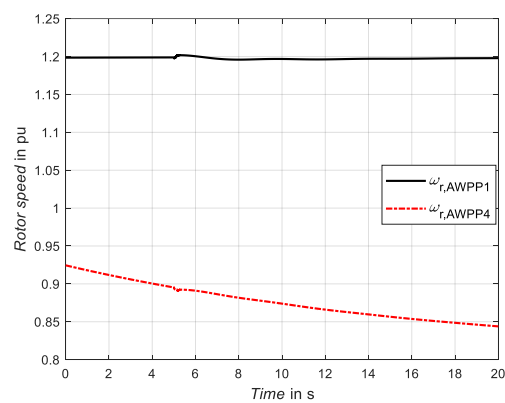
Figure 6.3 Three-phase fault transient responses of the 4-bus test grid with SG at bus 4 and AWPP at bus 1

The dynamic responses of the grid frequency in Figure 6.3 (a) have increased during the fault event. In (b), the AWPP's rotor speed, is rotating above the nominal super-synchronous speed for a wind speed of 12 m/s. The DFIG-based AWPP suffer with high in-rush current in the converter, I_{rotor} as in (c), and is injecting higher current and active power (see Figure 6.3 (d)) to the grid which can limit the safe operation of converters. This rotor over-current is caused due to voltage dips on the stator. The corresponding dynamic voltage responses of the AWPP and the test grid buses are illustrated in Figure 6.3 (e) and (f), respectively.

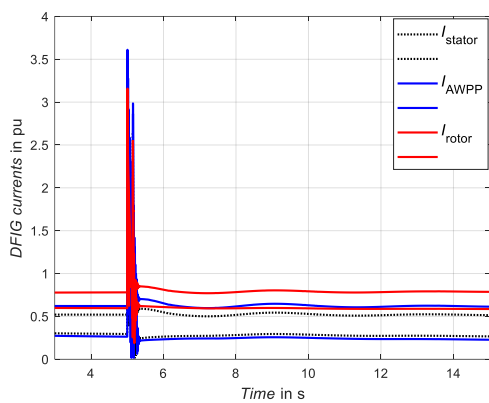
Therefore, the proposed generic model of DFIG-based wind turbines conveys the actual characteristics of a wind generator connected in a power system. However, the wind turbines are limited to regulate the grid frequency as in (a) which is a major concern when a significant amount of synchronous generator power is replaced by wind generators. To study explicitly the impacts of the increasing penetration level of wind power into the test grid, another aggregated wind power plant with total installed capacity of 15 MW is connected at bus 4, so that the synchronous generator is fully replaced by a second AWPP. With the given load condition, the total load is 15 MW at PF = 0.95 and so the total generation power shall be sufficient to supply the load. Thus, the AWPP at bus 1 is made to operate at 12 m/s wind speed (that is $P_{AWPP1} = 0.73 \times 15 \text{ MW} = 10.95 \text{ MW}$) and the second AWPP at bus 4 is made to operate at 8 m/s so that its optimal power is approximately 6 MW ($P_{AWPP1} \approx 0.4 \times 15 = 6 \text{ MW}$). Once again, a similar three-phase fault is applied at bus 4 and the impact of increasing wind power capacity on the test grid is studied and evaluated in contrast to the earlier scenario. With such arrangements, the dynamic responses of the test grid which is fully supplied from wind power plants are depicted in Figure 6.4.



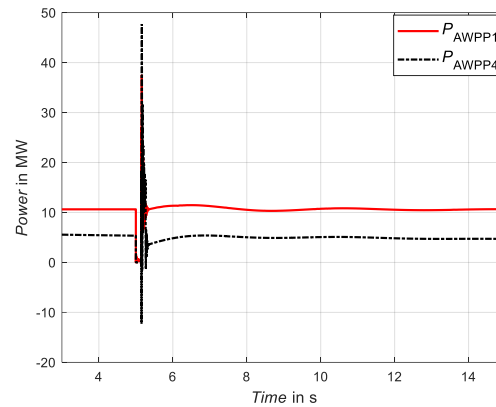
(a) Grid frequency



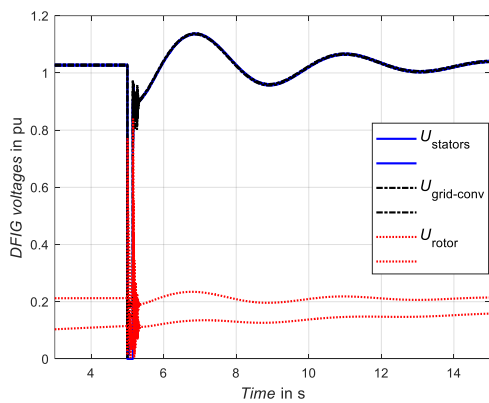
(b) AWPP rotor speed with slip of - 0.2



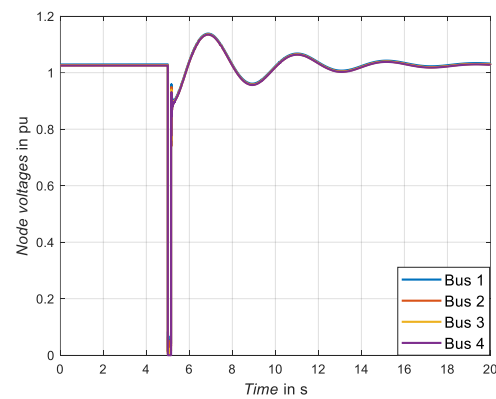
(c) AWPP current responses



(d) AWPP power at bus 1 and bus 4



(e) AWPP voltage dips



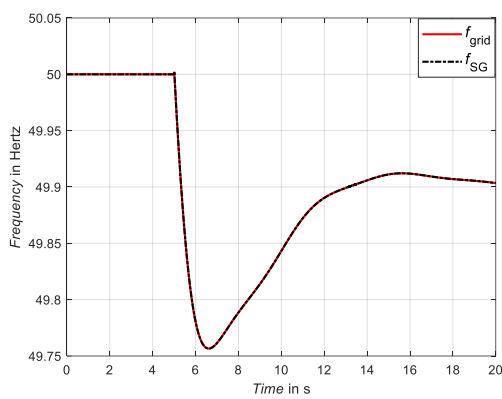
(f) Test grid bus voltage response

Figure 6.4 Three-phase fault transient responses of the 4-bus test grid with both AWPPs at bus 1 and bus 4

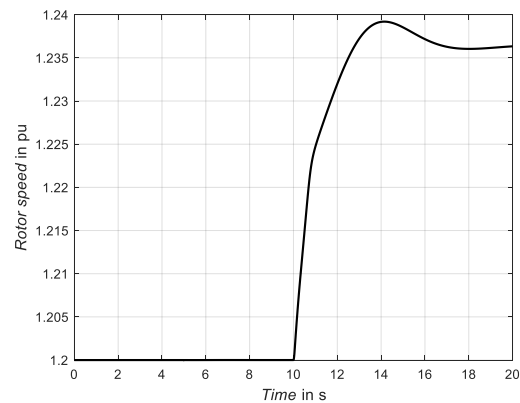
Comparing the transient responses of Figure 6.3 with Figure 6.4, it is obvious, that the grid frequency at plot (a) has a higher rate of change of frequency (ROCOF) when the penetration level is increased. Figure 6.4 (b) shows the wind generator’s rotor rotational speed for two different wind speed regimes. The output powers for both cases are kept constant so that the responses to wind capacity increase is accurately compared as shown in Figure 6.3 (d) and Figure 6.4 (d). The current results at (c) show that the latter case with higher penetration level of wind power suffer a lot with rotor over-currents during the fault event. Oscillating generator current source as in Figure 6.4 (c) has definitely an impact on the bus voltage stability so that the dynamic voltage responses in (e) show higher change of bus voltages at the generator buses. This is simply because DFIG-based wind generators are subjected to higher rotor over-currents due to the grid voltage dips unlike the synchronous generators. Some further scenarios have been carried out with

different penetration levels and the results follow in similar fashion. Thus, it can be concluded that the three-phase transient responses of the test grid are becoming worse as the wind power penetration level is increasing.

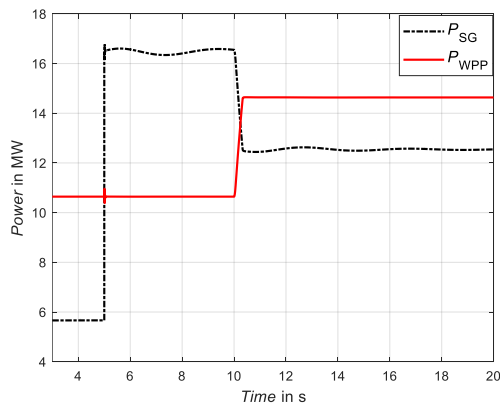
In the second scenario, the load at bus 4 is increased by 100 % at 5 seconds and remains connected until the end of the simulation. The wind speed is set to 12 m/s until the load disturbance is partially recovered at 15 seconds and then is gradually increased to 18 m/s to further study the transient responses. Figure 6.5 (a) shows the grid frequency f_{grid} , which is calculated based on the generator center of inertia as in (3.24), and synchronous generator rotor frequency f_{SG} . The results indicate similarity as the network frequency is following the SG.



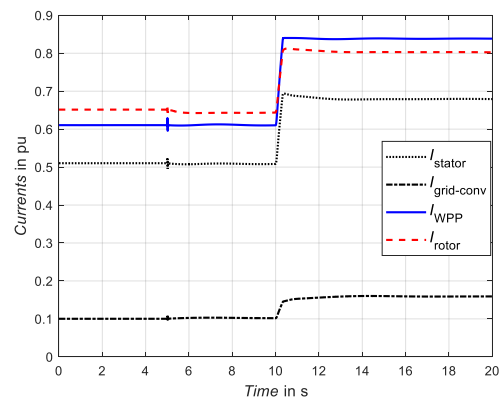
(a) Grid frequency and SG rotor frequency



(b) Aggregated WTGs rotor speed



(c) SG and wind power plant power outputs



(d) Aggregated WTG currents

Figure 6.5 Test grid simulation in response to large load change at bus 4 and varying input wind speeds from 12 m/s to 18 m/s

The rotor speed of the DFIG-based wind generator in Figure 6.5 (b) is in super-synchronous operation that allows the generators to generate power from both the stator and rotor-sides. This proves the fact that WTGs are designed to operate in the super-synchronous

mode during high wind speeds. This can be observed from the generators output power and current plots in Figure 6.5 (c) and (d), respectively. Figure 6.5 (c) shows that the SG has solely accommodated the load change while the power from the WTGs is first oscillating due to the load disturbance but shortly settled down to its maximum power point at 12 m/s as it cannot generate more than it. When the wind speed is increasing, the power from the AWPP is rising while replacing the synchronous generator power until the maximum power point corresponding to 18 m/s is attained.

6.1.2 Transient response analyses of the New England test system

The second test network, considered in the case study, is the New England network, shown in Figure 6.6. In this thesis work, the test network is mainly used to investigate the impacts of increasing wind power share on power system dynamics. The dynamic responses of different scenarios are evaluated through which the voltage and frequency stability margins with various penetration levels of wind power are studied. The main reason to employ this test network is due to its size and data availability as it is widely used in various transient analyses so that the results can also be compared easily to previous similar studies. Moreover, since the dynamic parameters of the synchronous generators and their regulators are relatively tested and amended in previous literatures, the network can be considered as testified topology.

In this thesis, the New England test network is mainly used to accurately study the impacts of increasing penetration levels of wind power capacity on the dynamic voltage stability margins as large network topology. The New England system has initially 10-synchronous generators whose detailed data are given in Appendix C. The impact of wind generators on the network is realized by increasing the share of wind power where the existing SGs are replaced by wind generators. The synchronous generators at bus 30, 32 and 35 are replaced by aggregated wind turbines to study the dynamic responses of various transient disturbances.

The impact of wind power increase on the network dynamics is carried out in three scenarios. The controlled conventional generators are step by step replaced by uncontrolled wind generators while investigating the system dynamics in each case. The main target of this analysis is to examine the impacts of increasing the wind power share on the power system dynamic behaviors such as grid frequency response, rotor angle responses and voltage collapse. Hence, the input wind speed of 12 m/s and the active power dynamics are relatively apprehended at constant values to keep the transient response as generic as possible.

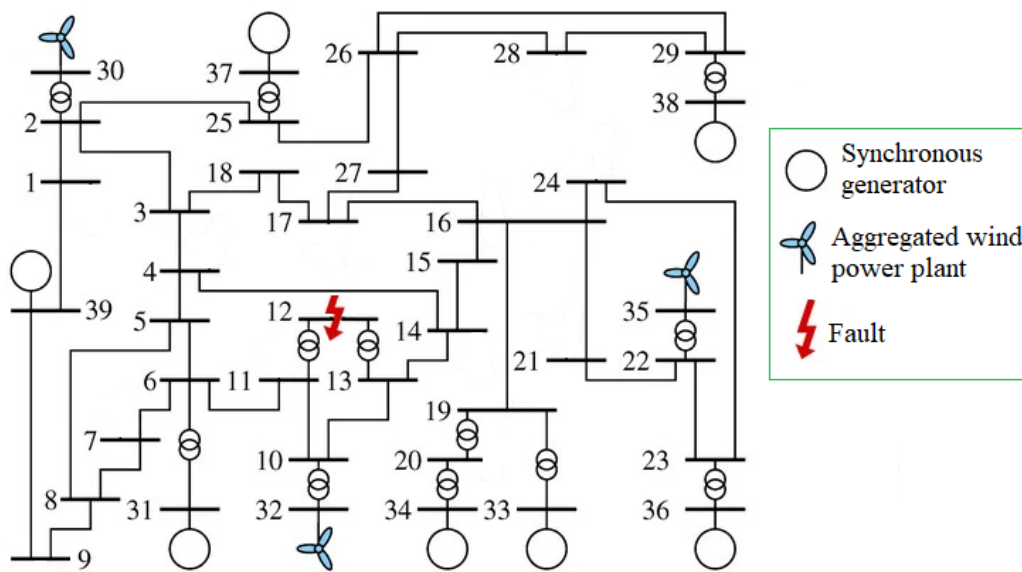


Figure 6.6 New England IEEE 39-bus system with three synchronous generators replaced by wind generators and three-phase fault at bus 12 [66]

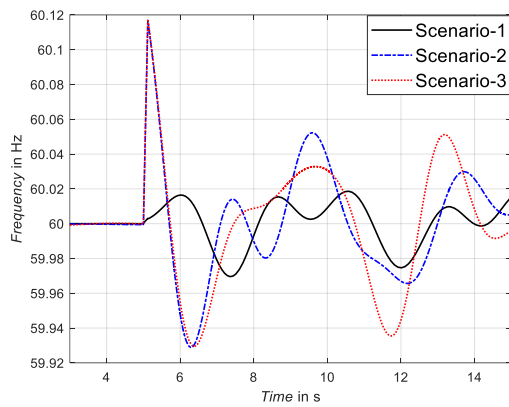
The load flow solutions for the New England test system yield the generator set voltage profiles in steady-state case, total power generation of 5.899 GW and a total system load of 5.880 GW as in Appendix C Table A.9. The PTSI indices of the New England test network, using (5.21), at base load shows that all load buses are within the allowable operation limits [57]. Based on the static loading, bus 12 is found critical [57]. This steady-state condition has been an input to the transient simulations. Thus, different network disturbances are applied at bus 12 to observe the worst situations. In this study, particularly, the dynamic voltage stability analyses are carried out with a load change at this bus while the others are kept constant at their base loads. The nearest generation station to the critical bus is bus 32. The impact of increasing wind power has been studied in three scenarios where the synchronous generators at buses 30, 32 and 35 are step by step replaced by aggregated DFIG-based wind power generators.

- **Scenario-1** all power generators are synchronous generators (thermal plants)
- **Scenario-2** aggregated DFIG-based wind generators at bus 30 and bus 35 (which is about 27 % penetration level of wind power)
- **Scenario-3** aggregated DFIG-based wind generators at bus 30, bus 32 and bus 35 (which is about 40 % penetration level of wind power)

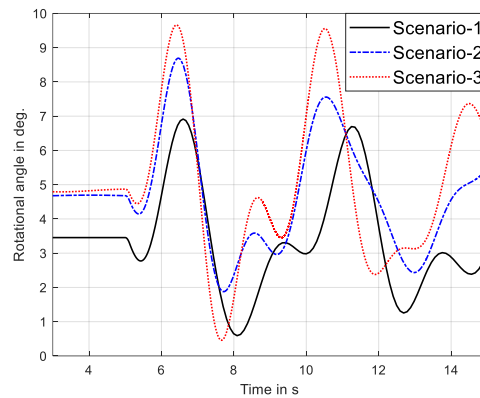
The intention on this section, with these three scenarios, is to investigate the influence of increasing wind power on power system dynamics within stable operation of different network topologies. In the proceeding sections, the penetration level of wind capacity is

increased to up to 100 % by modeling the DFIG-based wind power plants with enhanced control strategies.

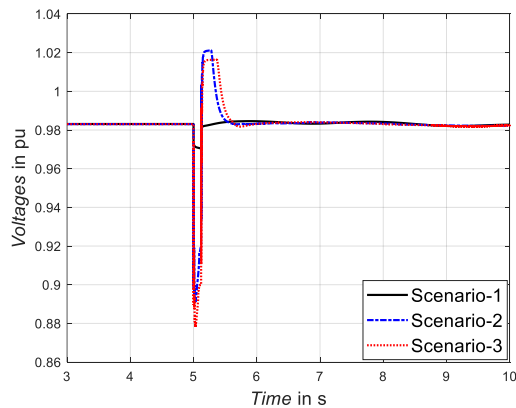
A three-phase short circuit, which lasts for 100 milliseconds, is applied at a critical bus (bus 12) for the three scenarios. The time simulation results confirm that the generator at bus 32 is significantly affected by the transient disturbance compared to the others. Hence, the generator at bus 32 is found utmost suitable to reveal the impacts of increasing wind capacity penetration level on the system stability. Figure 6.7 shows the New England test network dynamic responses for the three-phase fault at the critical bus. In this case, the synchronous generators are employed with steam turbines as in steam thermal power plants.



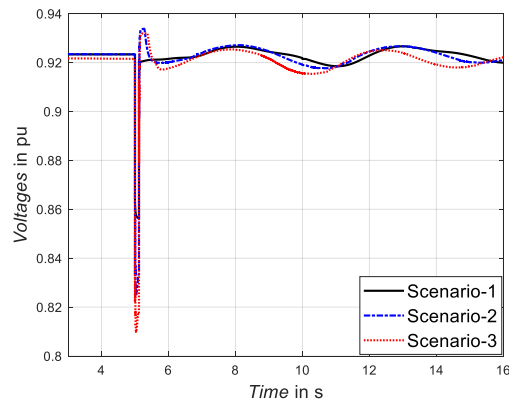
(a) Frequency responses at bus 32



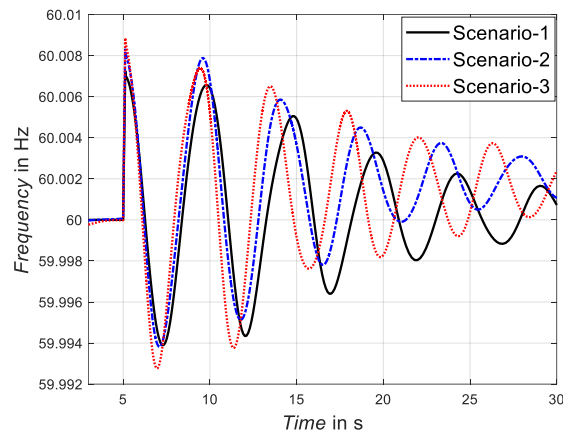
(b) Rotor angle responses at bus 31



(c) Voltage dip at bus 32



(d) Voltage at critical bus



(e) Grid frequency responses

Figure 6.7 Impacts of wind power increase on frequency and voltage responses to three-phase fault at critical bus

Figure 6.7 (a) shows the terminal field frequency, i.e., the stator voltage frequency of the generator at bus 32 for the three scenarios. The SG in bus 32 has been replaced by a wind generator in the third scenario and comparing the rotor angle responses for the three cases at this bus is meaningless. Hence, Figure 6.7 (b) presents the rotor angle response of a synchronous generator at bus 31, which is physically close to the faulty bus. This confirms that the rotor angle of the SG at bus 31 is significantly affected when the nearby generator at bus 32 is replaced by a wind power plant. The results in Figure 6.7 (a) and (b) show that an increase in wind power is disturbing the stator field frequency and the rotational angle of the generators at bus 32 and bus 31, respectively. The rate of fluctuations of the stator field frequency at bus 32 and rotor angle of SG at bus 31 are increasing with increasing wind capacity in the system.

The terminal voltage magnitude at bus 32 and at the critical bus 12 are also suffering from higher voltage dips when the share of wind power in the system is increasing as in Figure 6.7 (c) and (d), respectively. The grid frequency response at Figure 6.7 (e) presents that the rate of change of frequency (ROCOF) is higher when the penetration level of wind generators is increasing in the system.

The time-domain simulation is extended to a steady load increase at the critical bus to evaluate the distance of the dynamic voltage collapse from the steady-state operation. The P-U curves and the PTSI are calculated from the time-domain simulation results of the three scenarios to observe the impact of wind power on the dynamic voltage collapse.

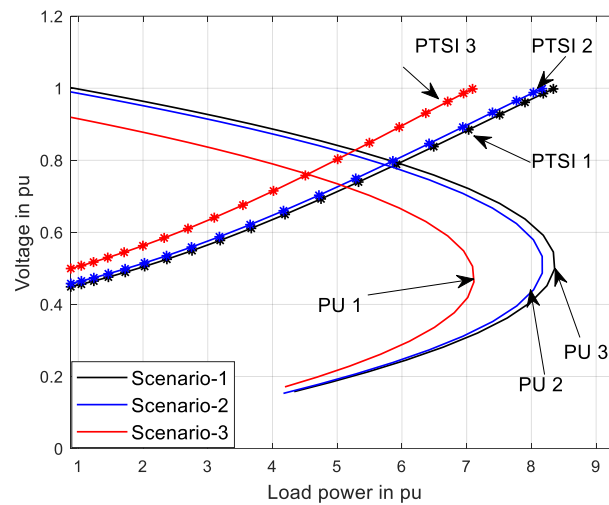
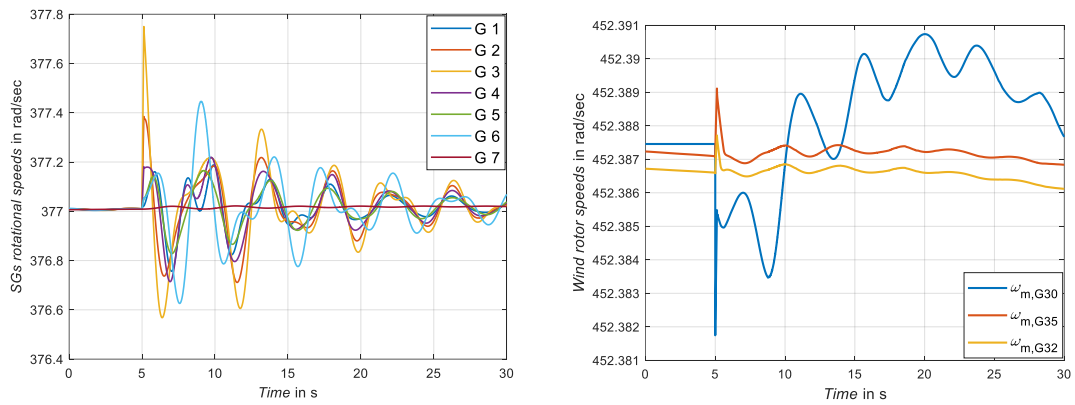


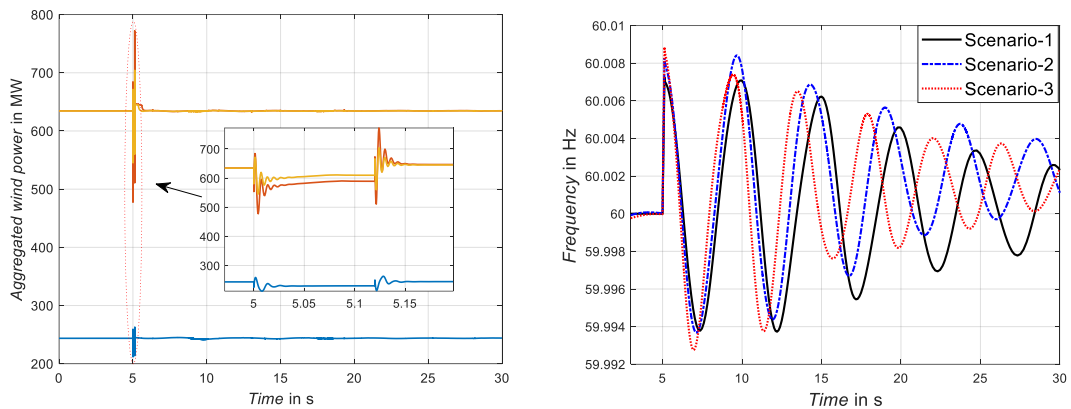
Figure 6.8 P-U curves and corresponding stability indices at the critical bus for the three scenarios

The dynamic voltage stability margin is estimated based on the P-U curve corresponding to the PTSI value at base load and the index value just before the voltage collapse occurs. Figure 6.8 presents the P-U curves of the three scenarios to predict the dynamic voltage stability margin (DVS) and the maximum transfer power at the critical bus. This shows that the dynamic stability margin is radically decreased when the penetration level of wind power increases.

Hydro power plants are also included in the analyses with various types of transient disturbances and fault clearing time to abundantly comprehend the impacts of wind power in various network topologies. It is observed, that such disturbances lead to system instability when the clearing time and the wind power penetration level are increasing. Therefore, the network dynamic responses for hydropower power plants (hydro-dominant network) with different penetration levels and fault clearing time are presented in Figure 6.9. Figure 6.9 (a) shows a transient stable response of hydro and wind generators rotational speeds and grid frequency response for a three-phase transient disturbance at the critical bus time step of 5 seconds with fault clearing time of 120 milliseconds.



(a) SGs rotational speed of scenario-3 (b) Aggregated WTG rotor speed of scenario-3



(c) WTG power response of scenario-3 (d) Grid frequency of the three scenarios

Figure 6.9 Stable transient responses of three-phase fault with hydro-generators

The rotor speeds of the conventional generators (hydro turbine) remain stable at synchronous speed during and after the fault event as in Figure 6.9 (a). For constant 12 m/s wind speed, the DFIG-based wind generator rotor speeds remain almost near to the super-synchronous rotor speed at 1.2 per unit, i.e., at a slip of -0.2 as in (b). Moreover, Figure 6.9 (c) confirms that the aggregated wind turbines are generating constant power (set by the load flow solution) with optimal power point tracking before and after the disturbance. However, the DFIG-based wind generators show an inertial response against the change in the grid.

It can be observed from Figure 6.9 (d) that hydro-generators are exceedingly affected by the increase in wind capacity compared to the thermal power plants in Figure 6.7 (e). As one of the objectives of this thesis is to investigate impacts of wind power in hydro-dominant systems like the Ethiopian power system, the conventional generators in the proceeding time-domain simulations are represented as hydro-turbine types.

Figure 6.10 presents the dynamic responses of the grid frequency and dynamic voltage of the critical bus in response to large load and input wind speed changes. The load at bus 20 is increased suddenly by 50 % at time 5.0 seconds, i.e., from 628 MVA to 942 MVA. The wind speed at bus 32 is changed from 12 m/s to 15 m/s at time 40 seconds while the wind power plants at bus 30 and bus 35 remain at wind speed of 12 m/s.

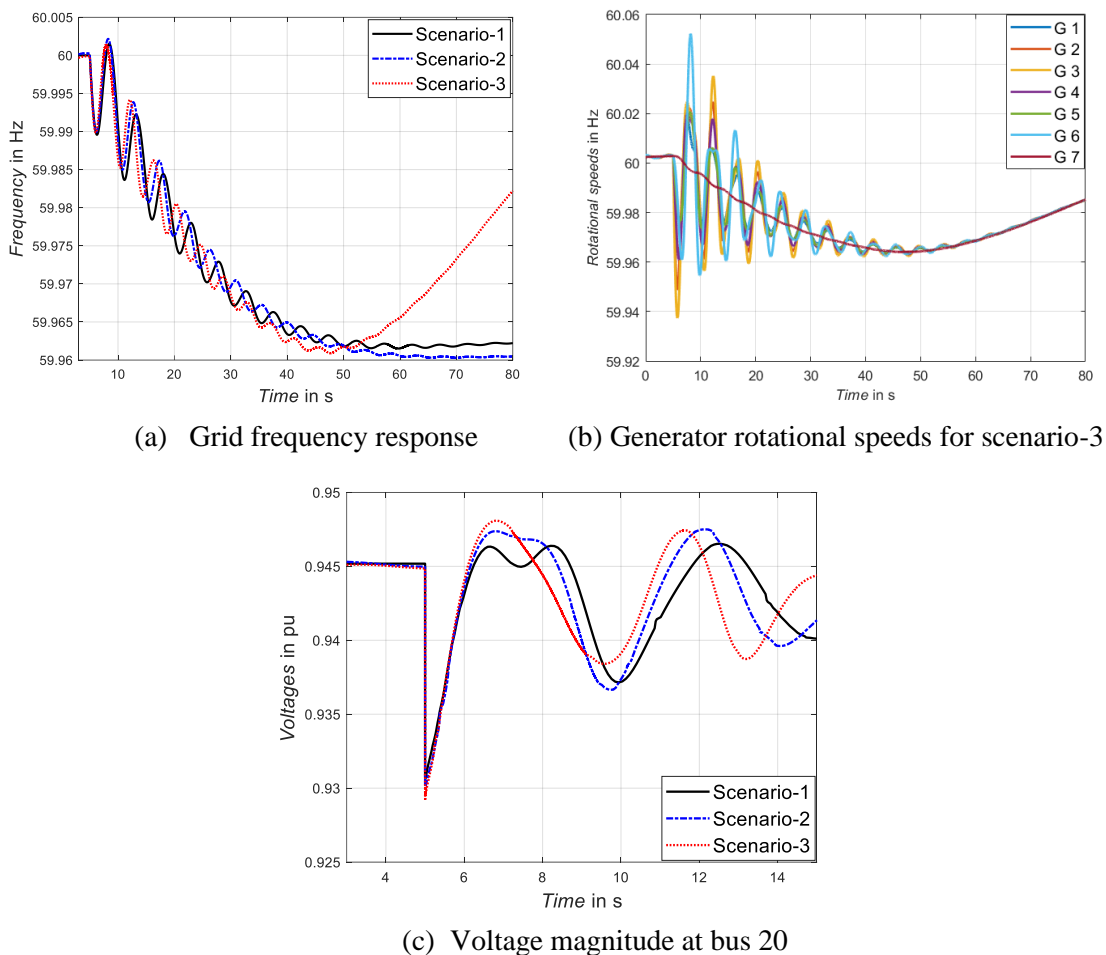


Figure 6.10 Stable transient responses of load change at bus 20 with hydro-generators

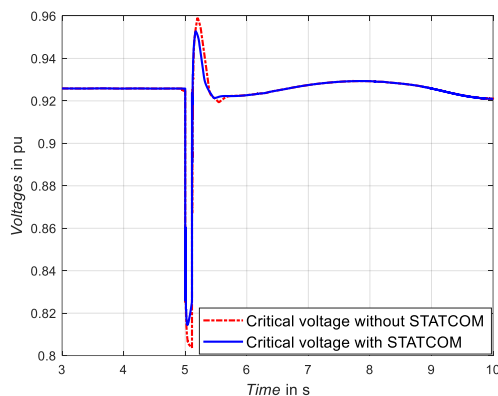
Figure 6.10 (a) shows that the grid frequency is dropping first and then recovering due to an increase in wind speed at bus 32 which helps to generate its nominal power at 15 m/s. The AWPP at bus 32 generates 650 MW till 40 seconds where the grid frequency is below the other scenarios but after time step 40 (when the wind input is increased), the wind generator is increasing its output and is helping in alleviating the grid frequency drop. Hence, this verifies that the aggregated wind power model is responding to the grid frequency suppression if there is an increase in wind speed. The grid frequency is improving much better in scenario 3 because the aggregated wind generators at bus 32 have got a chance to increase the output power due to wind speed increase. Figure 6.10 (b) shows

that the rotor speeds of the conventional generators are also enhanced with the wind speed increase in the wind plant at bus 32. Therefore, with higher wind power share, the grid frequency can be enhanced if the wind speed is increased as shown in Figure 6.10 (b) or if there is enough spinning reserve or storage systems in the network. However, the dynamic voltage response in Figure 6.10 (c) attests that increase in wind power penetration level down surge the stator voltage dip although the wind speed is increasing and output power is increasing.

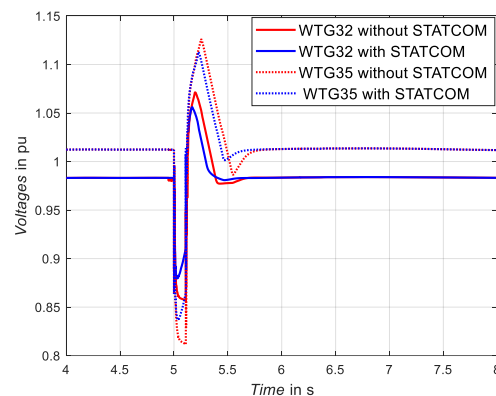
6.2 Voltage dip enhancement using STATCOM

Operation of power systems at conditions close to stability boundaries has increased the importance of fast acting reactive power compensation using FACTS devices. As stated in section 4.7, a simplified controlled current source STATCOM type, shown in Figure 4.14, is considered, to compensate the dynamic reactive power deficiency at the terminal bus of an aggregated wind power plant.

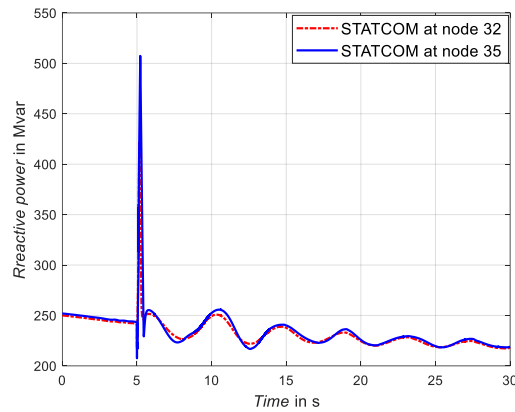
To demonstrate the functionality of the current controlled STATCOM model, the third scenario with aggregated wind generators at buses 30, 32 and 35 is considered. A controlled source current STATCOM that injects reactive current at real-time is integrated with the aggregated wind power plants at bus 32 and bus 35. A three-phase short circuit is applied at bus 20 with clearing time of 110 milliseconds and 125 milliseconds. Figure 6.11 shows the voltage dip responses of the critical bus and aggregated DFIG-based wind generators at buses 32 and 35 with and without STATCOM during the fault event in (a) and (b), respectively. The red color plots show, how the voltage response is affected, if STATCOM is not activated during the fault events. Therefore, it can be concluded that the proposed STATCOM, with real-time reactive power compensation capability, enhances the dynamic voltage responses during and after a fault event.



(a) Voltage response at critical bus



(b) Voltage dip responses at wind generators



(c) Injected reactive power at real-time

Figure 6.11 Stable voltage responses with and without STATCOM during fault event at bus 20

Figure 6.11 (c) presents the real-time injected reactive power from the current source STATCOM at buses 32 and 35. In this case, the reactive power references of all wind turbine generators is set equal to zero. Thus, the reactive power demand even after the fault at the buses is supplied by the STATCOM.

To observe the impact of the STATCOM, the fault clearing time is extended to 120 milliseconds and the corresponding transient responses of the New England test network, without the STATCOM case, are presented in Figure 6.12. The simulation results in Figure 6.12 (a) and (b) illustrate that the test network bus voltages, specifically that of the AWPP buses, are highly disturbed, if the DFIG-based wind power plants are not supported by STATCOM. The active power generation responses to the three-phase fault for the aggregated wind power plants (AWPP) and synchronous generators (hydropower in this case) are presented in Figure 6.12 (c) and (d), respectively. These results confirm that the aggregated wind power plant at bus 32 is tripped due to the higher voltage dip at its terminal bus. The trip order is initiated by the protection system to protect the in-rush current through the power-electronics in the rotor-side of the DFIG. The under-voltage protection is set at 0.55 per unit for a duration of 0.3 seconds. It is also shown in (d), that the hydropower plant at bus 39 is increasing its power to compensate the wind generator outage at bus 32.

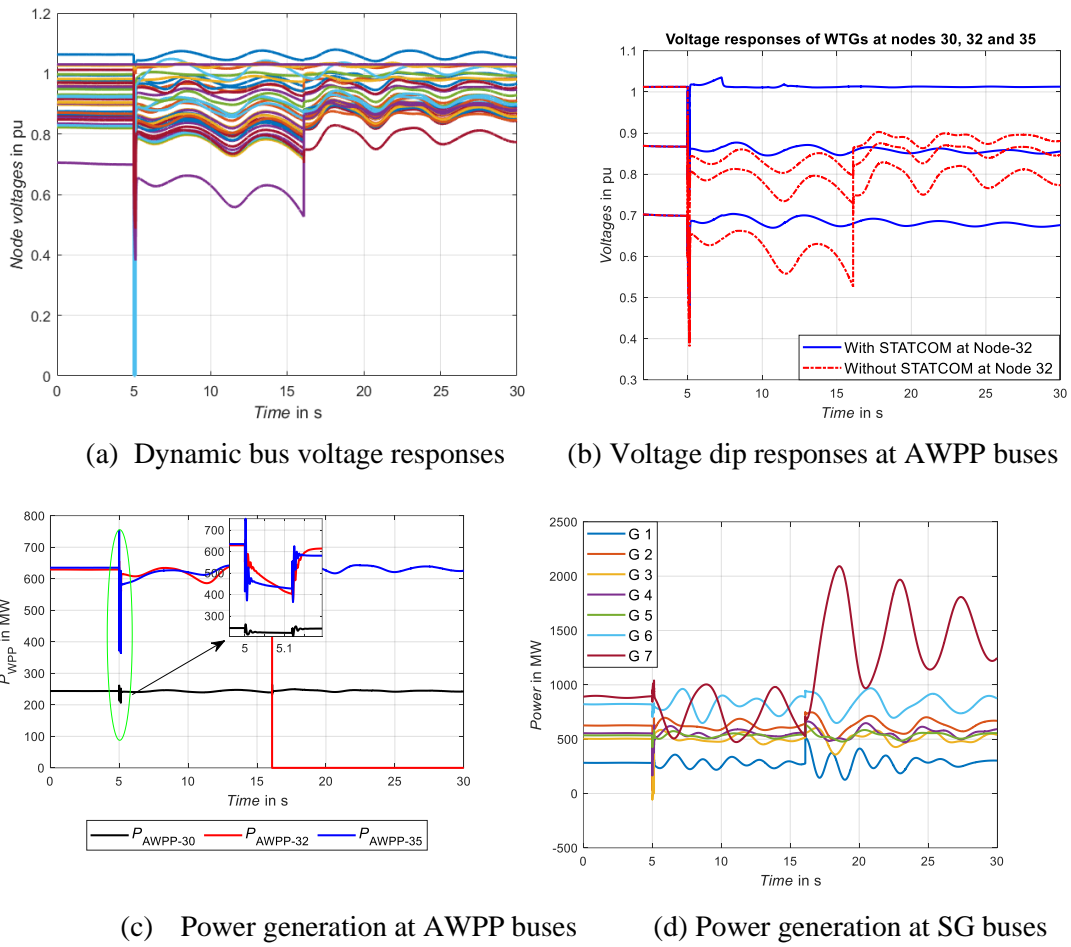


Figure 6.12 Transient responses to a three-phase fault at bus 20 with fault clearing time of 120 ms without STATCOM

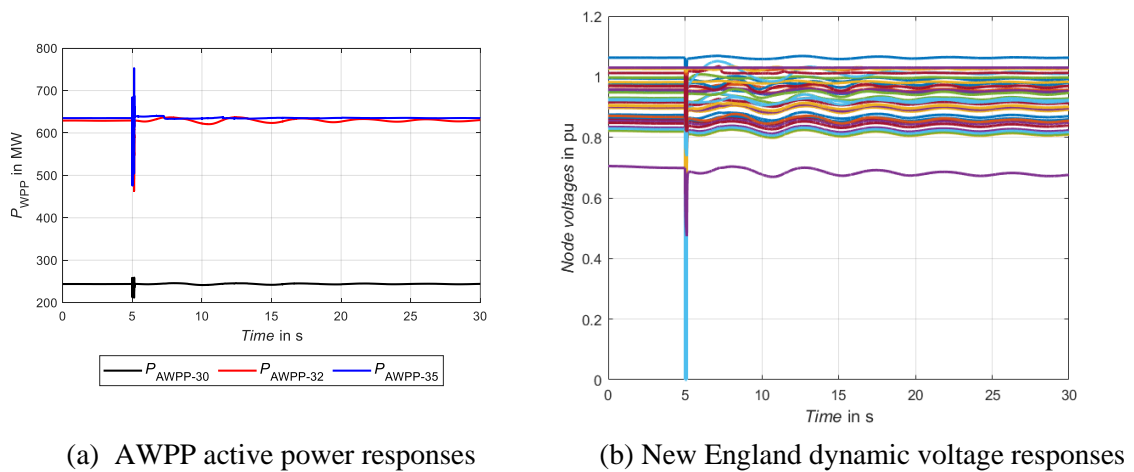


Figure 6.13 Transient responses to a three-phase fault at bus 20 with fault clearing time of 120 ms with STATCOM

If the STATCOMs at bus 32 and bus 35 are connected, the transient stability is better and is illustrated in Figure 6.13. In this regard, the wind generators are generating at their optimal operation point, that corresponds to wind speeds of 12 m/s. The voltage dip is instantly compensated by the injected reactive power of the STATCOMs. The New England test network is observed to be unstable if the fault clearing time is more than 120 milliseconds.

6.2.1 Fault ride-through capability enhancement using the rotor over-speeding control strategy

Low voltage phenomena are generally occurring when a power grid is subjected to transient disturbance such as short-circuit fault or sudden large load change. As a result, the grid voltage dip at the DFIG point of connection (POC in Figure 4.15) leads to undesirable transients in the stator and rotor circuits. The low voltage condition also limits the active power transmission from wind generators to the grid which results in power imbalance between the turbine maximum power point (MPP) operation and the grid-side, leading to significant increase of fluctuations in currents, voltages and rotational speed in the DFIG system.

A voltage dip in the stator of the DFIG results in rotor over-currents. Thus, in order to ride through the fault and protect the partial power converter, the DFIG system shall employ either a mechanism to instantaneously reduce the rotor circuit over-current or damp the excessive power by temporary circuit like the crowbar application. In this paper, the over-current is reduced by enhancing the voltage dip using a modified STATCOM at the POC and by provisionally over-speeding the rotational speed so that the wind turbine operates at output power lower than the MPP, which is named as de-loading operation.

The STATCOM is simply modeled to regulate the voltage deviation U_g at the POC for RMS type as shown in Figure 4.14. However, the power electronics in DFIG rotor-side are highly sensitive to rotor over-currents so that an immediate protection scheme must be applied as the STATCOM is not fast enough to protect the voltage dip consequences. For this reason, the rotational speed of the rotor is made to over-speeding so as the turbine is regulated to operate at lower mechanical torque T_m than the MPP. With such turbine de-loading operation, the torque imbalance between T_m and T_{em} , in (4.40) is stored as kinetic energy instead of dissipating like what is being done in the crowbar application. By over-speeding, the turbine accumulates the kinetic energy which can be released when the voltage dip is recovered. The increase of rotor speed is achieved by proper control of the rotor-side converter through supplementary power to adjust the voltage dip as shown in Figure 6.14. The control scheme is made to respond to the voltage dip with higher gain

K_d . The supplementary active power, controlled by the voltage dip magnitude, is subtracted from the optimal turbine power so that the reference active power is momentarily reduced.

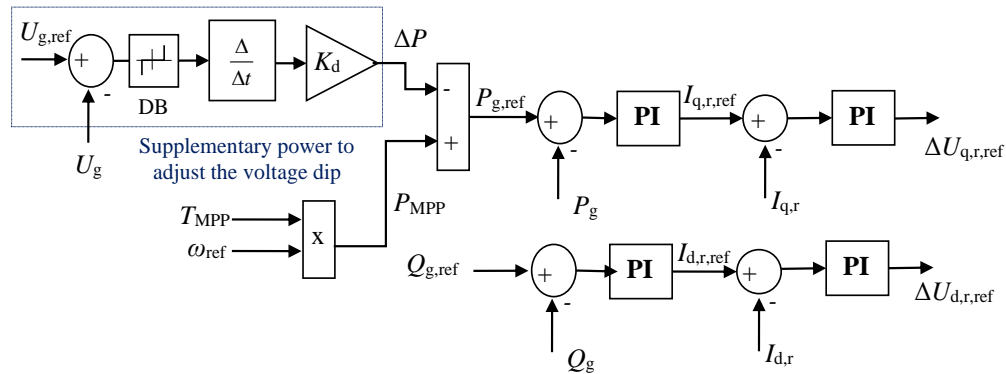
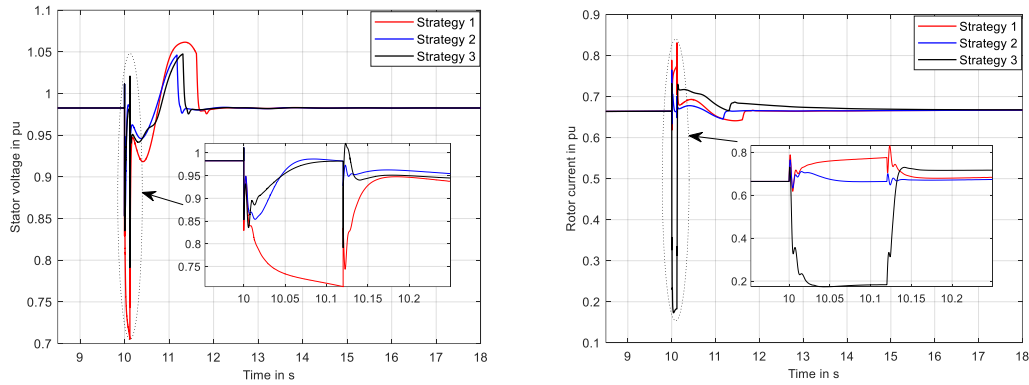


Figure 6.14 Rotor-side converter active and reactive power control with rotor over-speeding strategy in response to voltage dips

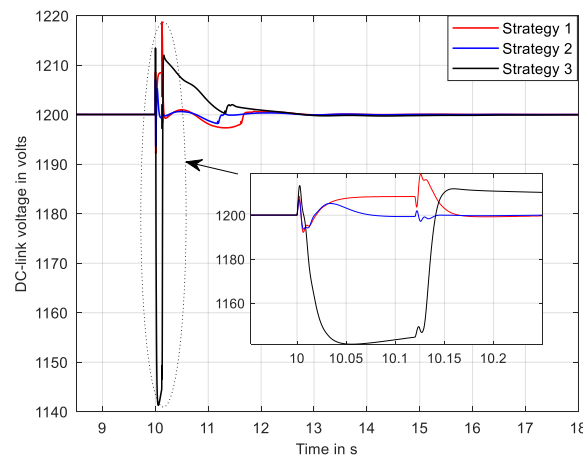
When the reference power of the rotor-side converter is set to a lower value than the optimal power P_{MPP} , the rotational speed is gradually increasing. In this thesis work, the reference active power is regulated by the voltage dip magnitude with a dead band DB of $\pm 10\%$. The rotor-side converter active power control is modified during higher voltage dip conditions, as in Figure 6.14, from the conventional DFIG-control methods in subsection 4.6.1. In this regard, the active power control method is modified in such a way that the reference power is dramatically reduced so that the speed increases and the rotor-side converter current decrease. The impact of reducing the rotor current results in higher fluctuation of the DC link voltage. Hence, the grid-side converter is made to compensate such fluctuation and keep the DC-link transients within the protection limit. With these arrangements, the DFIG-based wind turbine improves its low voltage ride through (LVRT) capability and ultimately contributes to support grid transient stabilities.

The proposed LVRT enhancement scheme is tested in the IEEE 39-bus test system using the third scenario in section 6.2.2, i.e., 40% penetration level of wind power. To evaluate the proposed scheme, three strategies have been adopted in response to the short-circuit fault at bus 20 for duration of 120 milliseconds. Bus 20 is physically close to the critical bus (bus 12) and wind generator at bus 32. For this reason, the dynamic responses of wind generator at bus 32 are considered and studied in detail below. The *first strategy* is with conventional (vector) DFIG-control schemes that is active and reactive power are regulated by rotor-side converter targeting to operate at optimal or maximum power point while the grid-side converter regulates the DC-link voltage. The *second strategy* is with optimal operation while the voltage dip at the stator is compensated with STATCOM.

The third strategy is with over-speed capability of the rotor-side converter control strategy in line with the STATCOM application to sustain the long-term voltage stability issues.



(a) Voltage dip response at WTG bus 32 (b) Rotor current responses at WTG bus 32



(c) BTB converter DC-link voltage responses at WTG bus 32

Figure 6.15 Improved LVRT capability of DFIG transient responses to symmetrical fault at bus 20

Figure 6.15 (a) shows that the voltage dip is higher for the conventional DFIG control strategy without both the STATCOM and rotor over-speed capability, while the response in the third strategy, where the STATCOM and over-speeding capability are employed, shows an improved voltage dip. Implementing the third strategy, leads to reduced rotor over-current during voltage dips as in Figure 6.15 (b). Figure 6.15 (c) also presents the partial load back-to-back converter DC-link voltage fluctuation due to the voltage dip. The results in (b) and (c) reveal that the proposed joint control strategy, STATCOM and over-speeding scheme, have improved the LVRT capability by reducing the rotor over-currents and DC-link fluctuations.

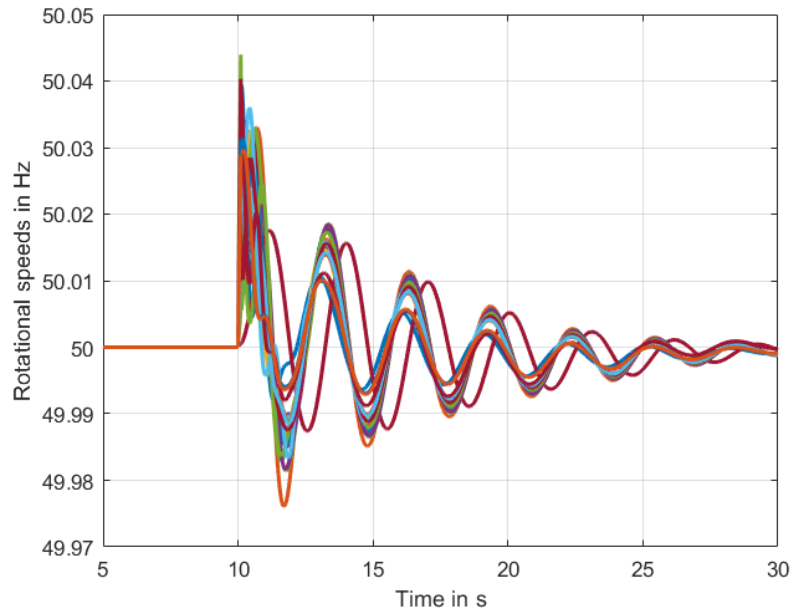
6.3 Transient responses for the case of the Ethiopian power system

In this thesis work, the Ethiopian network is considered as a case study for weak power systems. The Ethiopian network has a low share of wind capacity comparing to the second and third scenarios of the 39-bus system. The transient analysis in this case is intended to demonstrate that increasing wind power has a significant impact on weak power systems. The case study includes both the existing grid-connected generations and transmission systems until 2020 and also the units scheduled for the year 2022 based on the EEP master plan [9]. Hence, the case study considers the network model for the year 2022. The steady-state network data are taken from the EEP power system planning office for the year 2022. The cases study network has a total active power generation of 4.082 GW and a total load of 3.586 GW with an average load power factor of 0.971. The base network model in the simulation includes 770 buses, 45 conventional generation units, 5 wind power plants, 302 load buses, 376 transmission lines and 684 two-winding transformers. The three winding transformers are converted to three two-winding transformers and the two-winding T-model of the transformer is applied as discussed in subsection 3.2.2. The network data is not public and therefore a summary of the data used for the dynamic simulation are given in Appendix D.

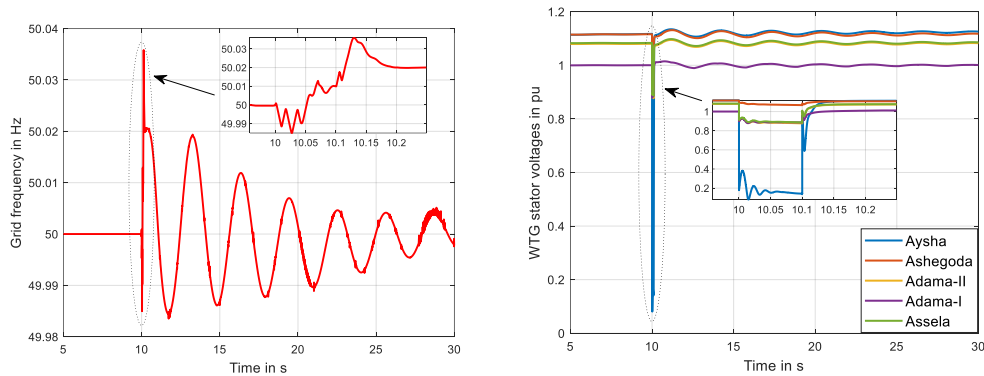
The existing steady-state case for the year 2022 has a total wind power generation of 564 MW which accounts for about 14 % of the total power generation. Moreover, conventional power plants with steam turbines generate less than 4.5 % of the total generation. Hence, more than 80 % of the power generation is from hydropower plants. As a case study, two scenarios have been considered, one with the existing condition and a second scenario with a higher penetration level of wind power (doubled the current penetration level to 28 %). A fault event of sudden load change from 81.2 MW to 162.4 MW at bus 158 (bus “203003” at DJIB-PK12 230 kV bus) is applied at time step of 10. The time-domain simulation results of the two scenarios, one with 14 % and the other with 28 % penetration level of wind power, are presented in Figure 6.16 and Figure 6.17, respectively.

Figure 6.16 shows stable responses to large load changes on the existing Ethiopian grid system where the penetration level of wind power is about 14 %. Figure 6.16 (a) presents the synchronous generator frequencies which are following the grid frequency shown in Figure 6.16 (b). In Figure 6.16 (c), it is clear that the wind farm voltages, at the aggregated wind generator points of connection, suffer from higher voltage dips. This can be typically noted in the Aysha wind power plant, where the voltage dip goes below 0.2 per unit during the fault duration which is practically due to the long transmission line that connect

the Aysha wind power plant and the national grid at Dire-Dawa substation. This is a typical impact of weak power system on the integration of higher share of wind capacity into a grid system.



(a) SG generator frequencies



(b) Grid frequency response

(c) Voltage responses at the five wind farms

Figure 6.16 Ethiopian grid system’s stable response to 100 % load change at bus 158 with wind power penetration level of 14 %

However, when the wind capacity penetration level increases to 28 % as explained in the second scenario, the transient analyses show that the increase in wind power capacity seems to significantly affect the weak grid. Unlike the third scenario in the case of 39-bus

system, the weak grid system falls into instable operation when 28 % of the power capacity is supplied from wind generators following large load changes, as described in scenario 1.

The transient responses of the second scenario are presented in Figure 6.17 below. The rotational frequency responses of the synchronous generators are presented in Figure 6.17 (a) and the corresponding calculated grid frequency response is shown in Figure 6.17 (b). The results in Figure 6.17 show that the weak grid system is instable following the disturbance in the network when the wind capacity is set to 28 % of the total power generation.

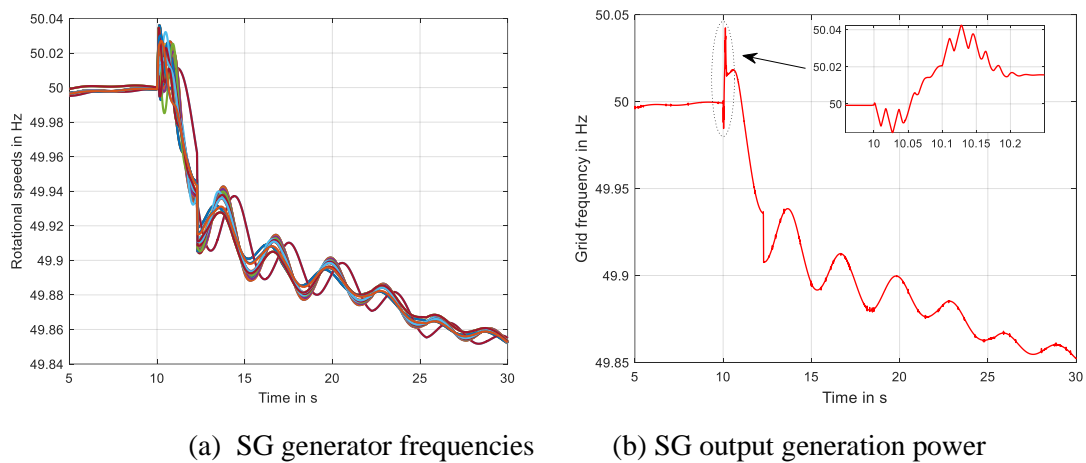


Figure 6.17 Ethiopian grid system's unstable response to 100 % load change at bus 158 with wind power penetration level of 28 %

It is actually difficult to realize what and where the problem is in the large system unlike the smaller grids in the previous test networks, but one can understand that an increase in wind power has significant impact on the wind generator voltage dips and grid frequencies, specifically in weak grid systems as the Ethiopian case, presented in Figure 6.16 and Figure 6.17.

7 Control Strategy to Regulate Grid Frequency with Higher Wind Power Share

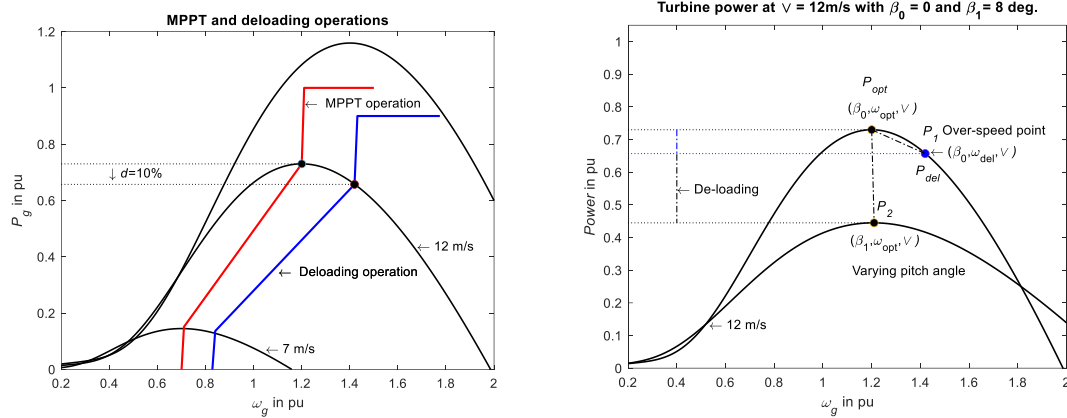
7.1 Introduction

Deployment of DFIG-based wind power generators electrically decouples the rotor-side energy source from the grid which results in a decrease of system inertia. Such limitations can potentially have an effect on the power grid dynamics, in particular, on the system frequency stability. Wind power plants (WPPs) are and will vibrantly continue contributing a significant share of electric power supply, and therefore, WPPs must participate in the frequency restoration process. As discussed in previous sections, the current WTGs are designed to generate at optimal electrical power output that limits the active power control capability during depressed frequency conditions. DFIG-based wind generators operate at variable wind speeds as they can host $\pm 30\%$ of its rated value by changing the rotor speed. In this regard, DFIG is designed to operate at various slip values which can be controlled based on the control reference power. Therefore, DFIG-based wind power plants can basically contribute to frequency control by adjusting the output power within the slip operation limit [67].

In this thesis work, DFIG-based wind turbines are modeled with virtual inertial response and primary frequency control module through de-loading the turbine [68], [69], [70]. The proposed frequency control module is integrated at a plant level to adopt the pre-defined power margin and dispatch it among the wind turbines in response to grid frequency deviations. The wind turbine frequency response is jointly achieved by rotor speed and pitch angle control schemes. The proposed module is tested in the third test network (microgrid) composed of DFIG-based wind park and thermal plant.

7.2 De-loading operations of DFIG-based wind power plants

De-loading operation of wind turbine helps WTG to take part in primary frequency regulation by which it can have sufficient generation margin at any instant. WTG can operate under stable de-loading operation by limiting the output so that the electrical output reference power, P_{ref} in Figure 4.8, is operating at lower value than the optimal power. Such load limitations can be achieved by either rotor over-speeding or by regulating the pitch angle so that its optimal value decreases depending on the wind speed. Figure 7.1 (a) shows a typical DFIG-based wind turbine control strategy for both the maximum power point tracking (MPPT) and de-loading operations.



(a) MPPT and de-loading operation strategies (b) Over-speeding and pitch angle regulation

Figure 7.1 De-loading operation of wind turbines (a) through rotor over-speeding and pitch angle regulation techniques (b)

Both control strategies are adopted in this work for a stable de-loading operation of wind generators. Figure 7.1 (b) shows that the output power can be reduced from P_{opt} to P_{del} by varying its rotor speed between ω_{opt} and ω_{del} or P_{opt} can be reduced more using pitch angle control techniques.

7.3 Proposed wind power plant frequency control module

Wind turbines in a wind farm might operate at different rotor speeds depending on the available wind speeds. Categorizing the number of wind turbines into a specific group-type is uncertain as the actual wind speed measurement at remote units are usually different. However, measuring the wind speed for each wind turbine and send to the central WPP decision module is not also practical for large systems. Thus, in this thesis work, the proposed wind power plant frequency control module is implemented by grouping the WTG units which have similar control strategy.

In this work, the wind turbines are generally grouped into four operation regions based on the available wind speed as in Figure 7.2. The group of wind turbines that receive low wind speeds (AB) are not made to participate in the de-loading operation. Hence, the other three groups of WTGs, namely, Type-1, Type-2 and Type-3, are participating on primary frequency restoration. The three types of WTGs are operating in wind speed intervals BC, CD and DE which are classified based on the wind speed and matching control strategy. Such type of classification allows to take full advantage of distinct regulation range for rotor over-speeding and pitch angle control which permit to use different de-loading control strategies.

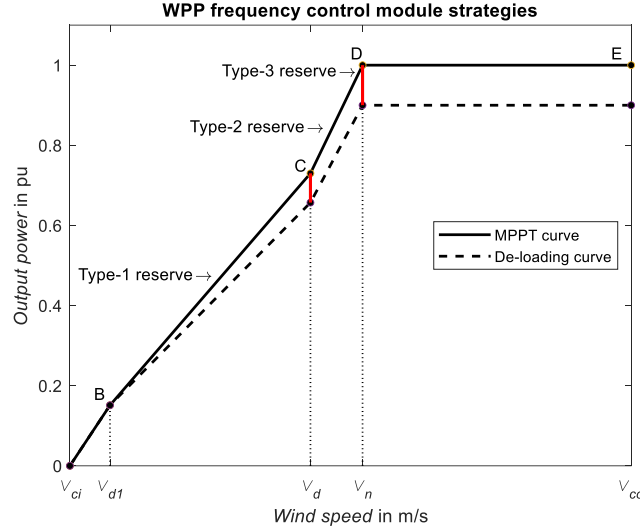


Figure 7.2 DFIG-based wind turbine types and corresponding reserve of de-loading operation

The three wind turbine types are initially operating at constant de-loading rate d_0 . The plant level decision module decides the new de-loading rate d_n and the frequency droop is based on the power constraint and the wind speed.

Type-1 WTGs receive wind speed between v_{d1} and v_d , where the first is the minimum wind speed that allows the turbine to start de-loading and the latter represents the upper wind speed limit in the BC range. In this range, only rotor over-speeding is applied to de-load the WTGs for stable operation. Using the optimal aerodynamic model in (4.7), the de-loading reference powers are defined as.

$$P_{\text{del}} = (1 - d_0)P_{\text{opt}} = (1 - d_0) \frac{\rho \pi R^5 C_{p\text{-max}}}{2\lambda_{\text{opt}}} \omega_{\text{opt}}^3 = 0.5 \rho \pi R^5 \frac{C_{p\text{-del}}}{\lambda_{\text{ref}}} \omega_{\text{del}}^3 \quad (7.1)$$

Where P_{opt} and P_{del} are the references for power at MPPT and power under de-loading operations, respectively. $C_{p\text{-max}}$ and $C_{p\text{-del}}$ are wind energy utilization coefficients at MPP and de-loading conditions, respectively. For constant wind, $C_{p\text{-del}}$ at optimal pitch angle ($\beta=0$) is determined as:

$$C_{p\text{-del}}(\lambda_{\text{ref}}, 0) = (1 - d) C_{p\text{-max}}(\lambda_{\text{opt}}, 0) \quad (7.2)$$

Where λ_{opt} and λ_{ref} are the tip speed ratios during optimal and de-loading operations of *Type-1* wind turbines. The rotor over-speeding at the initial de-loading rate between points B and C is determined by substituting the reference tip speed ratio and its optimal values in (7.1) as derived in (7.3).

$$\begin{aligned}
d_0 P_{\text{opt}} = P_{\text{opt}} - P_{\text{del}} &\rightarrow d_0 \omega_{\text{opt}}^3 = \omega_{\text{opt}}^3 - \omega_{\text{del}}^3 \left(\frac{\lambda_{\text{opt}}}{\lambda_{\text{ref}}} \right)^3 \\
&\rightarrow \left(\frac{\lambda_{\text{opt}}}{\lambda_{\text{ref}}} \right)^3 = (1 - d_0) \left(\frac{\omega_{\text{opt}}}{\omega_{\text{del}}} \right)^3 \\
&\rightarrow \omega_{\text{del}} = \sqrt[3]{1 - d_0} \frac{\lambda_{\text{ref}}}{\lambda_{\text{opt}}} \omega_{\text{opt}}
\end{aligned} \tag{7.3}$$

The de-loading reference tip speed ratio λ_{ref} can be first determined from lookup tables from $C_{p,\text{del}}-\lambda_{\text{ref}}-0$ curve. Moreover, the upper wind speed limit, v_d for the Type-1 control strategy can be calculated from (4.4) using λ_{ref} and the maximum rotor speed ω_{max} .

Type-2 wind turbines operate at a middle wind speed, in the range between v_d and v_n , where the over-speeding control reaches its upper limit at v_n . Thus, over-speeding alone cannot satisfy the required de-loading operation. Therefore, both over-speeding and pitch angle control are jointly applied to accomplish the required maximum reserve power for stable de-loading operation. As the turbine power is generating below its rated value, the reference power calculation for the optimal and de-loading operations are similar to that of Type-1 in (7.1).

However, in this case, the pitch angle is varying and so the reference tip speed ratio is first determined from $\omega_{\text{ref}} = \omega_{\text{max}}$ and $\lambda_{\text{ref}} = \omega_{\text{ref}} R/v$ and then the reference pitch angle is obtained from lookup table from $C_{p,\text{del}}-\lambda_{\text{ref}}-\beta_{\text{ref}}$.

$$C_{p,\text{del}}(\lambda_{\text{ref}}, \beta_{\text{ref}}) = (1 - d) C_{p,\text{max}}(\lambda_{\text{opt}}, 0) \tag{7.4}$$

Type-3 wind turbines are operating at wind speeds greater than the nominal wind speed v_n but less than the cut-out wind speed v_{co} . Over-speeding control has already reached its upper limit at the end of the CD control strategy. Therefore, the only technique to get more reserve at such high wind speeds can be realized by varying the pitch angle even more as can be seen in Figure 7.1 (b). The reference pitch angle is obtained from lookup table for $C_{p,\text{del}}-\lambda_{\text{ref}}-\beta_{\text{ref}}$ curve where $\omega_{\text{ref}} = \omega_{\text{max}}$ and $\lambda_{\text{ref}} = \omega_{\text{ref}} R/v$. The de-loaded power coefficient for such high wind speed is determined from the ratio factor of the rated power to the optimal power of the wind speed as in (7.5).

$$\begin{aligned}
C_{p,\text{rated}}(\lambda_{\text{ref}}, \beta_{\text{ref}}) &= \frac{P_{\text{rated}}}{P_{\text{opt},3}} C_{p,\text{max}}(\lambda_{\text{opt}}, 0) = K_r C_{p,\text{max}} \\
\rightarrow C_{p,\text{del}}(\lambda_{\text{ref}}, \beta_{\text{ref}}) &= (1 - d) K_r C_{p,\text{max}}(\lambda_{\text{ref}}, 0)
\end{aligned} \tag{7.5}$$

Where K_r is the ratio of rated power to the theoretical power corresponding to the wind speed. The reference power for de-loading operation is determined from the rated power P_{rated} as in (7.6).

$$\begin{aligned} P_{\text{opt}} &= P_{\text{rated}} \\ P_{\text{del},3} &= 0.5\rho\pi R^5 C_{\text{p-del}}(\lambda_{\text{ref}}, \beta_{\text{ref}}) (\omega_{\text{ref}} / \lambda_{\text{ref}})^3 \end{aligned} \quad (7.6)$$

Then, the reserve power P_{res} of a WPP using the initial de-loading rate d_0 is determined as:

$$P_{\text{res}} = P_{\text{opt}} - P_{\text{del}} \quad (7.7)$$

The proposed control module coordinates the virtual inertia response (VIR) and the primary frequency response (PFR) which reacts gradually to provide grid support that guarantee the frequency regulation reserves. In order to further provide more support for the grid with high wind power penetration, the grid operators can impose higher power constraints based on the maximum pre-determined incremental change in grid frequency.

The plant level frequency control module is modeled to dispatch an imposed power constraint by the grid operators over the operating units. The WPP is initially operating at steady-state condition with constant de-loading rate. Then, the decision module algorithm gives dispatching priority to the high wind speed turbines that guarantee the frequency regulation reserves. With this algorithm, Type-3 are given the first priority and if the sum of initial de-loading of this group is not enough to compensate the constraint, Type-2 and then Type-1 in order are dispensed for the primary frequency response as in Figure 7.3.

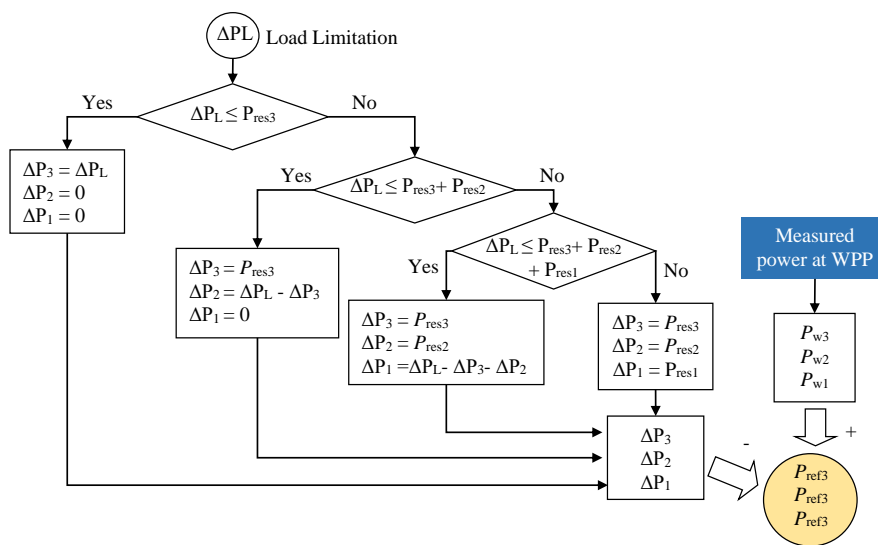


Figure 7.3 Algorithm in the WPP Control Module to dispatch the wind generators

With such arrangements, the new de-loading rate and the droop parameters of the turbines become variable which allows the turbines with less wind speeds to remain in operation while the plant load limitation is fulfilled by other wind turbines that have high wind speeds. This will optimize and improve the stable de-loading operation of the turbines and as well the WPP capacity rate.

The WPP operators segment the imposed power constraint to multiple generating units based on their respective initial reserves as in (7.7). The algorithm establishes new power reserve margins for the three turbine types that satisfy the pre-defined constraint. Hence, the new power margins will help to set the reference power P_{ref} and then a new de-loading operation point is determined at these respective reference powers. The new de-loading rating d_n is determined as:

$$d_n = \begin{cases} 1 - \frac{P_{ref}}{P_{opt}}; & \text{for Type-1 and Type-2} \\ 1 - \frac{P_{ref}}{P_{rated}}; & \text{for Type-3} \end{cases} \quad (7.8)$$

The WPP will then be ready to respond to any grid frequency change with the help of primary governor droop in the supplementary control loop. The actual droop parameter R_w is set to be variable and satisfy the power margins using the linear correlation with droop values as in Figure 7.4 [71].

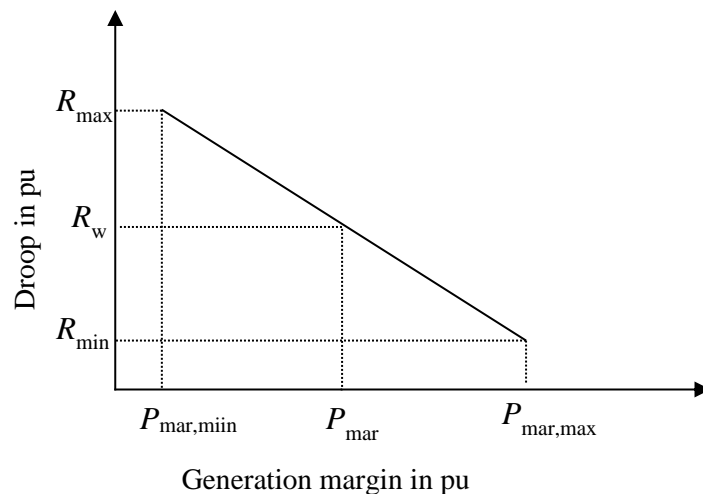


Figure 7.4 Speed droop values based on the generation margin

The grid codes of several countries demand governor droop settings in the range of 2 % to 6 %, for all generation units participating in system frequency regulation [70], [71]. Hence, in this thesis work, the wind turbine droop parameter is set to vary in the range

between 2 % to 5 %. Therefore, the droop parameters of the three turbine types are different based on their respective power margins. The reserve power ranges from the generation margins of Type-3 as $P_{\text{mar,max}}$ and Type-1 as $P_{\text{mar,min}}$. Therefore, the wind governor droop parameters R_w for the three wind turbine types are calculated from the linear function in (7.9).

$$R_w = R_{\text{min}} + \frac{R_{\text{max}} - R_{\text{min}}}{P_{\text{mar,max}} - P_{\text{mar,min}}} (P_{\text{mar,max}} - P_{\text{mar,ref}}) \quad (7.9)$$

The P - f droop characteristic of the primary frequency governor allows multiple generating units to share common load changes [11]. In this work, supplementary control loops have been integrated with the rotor-side converter control unit in response to the grid frequency change Δf . The primary frequency contribution ΔP of the wind generator depends on the droop parameter R_w of the speed governor as in (7.10).

$$\Delta P = \frac{\Delta f}{R_w} \quad (7.10)$$

The droop parameter determines the power-frequency characteristics of the generating WTGs. As pointed out above, the droop parameter is made to vary based on the wind turbine types. This allows wind turbines with high wind speed to increase their reference power more so that they primarily participate in the frequency response. Hence, the wind turbine type with lower droop setting is responsible for larger shares of primary frequency restoration.

7.4 Test system simulation for frequency enhancement

To verify the effectiveness of the control strategy, the proposed WPP frequency module has been implemented in a microgrid. The microgrid consists of an aggregated three groups of wind turbine types and a conventional generator to supply the load at bus 2 in Figure 7.5. A load with steady-state operation of 315 MW is connected at bus 2. The microgrid consists of an 85 MW thermal power plant and a WPP with installed capacity of 450 MW, which comprises three groups of wind turbines as described in subsection 7.3. Each WTG has 1.5 MW rating and can operate at variable wind speeds. The detailed parameter settings of the microgrid are provided in Appendix E. For the steady-state load condition, the three groups of WTGs run at wind speeds of 9 m/s, 13 m/s and 15 m/s so that the total WPP output power is 235 MW.

The grid frequency is determined from the system inertia and load damping as sum of all operating generators in the microgrid. The grid frequency varies depending on the supply-

load power balance (see Appendix E). The microgrid model with the proposed strategy control has been implemented in MATLAB/Simulink.

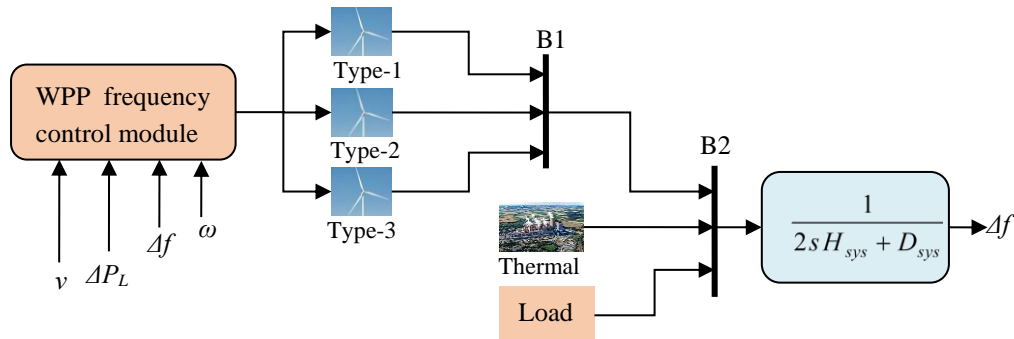


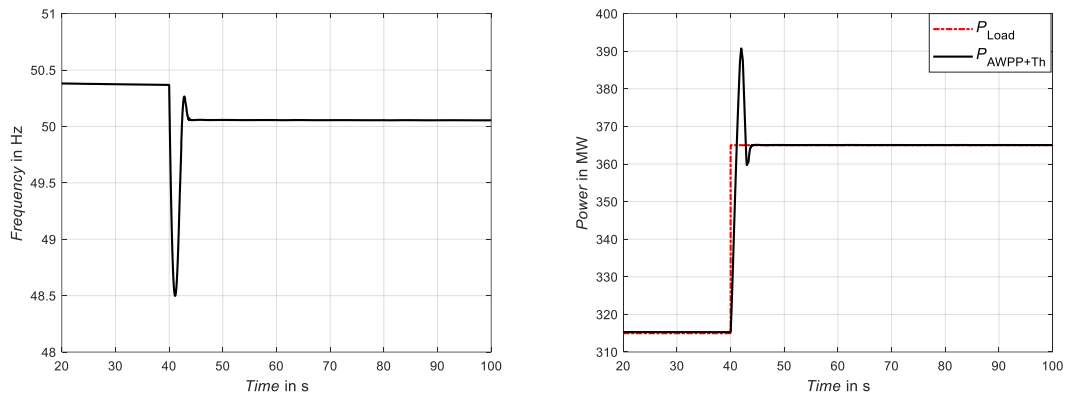
Figure 7.5 Microgrid with frequency control capability of WPP

The power flow analysis is first carried out to initialize the steady-state values of the dynamic variables in the model. All wind turbines initially start at a constant de-loading rate of 10 % and the WPP algorithm restates the new de-loading rate and wind governor droop values for the three wind turbine types. Table 7.1 shows the governor droop settings and de-loading rates for a grid-imposed power constraint of 50 MW. These droop parameters decide which group of wind turbines participates more in the primary frequency response in harmony to their reserves. The variable droop value will be helpful to allow Type-3 to contribute more to frequency control than Typ-2 and Type-1, this improves the computation time and stability of de-loading operation.

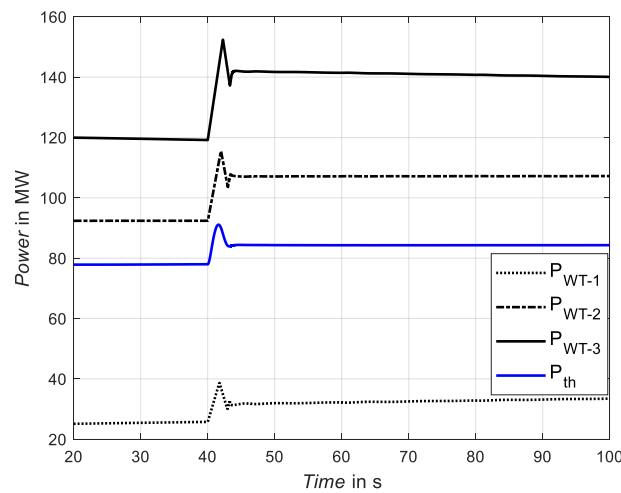
Table 7.1 The results of de-loading rate and droop settings with ΔPL of 50 MW

WTG group type	Wind speed in m/s	De-loading rate in %	Governor droop value in %
Type-1	9	0.00	4.00
Type-2	13	5.56	2.50
Type-3	15	10.00	2.00

The proposed model has been applied for different load change cases where the load change is less or greater than the pre-defined power constraint. Figure 7.6 (a) shows the microgrid frequency response to 50 MW load change at 40 seconds. The result in Figure 7.6 (a) shows that the proposed WPP control module is capable to regulate the frequency deviation with less than 10 seconds. The total power generation response of the aggregated wind turbines and thermal plant along with the load is presented in Figure 7.6 (b). Figure 7.6 (c) shows the output of the three types of aggregated power plants and thermal plant where the Type 3 wind turbines are more responsible for the deviation in frequency.



(a) Microgrid frequency response (b) Wind power output in response to load change



(c) Generation output power from the AWPP types and thermal plant

Figure 7.6 Frequency response of the aggregated wind generators for a load change of 50 MW with penetration level of wind power of 75 %

The proposed control models have also been applied with 100 % power supply from the WPP. To observe the action of the control module, the 50 MW load change was applied in two consecutive simulation times while the load change is within the upper limit of the WPP. The load has increased from 315 MW to 345 MW at simulation time 40 seconds and to 365 MW at 60 seconds at which the WPP is generating its optimal output as per the wind speeds. Figure 7.7 (a) and (b) show the sum of the virtual inertia and primary frequency responses for the consecutive load changes. It has been also observed that the WPP frequency response was slow with constant droop value.

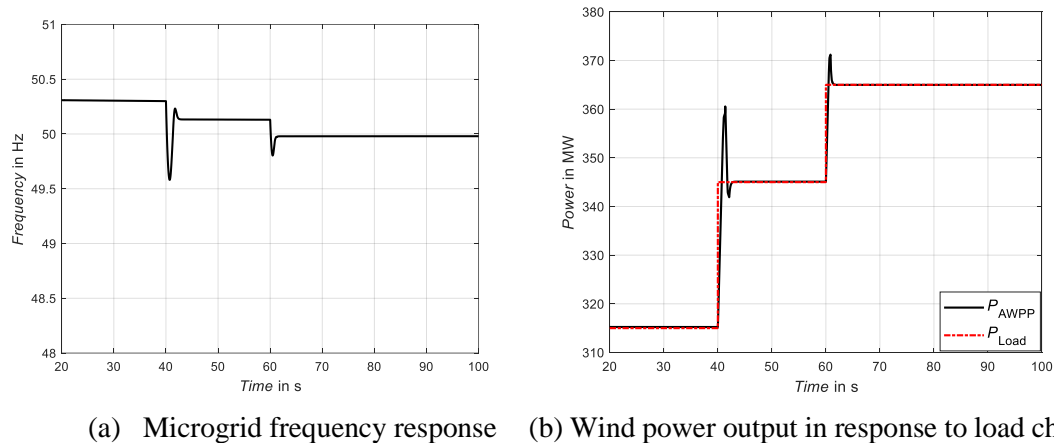


Figure 7.7 Virtual inertia and primary frequency responses of wind generators for consecutive load changes and penetration level of wind power of 100 %

To observe the model response for a load beyond the optimal WPP generation, the load has increased first to 365 MW at 40 seconds then to 380 MW at time 80 seconds. Figure 7.8 shows the grid frequency response for load deviation greater than the pre-defined power constraint.

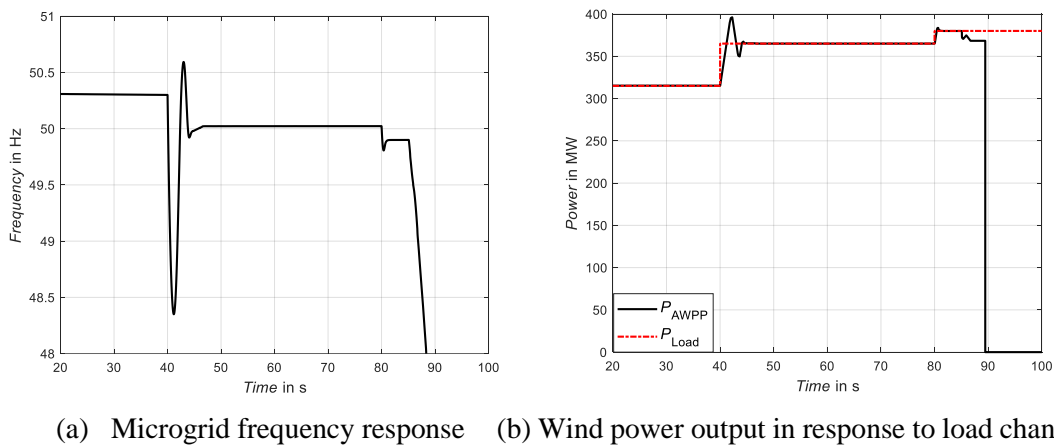


Figure 7.8 Unstable frequency response for a load change above the pre-defined power constraint

The proposed frequency control module has enhanced the frequency response. The wind turbines are operating at variable de-loading rate and variable droop parameter to get the reserve margin. This approach optimizes the stable de-loading operations of the turbines and improve the annual wind power plant capacity rate.

8 Conclusions and Future Work

The issue of environmental concern and strategies to shift the fossil fuel-based energy system to carbon-free energy resources has encouraged the employment of renewable energy resources. Currently, wind and solar resources are significant sources of electric power generation worldwide. The employment of such resources, specifically wind energy, is globally increasing and it will be among major electric power generation contributors in the near future. However, wind energy has a significant impact on the transient stability of the grid and is becoming more challenging for grid operators due to their unique behaviors which differs from conventional power generation. Therefore, investigating and evaluating the dynamic behaviors of wind turbine technologies and their impacts on power system dynamics is still an essential research topic so as to mitigate and enhance stable frequency and voltage.

This thesis work has realized the impacts of increasing wind power penetration levels on power system dynamics using various network topologies. In this regard, the major power system elements are modelled and simulated at various wind power penetration levels to realize the respective dynamic responses of transient disturbances. The network dynamics include models for conventional power stations, DFIG-based wind turbine generators, various control elements, transmission systems and transformers to study the influence of increasing wind power share in a large network system. The set of state dynamics is solved using numerical integration techniques in MATLAB/SIMULINK.

Various test networks are employed to stipulate the dynamic responses in different network topologies. The dynamic characteristics and transient response of DFIG-based wind turbines and its control capabilities have been studied and verified against manufacturer's datasheet using the 4-bus test system. The IEEE 39-bus system has been applied to evaluate the transient stability and investigate the dynamic impacts of integrating wind turbines specifically the issues related to dynamic voltage stability. The various simulation scenarios confirm that an increase in wind power share deteriorates the transient stability of the system. Power systems with large share of wind power are observed to behave differently and to challenge various system stability aspects, explicitly with voltage and frequency stability margins. Moreover, the DFIGs are observed to fail to withstand the grid voltage dips and remain connected under severe fault events because the generators are forced to disconnect themselves to protect the back-to-back rotor-side converters from rotor over-currents.

The proposed voltage control strategy using the joint application of STATCOM and rotor over-speeding techniques have been implemented in the 39-bus system. The proposed

control scheme is jointly implemented with modified STATCOM and over-speeding capability of rotor-side converter control. The proposed control strategy enables the DFIGs to improve their ride-through capability during grid voltage dip events. The simulation results of the test grid show, that the control strategy is efficient to suppress the rotor over-current and voltage fluctuations in the DC-link which is a vital element for LVRT capabilities. The proposed LVRT enhancement scheme is compared to the conventional DFIG control strategy and the results show, that the employment of both STATCOM and over-speeding control strategy lead to better transient behavior.

The two-bus test network is applied to demonstrate the frequency restoration capability of DFIG-based wind turbines under de-loading operations. The proposed frequency control module at a plant level monitors the contribution of various operating units, in a large wind farm, based on their respective wind speed and the grid frequency deviation.

As a future work, it is recommended that the proposed frequency control module is replaced by an integrated software tool within the wind farm SCADA system so that the decision to dispatch the constraint power over the operating units is monitored with the SCADA system.

9 References

- [1] IEA, "World Energy Outlook," December 2021. [Online]. Available: <https://www.iea.org/reports/world-energy-outlook-2021>.
- [2] S. Heier, Grid integration of wind energy: onshore and offshore conversion systems, John Wiley & Sons, 2014.
- [3] R. Adams, I. Aronovich, J. Ma, B. Badrzadeh und M. Barbieri, Modelling of Inverter-based Generation for Power System Dynamic, Joint Working Group C4/C6.35/CIREC, 2018.
- [4] N. J. Olimpo Anaya-Lara, J. Ekanayake, P. Cartwright und M. Hughes, Wind Energy Generation-Modelling, United Kingdom: John Wiley & Sons Ltd, 2009.
- [5] R. A. Kainth, „From First To The Finest: The Evolution Of Wind Turbines,“ Proxima Solutions GmnH, 2022. [Online]. Available: <https://proximasolutions.eu/blog/entries/the-evolution-of-wind-turbines>.
- [6] T. B. N. a. M. A. P. E. Muljadi, „Impact of Wind Power Plants on Voltage and Transient Stability of Power Systems,“ in *2008 IEEE Energy 2030 Conference*, 2008.
- [7] G. J. P. X. a. L. H. Chen Wei, „Study on voltage sag area and transient stability in power system with,“ in *2014 China International Conference on Electricity Distribution (CICED)*, 2014.
- [8] IRENA, „International Renewable Energy Agency, updated on Sep. 2021,“ Sep 2021. [Online]. Available: https://www.irena.org/IRENADocuments/-Statistical_Profiles/Africa/Ethiopia_Africa_RE_SP.pdf.
- [9] P. Brinckerhoff, „Ethiopian Power System Expansion Master Plan Study”, Expansion master plane prepared for EEP,“ Addis Ababa, 2015.
- [10] B. C. UMMELS, „Power System Operation with Large-Scale Wind Power in Liberalised Environments,“ Delf University of Technology, Netherlands, 2009.
- [11] P. Kundur, Power System Stability and Control, London: Mc Graw-Hill, Inc., 1994.
- [12] O. P. M. Abdelhay A. Sallam, „Power System Stability- Modelling, analysis and control,“ *IET Power and energy series*, Bd. Vol. 76, 2015.
- [13] M. G. C. G. a. N. B. S. Nuzzo, „Analysis, Modeling, and Design Considerations for the Excitation Systems of,“ *IEEE Transactions on Industrial Electronics*, Bd. 65, Nr. 4, pp. 2996-3007, 2018.

- [14] J. M. J. a. R. A. Manwell, *Wind Energy Explained. Theory, Design and Application*, John Wiley and, 2002.
- [15] F. Z. Joyce Lee, „Global Wind Report 2021,“ GWEC, 2021.
- [16] Fraunhofer-ISE, „Fraunhofer,“ 2022. [Online]. Available: https://energy-charts.info/charts/installed_power/chart.htm?l=en&c=DE&stacking=single&chartColumnSorting=default&legendItems=00000000000110&year=-1. [Zugriff am 13 09 2022].
- [17] J. Fortmann, *Modeling of wind turbines with doubly-fed generator system*, Germany: Springer Fachmedien Wiesbaden, 2015.
- [18] R. A. Vijay Vittal, *Grid Integration and Dynamic Impact of Wind Energy*, New York: Springer Science + Business Media, 2013.
- [19] Y. H. a. F. B. Z. Chen, „Stability Improvement of Induction Generator-Based Wind Turbine System,“ *IET Renewable Power Generation*, Bd. 1, Nr. 1, pp. 81-93, 2007.
- [20] R. A. P. C. D. K. a. G. S. N. Jenkins, „Embedded Generation,“ *Power and Energy Series 31*, 2000.
- [21] K. E. Okedu, „Enhancing the performance of DFIG variable speed wind turbine using parallel integrated capacitor and modified,“ *IET Genera. Transm. Distrib.*, Bd. 13, Nr. 2019b, pp. 3378-3387, 2019.
- [22] A. G. O. A.-L. a. K. L. L. S. Naser, „Voltage stability of transmission network with different penetration levels of wind generation,“ in *45th International Universities Power Engineering Conference UPEC2010*, 2010.
- [23] A. S.-Y. N. M. K. A. P. N. Boonchiam, „Voltage Stability in Power Network when Connected Wind Farm Generation,“ in *International Conference on Power Electronics and Drive Systems (PEDS)*, Taipei, 2009.
- [24] S. I. H.N.D. Le, „Substantial control strategies of DFIG wind power system during grid transient faults,“ in *IEEE Transmission and Distribution Conference and Exposition*, 2008.
- [25] J. L. M. A. R. L. M. I. G. Abad, „Doubly fed induction machine modeling and control for wind energy generation”, „*IEEE Press series*, 2011.
- [26] K. W. Slootweg JG, „Modelling and Analysing Impacts of Wind Power on Transient Stability of Power Systems,“ *Wind Engineering*, Bd. 26, Nr. 1, pp. 3-20, 2002.
- [27] S. Xia, Q. Zhang, S. Hussain, B. Hong und W. Zou, „Impacts of Integration of Wind Farms on Power System Transient Stability,“ *Appl. Sci.*, Bd. 8, p. 1289, 2018.

- [28] H. W. a. C. Z. Rui, „Review of power system stability with high wind power penetration,“ in *Proc. 41th Annu. Conf. IEEE Indus. Electron. Soc.*, Yokohama, Japan, 2015.
- [29] I. a. A. Lallu, „Impact of wind generators in power system stability,“ *WSEAS Trans. Power Syst.*, Bd. 13, pp. 235-248, 2018.
- [30] M. V. K. K. Sree Latha, „STATCOM for enhancement of voltage stability of a DFIG driven wind turbine,“ in *2014 POWER AND ENERGY SYSTEMS: TOWARDS SUSTAINABLE ENERGY*, 2014.
- [31] P. S. T. M. Masaud, „Study of the implementation of STATCOM on dfig-based wind farm connected to a power system,“ in *2012 IEEE PES Innovative Smart Grid Technologies (ISGT)*, 2012.
- [32] F. F. Amjady, „Determination of frequency stability border of power system to set the thresholds of under frequency load shedding relays,“ *Energy Conversion and Management*, Bd. 51, Nr. 10, pp. 1864-1872, 2010.
- [33] T. Ackermann, *Wind Power in Power Systems*, 2nd Edition Hrsg., John Wiley & Sons Inc, 2012.
- [34] F. B. C. a. N. Z. D. Xu, *Advanced control of doubly fed induction generator for wind power systems*, John Wiley & Sons Inc, 2018.
- [35] Z. C. W. M. Tahaguas Woldu, „Modeling of synchronous generator with fast-response excitation system for studying power network transients,“ in *NEIS 2019: Conference on Sustainable Energy Supply and Energy Storage Systems*, Hambrug, 2019.
- [36] K. B. K., *Power System Stability and Control*, Electrical Engineering dept., IIT Bombay, 2015.
- [37] P. J. A. V. A. G. Kundur P., „Definition and classification of power system stability,“ *IEEE Transactions on Power Systems*, Bd. 19, Nr. 2, pp. 1387-1401, 2004.
- [38] K. Yamashita, „Modelling and dynamic performance of inverter-based generation in power system transmission and distribution studies,“ co-covener of CIGRE JWG* C4/C6.35/CIRED, August 2018. [Online]. Available: <https://e-cigre.org>.
- [39] ESIG, „Generic Models (Individual Turbines),“ ESIG, 2021. [Online]. Available: <https://www.esig.energy/>. [Zugriff am August 2021].
- [40] WECC, „WECC Second Generation of Wind Turbines Models Guidelines,“ Technical Report; Western Electricity Coordinating Council:, Salt Lake City, UT, USA, 2014.
- [41] K. Padiyar, *Power System Dynamics - Stability and Control*, 2nd edn. Hrsg., India: BS Publications, 2008.

- [42] A. F. P.M. Anderson, *Power system control and Stability*, 2nd edn. Hrsg., USA: John Wiley & Sons Inc, 2003.
- [43] M. P. P.W. Sauer, *Power System Dynamics and Stability*, New Jersey: Prentice Hall, 1998.
- [44] S. Chapman, *Electrical Machinery & Power System Fundamentals*, New York, United States of America: McGraw-Hill, 2005.
- [45] W. Martin, „Power Network Planning and Operation,“ Version 2020. [Online]. Available: https://www.lena.ovgu.de/lena_media/Dokumente+und+Skripte/Skript_PNP.pdf. [Zugriff am August 2021].
- [46] IEEE standard 1110-2002, „IEEE Guide for Synchronous Generator Modeling Practices in Stability Analyses,“ *Revision of IEEE Std 1110-1991*, 2002.
- [47] IEEE Std 421.5-2005, „IEEE Recommended Practice for Excitation System Models for Power System Stability Studies,“ *Revision of IEEE Std 421.5-2005*, 2016.
- [48] C. C. K. P. W. G. Y. Wu, „Voltage Stability Constrained Optimal Dispatch in Deregulated Power Systems,“ *IET Generation, Transmission & Distribution*, Bd. 1, pp. 761-768, Feb. 2007.
- [49] K. Y. M. E. P. P. S.-G. J. Ellis A, „Description and technical specifications for generic WTG models – a status report,“ in *IEEE/PES power systems conference and exposition (PSCE)*, 2011.
- [50] J. B. E. L. H. a. X. N. Jenkins, „Dynamic modeling of doubly fed induction generator wind turbines,“ *IEEE Trans. Power System*, Bd. 18, pp. 803-809, 2003.
- [51] Z. Lubosny, „Wind turbine operation in electric power systems. Advanced modeling,“ ETDEWEB, 01 Jul 2003. [Online]. Available: <https://www.osti.gov/etde-web/biblio/20397453>. [Zugriff am 2021].
- [52] F. B. C. a. N. Z. D. Xu, *Advanced control of doubly fed induction generator for wind power systems*, Wiley-IEEE Press, 2018.
- [53] B. C. P. F. Mei, „Modelling of doubly-fed induction generator for power system stability study,“ in *2008 IEEE Power and Energy Society General Meeting - Conversion and Delivery of Electrical Energy in the 21st Century*, 2008.
- [54] X.-P. Z. K. G. a. P. J. F. Wu, „Small signal stability analysis and optimal control of a wind turbine with doubly fed-induction generator,“ *IET Generation, Transmission and Distribution* 1(5):, pp. 751-760, 2007.
- [55] R. S. R. Ghadir Radman, „Dynamic model for power systems with multiple FACTS controllers,“ *Electric Power Systems Research*, Bd. 78, Nr. 3, pp. 361-371, 2008.

- [56] P. K. S. T. M. Masaud, „Study of the implementation of STATCOM on DFIG-based wind farm connected to a power system,“ in *2012 IEEE PES Innovative Smart Grid Technologies (ISGT)*, 2012.
- [57] C. Z. M. W. T. A. Woldu, „A New Method for Prediction of Static and Dynamic Voltage Collapse Using Bus Parameters in Large Power Networks,“ in *2020 IEEE PES Innovative Smart Grid Technologies Europe (ISGT-Europe)*, 2020.
- [58] R. Natarajan, *Computer-Aided Power System Analysis*, United States: CRC Press, 2002.
- [59] C. C. K. P. W. G. Y. Wu, „Voltage Stability Constrained Optimal Dispatch in Deregulated Power Systems,“ *IET Generation, Transmission & Distribution*, Bd. 1, pp. 761-768, 2007.
- [60] A. S.-Y. N. M. K. A. P. N. Boonchiam, „Voltage Stability in Power Network when Connected Wind Farm Generators,“ in *International Conference on Power Electronics and Drive Systems (PEDS)*, aipei, 2009.
- [61] F. M. A. S. A. T. M. F. B. K. S. A. C. M. Z. & R. N. A. Albatsh, „A Comparative analysis of line stability indices for dynamic voltage stability,“ in *IEEE International Conference on Engineering Technology and Technopreneurship (ICE2T)*, 2017.
- [62] F. M. Moghavvemi, „Technique for Contingency Monitoring and Voltage Collapse Prediction,“ *IEEE Proceeding on Generation, Transmission and Distribution*, Bd. 145, Nr. 6, pp. 634-640, 1998.
- [63] G. M. P. K. B. Gao, „Voltage Stability Evaluation using Modal Analysis,“ *EEE/PES*, Bd. 7, Nr. 4, pp. 1529-1536, 1991.
- [64] M. Nizam, „Dynamic Voltage Collapse Prediction on a Practical Power System Using Power Transfer Stability Index,“ in *5th Student Conference on Research and Development*, Malesia, 2007.
- [65] C. Canizares, „oltage Stability Assessment: Concepts, Practices and Tools” IEEE/PES Power System Stability Subcommittee Special Publication,“ in *IEEE/PES Power System Stability Subcommittee Special Publication*, 2002.
- [66] ILLINOIS, „Illinois Center for a Smarter Electric Grid (ICSEG),“ University of Illinois at Urbana-Champaign, 2022. [Online]. Available: <https://icseg.iti.illinois.edu/ieee-39-bus-system/>. [Zugriff am June 2021].
- [67] R. L. J. De Almeida, „Participation of doubly fed induction wind generators in system frequency regulation,“ *IEEE Trans Power Syst*, Bd. 22, Nr. 3, pp. 944-950, 2007.

-
- [68] M. W. Tahaguas A. Woldu, „Analysis and Modeling of DFIG-Based Wind Turbines with Variable Frequency Regulation Capability,“ in *The 18th International conference on European energy market (EEM22)* , [in press], 2022.
- [69] P. S. H. D. M. S. B. R. B. D. Kumar, Modified Deloading Strategy of Wind Turbine Generators for Primary Frequency Regulation in Micro-Grid, Springer Nature Singapore Pte Ltd., 2020.
- [70] W. M. Erlich I, „Primary frequency control by wind turbines,“ *Power and Energy Society General Meeting, IEEE*, 2010.
- [71] K. Yamashita, „Modelling and dynamic performance of inverter-based generation,“ co-covener of CIGRE JWG* C4/C6.35/CIREN, 2018.

Appendices

A DFIG-based wind turbine input data

In this thesis work, two types of DFIG-based wind turbines are considered. The first is a 2.0 MW wind turbine whose detailed datasheet is presented in Table A.1 and A.2. The second one is a 1.5 MW DFIG-based wind turbine, which is the most widely used wind turbine in the glob, whose detailed data for dynamic simulation is depicted in Table A.3 and A.4. The control input data of the wind turbines are not vender specific, which were evaluated by tuning to the control outputs to the steady-state operation. While most of the generator and turbine data are taken from literatures source which in turn are tracked from actual operating wind turbines such are Enercon E-82 E2 and General Electric GE 1.5 MW, respectively.

Table A.1 Generator and turbine parameters of 2 MW DFIG [26]

Rated power	2 MW	Stator resistance	0.00488 Ω	Cut-in wind speed	4 m/s
Rated voltage	690 V	Stator linkage inductance	0.09241 H	Rated wind speed	12m/s
Rotor diameter	84 m	Mutual inductance	3.9527 H	Cut-out wind speed	25m/s
Number of Poles	4	Rotor resistance	0.00488 Ω	Optimal pitch angle	0 ⁰
Min. rotor speed	9 rpm	Rotor linkage inductance	0.09955 H	Rotor blade	38 m
Max. rotor speed	18rpm	Stator/rotor turns ratio	1/3	Geer-box ratio	100
Generator inertia	0.94s	Nominal Torque	10610Nm	Turbine inertia	4.33s

Table A.2 Converter and pitch control parameters of 2 MW DFIG [26]

DC voltage	1200 V	Kp_power_reg	4 pu	Kp_DC_reg	8 pu
Capacitance	80 mF	Ki_power_reg	10 pu	Ki_DC_reg	40 pu
Resistance_LR	1.5e-3pu	Kp_Q_reg	4 pu	Kp_grid_side_cur_reg	1 pu
Inductance_LR	0.15 pu	Ki_Q_reg	10 pu	Ki_grid_side_cur_reg	100 pu
Switching freq.	4e-3 Hz	Kp_rotor_side_cur_reg	1 pu	Kp_pitchangle	150
Crowbar	1/5 Ohm	Ki_rotor_side_cur_reg	100 pu	Ki_pitchangle	25

Table A.3 Generator and turbine parameters of 1.5 MW DFIG [48]

Rated power	1.5MW	Stator resistance	0.0071 Ω	Cut-in wind speed-	4 m/s
Rated voltage	575 V	Stator linkage inductance	0.171H	Rated wind speed	13.3m/s
Rotor diameter	38 m	Mutual inductance	3.90 H	Cut-out wind speed	22 m/s
Number of Poles	6	Rotor resistance	0.005 Ω	Optimal pitch angle	0 ⁰
Min. rotor speed	9 rpm	Rotor linkage inductance	0.156H	Rotor blade	38 m
Max. rotor speed	22 rpm	Stator/rotor turns ratio	1/3	Geer-box ratio	67
Generator inertia	0.84s	Nominal Torque	7960Nm	Turbine inertia	4.0s

Table A.4 Converter and pitch control parameters of 1.5 MW DFIG [48]

DC voltage	1200 V	Kp_power_reg	1.0 pu	Kp_DC_reg	0.002pu
Capacitance	10 mF	Ki_power_reg	100 pu	Ki_DC_reg	0.05 pu
Resistance_LR	1.5e-3pu	Kp_Q_reg	0.05pu	Kp_grid_side_cur_reg	1 pu
Inductance_LR	0.15 pu	Ki_Q_reg	5.0 pu	Ki_grid_side_cur_reg	100 pu
Switching freq.	3.2e-3 Hz	Kp_rotor_side_cur_reg	0.3 pu	Kp_pitchangle	500
Crowbar	1/5 Ohm	Ki_rotor_side_cur_reg	8.0 pu	Ki_pitchangle	0

B 4-Bus test network data

The 4-bus test system’s input data for the steady-state and dynamic analysis are given below. The test system frequency is selected to be 50 Hertz.

Table A.5 Bus data for 4-bus test system

Bus no.	Type	Nominal voltage in kV	P_G in MW	Voltage set in pu	P_L in MW	Q_L in MW	U_{min} in pu	U_{max} in pu
1	2	20	10.0	1.025	--	--	0.8	1.1
2	0	20	--	--	5.0	1.64	0.8	1.1
3	0	220	--	--	10.0	3.28	0.8	1.1
4	3	220	6.0	1.04	--	--	0.8	1.1

Note that the bus types are defined as 0 for PQ buses, 2 for PU buses and 3 for slack bus.

Table A.6 Synchronous machine data for 4-bus test system

Bus no.	S_r in MW	H in sec	D in pu	R_s in pu	X_d in pu	X_q in pu	X'_d in pu	X'_q in pu	T'_{d0} in sec	T'_{q0} in sec
4	60	3.92	0.02	0	1.7199	1.6598	0.230	0.378	6	0.535

Note that the per unit values are calculated based on the respective machine ratings and corresponding generator terminal voltages as given in Table A.5.

Table A.7 Transmission line data for 4-bus test system

Branch no.	From bus	To bus	R in Ω/km	X in Ω/km	C in nF/km	G in $\mu s/km$	I_{max} in kA	CB Status	Length (km)	Line type
1	1	2	0.0274	0.0183	0.3906	0	0.8	1;1	--	Standard 20 kV
2	3	4	0.0757	0.4055	8.3168	0	1.5	1;1	--	Standard 220 kV

Table A.8 Two winding transformer data for 4-bus test system

Branch no.	From bus	To bus	HV in kV	LV in kV	S_r in MVA	u_K in %	P_k in kW	CB Status	Tx. Tap	Line type
3	3	2	220	20	250	14.4	240	1;1	0	Standard 220/20 kV

C New England test network data

The New England network (IEEE 39-bus system) has the following input data for the steady-state and dynamic analysis. The base frequency of the IEEE 39-bus system is 60 Hertz. The dynamic parameters of the synchronous generators are based on 4-th order model of hydropower plants.

Table A.9 Bus data for New England test network (39-bus system)

Bus no.	Type	Base voltage in kV	P_G in MW	Voltage set in pu	P_L in MW	Q_L in MW	U_{min} in pu	U_{max} in pu
1	0	345	10.0	--	--	--	0.8	1.1
2	0	345	--	--	--	--	0.8	1.1
3	0	345	--	--	322	0	0.8	1.1
4	0	345	6.0	--	500	183.95	0.8	1.1
5	0	345	--	--	--	--	0.8	1.1
6	0	345	--	--	--	--	0.8	1.1
7	0	345	--	--	233.8	84	0.8	1.1
8	0	345	--	--	522	175.98	0.8	1.1
9	0	345	--	--	--	--	0.8	1.1
10	0	345	--	--	--	--	0.8	1.1
11	0	345	--	--	--	--	0.8	1.1
12	0	138	--	--	7.5	88.02	0.8	1.1
13	0	345	--	--	--	--	0.8	1.1
14	0	345	--	--	--	--	0.8	1.1
15	0	345	--	--	320	152.98	0.8	1.1
16	0	345	--	--	329	32.35	0.8	1.1
17	0	345	--	--	--	--	0.8	1.1
18	0	345	--	--	158	30.04	0.8	1.1
19	0	345	--	--	--	--	0.8	1.1
20	0	230	--	--	628	103.06	0.8	1.1
21	0	345	--	--	274	114.98	0.8	1.1
22	0	345	--	--	--	--	0.8	1.1
23	0	345	--	--	247.5	84.64	0.8	1.1
24	0	345	--	--	308.6	92.14	0.8	1.1
25	0	345	--	--	224	47.21	0.8	1.1
26	0	345	--	--	139	17.00	0.8	1.1
27	0	345	--	--	281	75.56	0.8	1.1
28	0	345	--	--	206	27.67	0.8	1.1
29	0	345	--	--	283.5	26.99	0.8	1.1
30	2	16.5	278.6	0.982	--	--	0.8	1.1
31	3	16.5	632	0.9972	9.2	4.6	0.8	1.1
32	2	16.5	508	1.0123	--	--	0.8	1.1
33	2	16.5	560	1.0635	--	--	0.8	1.1
34	2	16.5	540	1.0278	--	--	0.8	1.1

35	2	16.5	830	1.0265	--	--	0.8	1.1
36	2	16.5	1000	1.03	--	--	0.8	1.1
37	2	16.5	278.6	0.982	--	--	0.8	1.1
38	2	16.5	632	0.9972	--	--	0.8	1.1
39	2	345	508	1.0123	1104	250	0.8	1.1

Table A.10 Synchronous machine data for IEEE 39-bus system bus

Bus no.	Sr in MW	H in sec	D in pu	R _s in pu	X _d in pu	X _q in pu	X' _d in pu	X' _q in pu	T' _{d0} in sec	T' _{q0} in sec
30	1000	42	0.02	0	0.1	0.069	0.031	0.05	10.2	1.5
31	700	30.3	0.02	0	0.295	0.282	0.0697	0.17	6.56	1.5
32	800	35.8	0.02	0	0.2495	0.237	0.0531	0.0876	5.7	1.5
33	800	28.6	0.02	0	0.262	0.258	0.0436	0.166	5.69	1.5
34	600	26	0.02	0	0.67	0.62	0.132	0.166	5.4	0.44
35	800	34.8	0.02	0	0.254	0.241	0.05	0.0814	7.3	0.4
36	700	26.4	0.02	0	0.295	0.292	0.049	0.186	5.66	1.5
37	700	24.3	0.02	0	0.29	0.28	0.057	0.0911	6.7	0.41
38	1000	34.5	0.02	0	0.2106	0.205	0.057	0.0587	4.79	1.96
39	10000	500	0.02	0	0.02	0.019	0.006	0.008	7	0.7

Note that the per unit values are calculated based on the respective machine ratings in column 2 of Table A.10 and corresponding generator terminal voltages given in Table A.10.

Table A.11 Transmission line data for New England test network (39-bus system)

Branch no.	From bus	To bus	R in Ω/km	X in Ω/km	C in nF/km	G in $\mu\text{s}/\text{km}$	I_{max} in kA	CB Status	Length (km)	Line type
L1	1	2	4.1659	48.9193	1592.3567	0	2.5	1;1	1.00	L1 345 kV
L2	1	39	1.1903	29.7563	1592.3567	0	2.5	1;1	1.00	L2 345 kV
L3	2	3	1.5473	17.9728	530.78556	0	2.5	1;1	1.00	L3 345 kV
L4	2	25	8.3317	10.2362	265.39278	0	2.5	1;1	1.00	L4 345 kV
L5	3	4	1.5473	25.3523	530.78556	0	2.5	1;1	1.00	L5 345 kV
L6	3	18	1.3093	15.8303	530.78556	0	2.5	1;1	1.00	L6 345 kV
L7	4	5	0.9522	15.2352	265.39278	0	2.5	1;1	1.00	L7 345 kV
L8	4	14	0.9522	15.3542	265.39278	0	2.5	1;1	1.00	L8 345 kV
L9	5	6	0.2381	3.0946	0	0	2.5	1;1	1.00	L9 345 kV
L10	5	8	0.9522	13.3308	265.39278	0	2.5	1;1	1.00	L10 345 kV
L11	6	7	0.7141	10.9503	265.39278	0	2.5	1;1	1.00	L11 345 kV
L12	6	11	0.8332	9.7601	265.39278	0	1	1;1	1.00	L12 138 kV
L13	7	8	0.4761	5.4752	265.39278	0	2.5	1;1	1.00	L13 345 kV
L14	8	9	2.7376	43.2061	796.17834	0	2.5	1;1	1.00	L14 345 kV
L15	9	39	1.1903	29.7563	2653.9278	0	2.5	1;1	1.00	L15 345 kV
L16	10	11	0.4761	5.1181	265.39278	0	2.5	1;1	1.00	L16 345 kV
L17	10	13	0.4761	5.1181	265.39278	0	2.5	1;1	1.00	L17 345 kV
L18	13	14	1.0712	12.0215	265.39278	0	2.5	1;1	1.00	L18 345 kV
L19	14	15	2.1424	25.8284	796.17834	0	2.5	1;1	1.00	L19 345 kV
L20	15	16	1.0712	11.1883	265.39278	0	1.5	1;1	1.00	L20 230 kV
L21	16	17	0.8332	10.5932	265.39278	0	2.5	1;1	1.00	L21 345 kV
L22	16	19	1.9044	23.2099	796.17834	0	2.5	1;1	1.00	L22 345 kV
L23	16	21	0.9522	16.0684	530.78556	0	2.5	1;1	1.00	L23 345 kV
L24	16	24	0.3571	7.0225	265.39278	0	2.5	1;1	1.00	L24 345 kV
L25	17	18	0.8332	9.7601	265.39278	0	2.5	1;1	1.00	L25 345 kV
L26	17	27	1.5473	20.5913	796.17834	0	2.5	1;1	1.00	L26 345 kV
L27	21	22	0.9522	16.6635	530.78556	0	2.5	1;1	1.00	L27 345 kV
L28	22	23	0.7141	11.4264	530.78556	0	2.5	1;1	1.00	L28 345 kV
L29	23	24	2.6186	41.6588	796.17834	0	2.5	1;1	1.00	L29 345 kV
L30	25	26	3.8088	38.4451	1061.5711	0	2.5	1;1	1.00	L30 345 kV
L31	26	27	1.6663	17.4967	530.78556	0	2.5	1;1	1.00	L31 345 kV
L32	26	28	5.1181	56.4178	1857.7495	0	2.5	1;1	1.00	L32 345 kV
L33	26	29	6.7844	74.3906	2388.535	0	2.5	1;1	1.00	L33 345 kV
L34	28	29	1.6663	17.9728	530.78556	0	2.5	1;1	1.00	L34 345 kV

Table A.12 Two-winding transformer data for New England test network (39-bus system)

Branch no.	From bus	To bus	HV in kV	LV in kV	S_r in MVA	u_K in %	P_k in kW	CB Status	Tx. Tap	Line type
T1	11	12	345	138	500	12.5	140	1;1	0	Standard 345/138
T2	13	12	345	138	500	12.5	140	1;1	0	Standard 345/138
T3	6	31	345	16,5	300	9	180	1;1	0	Standard 345/16,5
T4	10	32	345	16,5	300	9	180	1;1	0	Standard 345/16,5
T5	19	33	345	16,5	300	9	180	1;1	0	Standard 345/16,5
T6	20	34	230	16,5	250	14.4	160	1;1	0	Standard 230/16,5
T7	22	35	345	16,5	300	9	180	1;1	0	Standard 345/16,5
T8	23	36	345	16,5	300	9	180	1;1	0	Standard 345/16,5
T9	25	37	345	16,5	300	9	180	1;1	0	Standard 345/16,5
T10	2	30	345	16,5	300	9	180	1;1	0	Standard 345/16,5
T11	29	38	345	16,5	300	9	180	1;1	0	Standard 345/16,5
T12	19	20	345	230	900	14	100	1;1	0	Standard 345/230

D The Ethiopian power network data

The study in [9] shows that Ethiopia has an incredible exploitable resource potential - among which about 45 GW hydropower, 100 GW wind power, 7 GW Geothermal, and an average daily solar irradiation of 5.2 kWh/m². Despite the abundant natural resources and huge energy potential of Ethiopia, only about 44 % of its population has access to electricity. Ethiopia has been suffering from energy shortages that has been resulting in load shedding for the last decade. The country is struggling to expand the grid and supply electricity to a population of over 115 million people with an estimated demand growth of approximately 30 % per year [9]. As a result of Ethiopia's rapid GDP growth over the previous decade, the demand for electricity has been steadily increasing. Ethiopian electric power (EEP) is a state-owned utility which is engaged in development, construction, operation, and management of power plants and power transmission lines.

Ethiopia's current installed generation capacity is about 4.5 GW. Hydropower accounts for approximately 82 % of the existing installed capacity, while wind source reaches up to 14 %. The remaining 4 % is from thermal sources [8]. The Ethiopian grid, with a hydro dominated system, has been severely affected by shortages of rainfall or droughts and the ministry of energy has put forward a strategic plan to diversify the generation sources with other types such as wind, solar and geothermal that will result in a more climate-resilient power system. Other than hydropower, Ethiopia also has three wind farms, collectively generating 324 MW, and a few diesel plants, generating 143 MW, with the rest being generated by waste-to-energy (25 MW), solar power (14 MW) and geothermal

power (7.5 MW) [8]. Several large hydro and wind power plants are currently under development, such as the massive 5.6 GW Great Ethiopian Renaissance Dam (GERD), the 254 MW Genale Dawa hydropower project, the 120 MW Aysha wind power project and 100 MW Asela wind power project. Despite the incredible efforts towards generating electricity from hydropower, there is a huge gap in diversifying the energy mix.

The Ethiopian grid has currently 17,448 km total transmission line length, with additional 4,000 km under construction. The national grid has started exporting electricity to Djibouti and Sudan, up to 100 MW each. Ethiopia is also negotiating a power purchase agreement (PPA) to begin exporting up to 400 MW of power to Kenya [9].

Based on the master plan in [9], the projected total installed generation capacity will be 10,358 MW by the end of 2022. Based on the long-term projected plan, the grid system will be supplied by about 50 % from wind and solar in the year 2030. According to the forecast plan of EEP 2015-master plan [9], the wind energy penetration level alone will reach to 28 % in 2030.

Table A.13 shows the base value of the conational generators for the existing Ethiopian network scenario. Table A.14 show the aggregated wind power plants included in the simulation for the first case (14 % of wind power penetration).

Table A.13 Base load data of the existing conventional generators for the stable case

Generation ID	Bus ID	Active Power in MW	Voltage set point in pu	Generation Type
BELES-1 15.000	907001	92.0079	1	Hydro
T-ABA2-1 10.500	907002	20.4762	1	Hydro
BELES-2 15.000	907004	92.0079	1	Hydro
T-ABA2-2 10.500	907005	8.8665	1	Hydro
BELES-3 15.000	907007	92.0079	1	Hydro
BELES-4 15.000	907009	92.0079	1	Hydro
GRANRENAIS-113.800	907011	250	1	Hydro
GRANRENAIS-213.800	907013	250	1	Hydro
FINCHA1 13.800	908001	27.9182	1.01	Hydro
NESHE-1 13.800	908002	19.8104	1	Hydro
FINCHA2 13.800	908003	27.9182	1.01	Hydro
NESHE-2 13.800	908004	19.8104	1	Hydro
FINCHA3 13.800	908005	2.4019	1.01	Hydro
FINCHA4 13.800	908006	2.7728	1.01	Hydro
TEKEZE1 13.800	909001	47.9167	1.02	Hydro
TEKEZE2 13.800	909004	47.5449	1.02	Hydro
TEKEZE3 13.800	909005	47.9167	1.02	Hydro
ALT-LANG-1 11.000	911001	4.3658	1	Thermal
ALT-LANG-II 11.000	911002	4.3658	1.03	Thermal

AWASH2-1	10.500	911003	3.0901	1.03	Hydro
AWASH3-1	10.500	911004	3.0901	1.03	Hydro
KOKA1	10.500	911005	8.6499	1.03	Hydro
KOKA3	10.500	911006	0	1.03	Hydro
M-WAKNA1	13.800	911007	20.9827	1	Hydro
AWASH2-2	10.500	911008	3.5466	1.03	Hydro
AWASH3-2	10.500	911009	3.0901	1.03	Hydro
KOKA2	10.500	911010	8.6499	1.03	Hydro
M-WAKNA2	13.800	911011	0	1	Hydro
M-WAKNA3	13.800	911012	27.3619	1	Hydro
M-WAKNA4	13.800	911013	27.3619	1	Hydro
TULU MOYE-1	13.800	911019	49.5259	1	Thermal
OMA-KURAZF1	33.000	913001	28	1	Thermal
OMA-KURAZ2	33.000	913002	36	1	Thermal
OMA-KURAZ3	33.000	913003	36	1	Thermal
GENALE-III	13.800	913004	150	1.03	Hydro
ADDIS-EFW	15.000	914001	21.4567	1	Thermal
G-GIB2-1	15.000	915002	78.4882	1	Hydro
G-GIBE1-1	13.800	915003	56.5781	1.02	Hydro
G-GIB2-2	15.000	915004	78.4882	1	Hydro
G-GIBE1-2	13.800	915005	47.1487	1.02	Hydro
G-GIB2-3	15.000	915006	78.4882	1	Hydro
G-GIBE1-3	13.800	915007	47.1487	1.02	Hydro
G-GIB2-4	15.000	915008	78.4882	1	Hydro
G-GIB3 1	13.800	915009	800	1	Hydro
G-GIB3 2	13.800	915010	640	1	Hydro

Table A.14 Base load data of the existing aggregated wind power generators for the stable case

WPP ID	Bus ID	S_r in MVA	Active Power in MW	Model WTG Type	Number of WT	
AYISHA-WIND	33.000	803026	120	106.7779	DFIG-based WT	48
ASHEGODA-WF	33.000	909006	120	41.6017	DFIG-based WT	90
ADAMA WF-II	33.000	911015	153	34.6681	DFIG-based WT	102
ADAMA WF-I	33.000	911016	51	11.8862	DFIG-based WT	34
ASSELA WIND	33.000	911018	100	34.6681	DFIG-based WT	67

E Microgrid test network data

The microgrid in Figure 7.5, which have been used for implementing the frequency control strategy, has three main components the wind power plant, the thermal power plant and the microgrid system. The wind turbine generators with detailed data in Table A.3 and converter control parameters in Table A.4 have been applied for the microgrid simulation. The simulation inputs for the microgrid and the thermal power plant parameters are given below.

Table A.15 Base load data for the microgrid system

Parameter	Value	Unit	Description
Base power S_{base}	100	MVA	-
Base voltage at low-voltage bus-bar (B1)	575	Volts	-
Base voltage at high-voltage bus-bar (B2)	230	kV	-
Initial load power	315	MW	
System inertia constant H_{sys}	8.5658	Sec	$H_{sys} = (H_w P_{w,nom}/S_{base}) + (H_{th} P_{th}/S_{base})$
System damping constant D_{sys}	1.0425	-	$D_{sys} = (D_w P_{w,nom}/S_{base}) + (D_{th} P_{th}/S_{base})$

Table A.16 Synchronous generator parameters of the thermal power plant in the microgrid

Parameter	Value	Unit
Nominal power	85	MVA
Coupling transformer rated voltage	230	kV
Coupling transformer reactance	0.052	pu
Stator resistance R_s	0.0036	pu
d-axis steady-state reactance X_d	1.56	pu
q-axis steady-state reactance X_q	1.06	pu
d-axis transient reactance X'_d	0.296	pu
d-axis stator transient reactance X'_q	0.296	pu
Inertia constant H_{th}	5.0	Sec
Damping constant D_{th}	0.2	-

Curriculum Vitae

Tahaguas A. Woldu

Married, 2 children

Universitätsplatz. 2,

39106 Magdeburg



Work Experience

- Since 07/2019 **Scientific staff, Otto von Guericke University, Magdeburg**
Chair of electrical power network and renewable energy sources (LENA)
- Modelling and simulation of power system dynamics for projects in the chair
 - Development of wind turbine generator model in MATLAB/Simulink
- 02/2016 – 04/2017 **Associate Dean for Academic Affairs, Adama Science and Technology University, Ethiopia**
School of Electrical Engineering and Computing
- 12/2011 – 04/2017 **Lecturer, Adama Science and Technology University, Ethiopia**
School of Electrical Engineering and Computing
- Delivering courses on Renewable Energy Technologies, power system planning and operation; power system protection and control.
- 01/2013 – 02/2016 **Resident Engineer, Adama-II Wind Power Project (153 MW), Ethiopia**
ASTU-MU JV consultant for Adama-II Wind Power Project
- Supervise and verify the installation, testing and commissioning of wind turbines and their grid integration compatibilities.
- 09/2009 – 12/2011 **Power System Planning Engineer, Ethiopian Electric Power**
Strategic and power System Planning Corporate Office
- Expansion planning for generation and transmission systems by preparing short- and long-term national master plans
 - Power system modelling and simulation for studying system security

Education background

- 05/2017-12/2022 **Otto von Guericke University, Magdeburg, Germany**
PhD in Electrical Engineering (Dr.-Ing.)
- Focus on power system dynamics and control systems related to grid integration of renewable energy sources.
 - Thesis title: “Modeling and Simulation of Power System Dynamics for Studying the Impacts of Increasing Wind Power in a Weak Grid System”
- 09/2007 – 09/2010 **Royal Institute of Technology (KTH), Stockholm, Sweden**
M.Sc. Renewable Energy Engineering
- Focus on renewable energy sources, power generation and energy management
 - Thesis title: “Long-term renewable energy developments in the Ethiopian power system”
- 09/2002 – 08/2007 **Addis Ababa University, Addis Ababa, Ethiopia**
B.Sc. Electrical Engineering
- Focus on electrical power and control systems
 - Final project: “Design of Ultra-wide band communication system”